Engineering Hierarchical DNA-based Synthetic Cells

Dissertation
zur Erlangung des Grades
„Doktor der Naturwissenschaften “
im Promotionsfach Chemie

am Fachbereich
Chemie, Pharmazie, Geographie und Geowissenschaften
der Johannes Gutenberg-Universität
in Mainz

Wei Liu

Mainz, May 2024

Engineering Hierarchical DNA-based Synthetic Cells

Dissertation

Wei Liu

Parts of this work have been published:

1. Mechanistic Insights into the Phase Separation Behavior and Pathway-Directed Information Exchange in all-DNA Droplets. *Angew. Chem. Int. Ed.* **61***,* e202208951 (2022).

2. Switchable Hydrophobic Pockets in DNA Protocells Enhance Chemical Conversion. *J. Am. Chem. Soc.* **145***,* 7090-7094 (2023)*.*

3. A Facile DNA Coacervate Platform for Engineering Wetting, Engulfment, Fusion and Transient Behavior. *Commun. Chem.* **7**, 100 (2024).

Erklärung

gemäß § 18 Abs. 6 und § 15 Abs. 8 der Ordnung für die Prüfung im lehramtsbezogenen Bachelorstudi-engang an der Johannes Gutenberg-Universität Mainz (POLBA, ggf. POLBA-Dijon), bzw. § 18 Abs. 5 und § 15 Abs. 10 der Ordnung für die Prüfung im Masterstudiengang für das Lehramt an Gymnasien (POLMA, ggf. POLMA Dijon, iPOLMA-Dijon).

Hiermit erkläre ich, Wei Liu ,
dass ich die vorliegende Arbeit selbstständig verfasst und keine anderen als die angegebenen Quellen oder Hilfsmittel (einschließlich elektronischer Medien und Online-Quellen) benutzt habe. Mir ist be-wusst, dass ein Täuschungsversuch oder ein Ordnungsverstoß vorliegt, wenn sich diese Erklärung als unwahr erweist. § 18 Absatz 3 und 4 der o. g. Ordnungen gilt in diesem Fall entsprechend.

Auszug aus § 18 o. g. Ordnungen: Versäumnis, Rücktritt, Täuschung, Ordnungsverstoß

(3) Versucht die Kandidatin oder der Kandidat das Ergebnis einer Prüfung durch Täuschung oder Benutzung nicht zugelassener Hilfsmittel zu beeinflussen, gilt die betreffende Prüfungsleistung als mit „nicht ausreichend“ (5,0) absolviert (…)

(4) Die Kandidatin oder der Kandidat kann innerhalb einer Frist von einem Monat verlangen, dass Entscheidun-gen nach Absatz 3 Satz 1 und 2 vom jeweils zuständigen Prüfungsausschuss überprüft werden. Belastende Ent-scheidungen sind der Kandidatin oder dem Kandidaten unverzüglich schriftlich mitzuteilen, zu begründen und mit einer Rechtsbehelfsbelehrung zu versehen. Der Kandidatin oder dem Kandidaten ist vor einer Entscheidung Gelegenheit zur Äußerung zu geben.

Abstract

Liquid-liquid phase separation (LLPS) is a fundamental phenomenon in living cells, which drives the organization of biomolecules into liquid condensates and plays critical roles in cellular dynamics and functions. This biological blueprint has inspired the development of synthetic compartments, including membranous structures, colloidosomes, and coacervates, which have emerged as promising models for studying cellular behaviors and investigating the origins of life. Protocells, which are simplified cell-like compartments with membranous structures, serve as pivotal models for exploring early cellular evolution. Additionally, biomolecular coacervates are also gaining attention for their relevance to membraneless organelles and their potential in various applications, such as drug delivery and synthetic biology. Due to the programmability and sequence-specificity, DNA emerges as an enticing component for fabricating these micro/nanostructures, offering valuable insights into the mechanisms of life. DNA-based synthetic cell models have been constructed to mimic cellular behaviors and functions attributed to DNA's high programmability and the simplicity of the fabrication process, thereby bridging the understanding gap between living and non-living matter. However, significant challenges remain in deciphering the specifics of ssDNA phase separation as an essential process in ssDNA-based synthetic cells, and in balancing the complexity and simplicity of these synthetic cells, highlighting an ongoing need for exploration in this interdisciplinary field.

Within the framework of this thesis, LLPS-driven DNA-based synthetic cell models have been introduced to study self-assembling processes and chemical reactions in a DNA-based crowded environment:

In the first part of the thesis, all-DNA droplets were formed by using metal ion-dependent phase separation of ssDNA. Two phase separation temperatures corresponding to the formation of primary nuclei and droplet growth were found. Two different cations were investigated (Ca^{2+} vs. Mg^{2+}), regarding their regulation of dynamics in phase separation. Ca^{2+} allows for irreversible, whereas Mg^{2+} leads to reversible phase separation. This new Ca^{2+}-specific kinetic trapping could be utilized for simple Ca^{2+}/all-DNA droplet formation, and also opened a new design space to trigger information exchange between coacervates and protocells stemming from

distinct ion-specific pathways. Specifically, a Ca^{2+}-derived polyadenine-rich droplet could merge its information content with a Mg^{2+}-derived core/shell DNA protocell formed by a polyadenine/polythymine mixture by proper salinity adjustment and using a secondary temperature ramp. This part introduces new kinetic traps of phase separating ssDNA that lead to new phenomena in cell-mimicking systems.

Based on the concept of Mg^{2+}-induced reversible phase separation of ssDNA, we introduced a crowded all-DNA protocell and embedded a temperature-switchable DNA-*b*-polymer block copolymer, in which the synthetic DNA-*b*-polymer copolymer can undergo phase segregation at elevated temperatures. We showed that phase segregation of the DNA-*b*-polymer copolymer occurred by spinodal/viscoelastic phase separation and led to the formation of artificial organelle structures that can reorient into larger phase-segregated domains depending on the viscoelastic properties of the protocell interior. Notably, this compartment formation was reversible upon temperature adjustment. Enhanced solubilization of hydrophobic molecules confirmed the formation of hydrophobic compartments, in which we elucidated the enhanced reactivity of a self-reporting bimolecular reaction. This study demonstrated how to harness the individual strength of biological and synthetic polymers to construct advanced biohybrid artificial cells that offer insights into phase segregation under macromolecularly crowded conditions and the formation of synthetic organelles and microreactors in response to environmental changes.

The third part demonstrates a simple approach for the formation of dynamic, multivalency-driven coacervates using long ssDNA homopolymer in combination with a series of palindromic binders. We reveal details on how the length and sequence of the multivalent, self-complimentary binders influence coacervate formation, how to introduce switching and autonomous behavior in reaction circuits, as well as how to engineer wetting, engulfment, and fusion in multi-coacervate system. Our simple-to-use model DNA coacervates fundamentally enhance the understanding of coacervate dynamics, fusion, phase transition mechanisms, and wetting behavior between coacervates, forming a solid foundation for the development of innovative synthetic coacervates with programmable properties for fundamental studies and applications.

From a future perspective, understanding the formation mechanisms and the flexible design space for engineering different dynamic behaviors of DNA compartments will pave the way for the engineering of functional DNA-based cell-mimicking systems.

The ability to control compartment morphologies offers new strategies for developing tunable compartments for biological functions in catalytic reactions, information transfer, and partitioned storage.

Zusammenfassung

Die Flüssig-flüssig-Phasentrennung (LLPS) ist ein zentrales Phänomen in lebenden Zellen, das entscheidend für die Organisation von Biomolekülen in flüssigen Kondensaten ist und eine wesentliche Rolle in der zellulären Dynamik und Funktion spielt. Dieses biologische Prinzip hat die Entwicklung von synthetischen Kompartimenten inspiriert, darunter membrane-basierte Strukturen, Kolloidosome und membrane-freie Coacervate. Diese Strukturen haben sich als vielversprechende Modelle zur Untersuchung zellulärer Verhaltensweisen und zur Erforschung des Ursprungs des Lebens erwiesen. Protozellen, die als vereinfachte, zellähnliche Kompartimente mit membranösen Strukturen fungieren, sind zentrale Modelle zur Untersuchung der frühen zellulären Evolution. Zudem rücken biomolekulare Coacervate aufgrund ihrer Bedeutung für membranlose Organellen und ihre vielfältigen Anwendungsmöglichkeiten in Bereichen wie der Arzneimittelabgabe und der synthetischen Biologie in den Fokus der Forschung. Die Programmierbarkeit und Sequenzspezifität der DNA machen DNA zu einer attraktiven Komponente für die Herstellung dieser Mikro-/Nanostrukturen und bieten tiefe Einblicke in die Lebensmechanismen. Aus diesem Grund wurden auf Einzelstrang-DNA (ssDNA) basierende synthetische Zellmodelle entwickelt, die zelluläre Verhaltensweisen und Funktionen nachahmen, welche auf hoher Programmierbarkeit und der Einfachheit des Herstellungsprozesses beruhen. Diese Modelle dienen dazu, die Kluft im Verständnis zwischen lebender und nicht-lebender Materie zu überbrücken. Dennoch bestehen weiterhin erhebliche Herausforderungen bei der Entschlüsselung der Details der ssDNA-Phasentrennung und bei der Ausbalancierung zwischen Komplexität und Simplizität dieser synthetischen Zellen, was die Notwendigkeit fortgesetzter Forschung in diesem interdisziplinären Feld unterstreicht.

In dieser Arbeit wurden zwei Ansätze zur Untersuchung von LLPS-gesteuerten DNA-basierten synthetischen Zellmodellen vorgestellt, die darauf abzielen, Selbstorganisationsprozesse und chemische Reaktionen innerhalb einer DNA-reichen molekular gecrowdeden Umgebung zu erforschen:

Im ersten Teil dieser Arbeit wurden DNA-Tröpfchen durch die metallionenabhängige Phasentrennung von ssDNA erzeugt. Es wurden zwei spezifische Phasentrennungstemperaturen identifiziert, die jeweils der Bildung von Primärkernen

und dem Wachstum von Tröpfchen zugeordnet werden können. Dabei wurden die Effekte von zwei unterschiedlichen Kationen (Ca^{2+} und Mg^{2+}) auf die Dynamik der Phasentrennung untersucht. Während Ca^{2+} eine irreversible Phasentrennung bewirkt, führt Mg^{2+} zu einer reversiblen Trennung. Diese neu entdeckte Ca^{2+}-spezifische kinetische Falle ermöglicht nicht nur die einfache Bildung von Ca^{2+}/All-DNA-Tröpfchen, sondern eröffnet auch innovative Möglichkeiten für den Informationsaustausch zwischen Coacervaten und Protocellen, die auf unterschiedlichen ionenspezifischen Mechanismen basieren. Insbesondere kann ein Ca^{2+}-abgeleitetes PolyA-reiches Tröpfchen, das in einer Mg^{2+}-Umgebung instabil wäre, seinen Informationsgehalt mit einem Mg^{2+}-abgeleiteten Kern/Schale DNA-Protocell, das aus polyA/polyT besteht und ebenfalls nicht in einer Ca^{2+}-Umgebung entstehen würde, durch angemessene Salinitätsanpassung und die Anwendung einer sekundären Temperaturrampe verschmelzen. Dieser Abschnitt führt neue kinetische Fallen bei der Phasentrennung von ssDNA ein, die zu innovativen Phänomenen in zellnachahmenden Systemen führen.

Basierend auf dem Konzept der durch Mg^{2+} induzierten reversiblen Phasentrennung von ssDNA, entwickelten wir eineDNA-Protozelle und integrierten ein temperaturschaltbares DNA-*b*-Polymer Block-Copolymer. Dieses synthetische Copolymer kann bei erhöhten Temperaturen eine Phasensegregation durchführen. Unsere Ergebnisse zeigen, dass die Phasensegregation des DNA-*b*-Polymer-Copolymers mittels einer spinodal/viskoelastisch Phasentrennung stattfindet und zur Bildung von künstlichen Organellstrukturen führt. Diese Strukturen können sich, abhängig von den viskoelastischen Eigenschaften des Protozellinneren, in größere phasensegregierte Domänen umorientieren. Diese Kompartimentbildung ist reversibel. Fluoreszenzsensoren bestätigen die Bildung hydrophober Kompartimente, und wir konnten eine gesteigerte Reaktivität einer bimolekularen Reaktion innerhalb dieser Kompartimente nachweisen. Die Studie verdeutlicht, wie die spezifischen Eigenschaften biologischer und synthetischer Polymere genutzt werden können, um fortschrittliche biohybride künstliche Zellen zu konstruieren. Diese bieten tiefgreifende Einblicke in die Phasensegregation unter makromolekular gecrowdeden Bedingungen sowie in die Bildung von synthetischen Organellen und Mikroreaktoren als Reaktion auf Umweltveränderungen.

Im dritten Teil dieser Arbeit wird ein einfacher Ansatz zur Bildung dynamischer, multivalenzgetriebener Coacervate vorgestellt. Es wurde ein langes ssDNA-Homopolymer in Kombination mit einer Serie palindromischer Binder genutzt. Wir geben Einblicke, wie die Länge und Sequenz dieser multivalenten, selbstkomplementären Binder die Coacervatbildung beeinflussen. Weiterhin erörtern wir Methoden, um schaltbares und autonomes Verhalten in Reaktionskreisen zu implementieren, sowie Techniken zur Gestaltung von Benetzungsprozessen, Engulfment und Fusion in einem Multi-Coacervat-System. Unsere benutzerfreundlichen Modell-DNA-Coacervate tragen wesentlich zum besseren Verständnis der Coacervatdynamik, der Fusion, der Phasenübergangsmechanismen und des Benetzungsverhaltens zwischen Coacervaten bei. Sie bilden eine robuste Grundlage für die Entwicklung innovativer synthetischer Coacervate mit programmierbaren Eigenschaften, die sowohl für grundlegende Studien als auch für praktische Anwendungen von Bedeutung sind.

Aus zukünftiger Perspektive wird das Verständnis des Bildungsmechanismus und das flexible Design verschiedener dynamischer Verhaltensweisen von DNA-Kompartimenten den Weg für die Entwicklung funktionaler, DNA-basierter, zellnachahmender Systeme ebnen. Die Fähigkeit, die Morphologie dieser Kompartimente gezielt zu steuern, eröffnet neue strategische Möglichkeiten zur Entwicklung anpassbarer Kompartimente. Diese können speziell für biologische Funktionen in katalytischen Reaktionen, Informationsübertragung und abgeteilter Speicherung konzipiert werden, was ihre Anwendungsbreite in der Biotechnologie und verwandten Feldern deutlich erweitert.

Contents

Abbreviations

LLPS	Liquid-liquid phase separation
ssDNA	Single-stranded DNA
DOTAP	N-[1(2,3-dioleoyloxy)propyl]-N,N,N-trimethylammonium chloride
PCR	Polymerase chain reaction
6HB	Six-helix-bundle
PTA	Photothermal agent
HRP	Horseradish peroxidase
FeM	Fe-rich montmorillonite
NIPAAm	N-isopropyl acrylamide
ALP	Alkaline phosphatase
MLOs	Membraneless organelles
ATP	Adenosine triphosphate
FRAP	Fluorescence recovery after photobleaching
nt	Nucleotide
A	Adenine
T	Thymine
G	Guanine
C	Cytosine
dsDNA	Double-stranded DNA
dNTPs	Deoxynucleotide triphosphates
TdT	Terminal deoxynucleotidyl transferase
3'-OH	3'-Hydroxy terminus
RCA	Rolling circle amplification
SEs	Sticky ends

RCM	Ring-closing metathesis
ArMs	Artificial metalloenzymes
Sav	Streptavidin
Biot-Ru	Biotinylated olefin metathesis catalyst
ATPS	Aqueous two-phase systems
PEG	poly(ethylene glycol)
NaCl	Sodium chloride
Tris-HCl	Tris(hydroxymethyl)-aminomethane hydrochloride
EDTA	Ethylenediaminetetraacetic acid disodium salt dihydrate
nb	Nucleobases
RT	Room temperature
LCST	Lower critical solution temperature
CLSM	Confocal laser scanning microscopy
DLS	Dynamic light scattering
RCA	Rolling circle amplification
AGE	Agarose gel electrophoresis
T_1	Primary nucleation temperature
T_2	Growth temperature
FRAP	Fluorescence recovery after photobleaching
TCA	Trichloroacetic acid
ETT Activator	5-(Ethylthio)-1H-tetrazole
$CaAc_2$	Calcium acetate
$MgCl_2$	Magnesium chloride
Na_2HP_4	Sodium phosphate dibasic
KH_2PO_4	Potassium phosphate monobasic
KCl	Potassium Chloride

DMAP	4-dimethylaminopyridine
mTEGA	Triethylene glycol methyl ether acrylate
eDEGA	Diethylene ethyl ether acrylate
Me_6TREN	Tris[2-(dimethylamino)ethyl]amine
PCs	Protocells
i*-*b*-pEGA	ssDNA-*b*-Polyethylene glycol acrylate
BCP	Block copolymer
Cu-LRP	Cu-controlled living radical polymerization
T_{cp}	Cloud point temperature
Rhd	Rhodamine
GPC	Gel permeation chromatography
T_m	Melting temperature

1 Introduction

1.1 Synthetic Cell Model

Cell biology has evolved from its traditional focus on cell structure and function to encompass a wide range of applications, from medicine to environmental science, including advances in drug delivery, cell engineering, and biotechnology.[1] This expansion is partly due to the challenges presented by the complexity of biological cells, such as loss of activity or cell death when studied outside their natural environment. As a result, there is a growing interest in creating simplified models in the molecular life sciences. One innovative approach is the development of bottom-up synthetic cells. These are constructed from non-living materials that mimic specific properties and functions of biological cells. These synthetic systems are built using a variety of components, including synthetic materials, biomimetic nanostructures, or elements derived from different organisms.[2] When designing synthetic cells, scientists focus on three fundamental properties: the ability to replicate information-carrying molecules, having selectively permeable membranes, and the capability to undergo metabolic processes.[3, 4] Research in this area has led to the categorization of synthetic cells into three main types: membranous structures (which include liposomes, fatty acid vesicles, and polymersomes), colloidosomes, and membraneless coacervates (Figure 1.1).[2] Each of these groups represents different strategies and materials used to mimic the essential functions of natural cells.

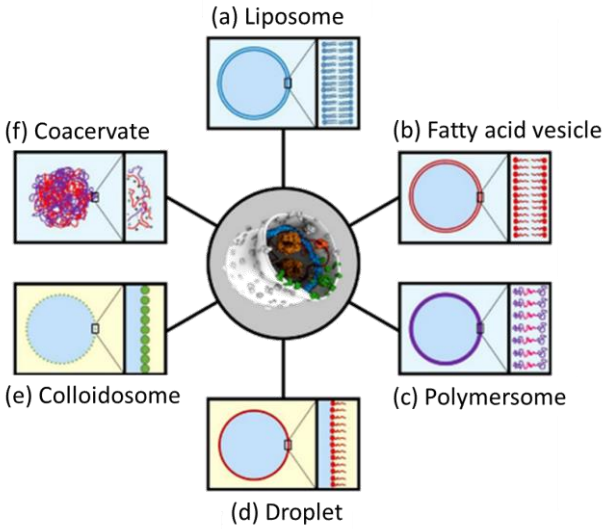

Figure 1.1. Synthetic cells with different structures. The magnified view on the right side of each panel illustrates the molecular structure of the boundary of each synthetic cell models. Graphics adapted with permission from Ref. *(2)*.

1.1.1 Membranous Structures

Synthetic cell membranes, typically in the form of spherical vesicles, are defined by bilayer membranes that emerge from the spontaneous self-assembly of amphiphilic molecules. These vesicles, synthesized in vitro within aqueous dispersions, comprise an aqueous interior encapsulated by one or several thin layers of amphiphilic molecules. In the structure of a vesicle membrane, the hydrophilic parts of the amphiphiles interface with the surrounding aqueous medium, whereas the hydrophobic parts congregate to form the inner of each layer, thus creating a stable bilayer configuration. Phospholipids, which are conventional amphiphilic molecules, consist of a hydrophilic phosphate head and two hydrophobic carbon tails. They are a primary component of the cell membrane, playing crucial structural and metabolic roles in living cells. The amphipathic nature of phospholipids drives their self-assembly into two-layer structures, known as lipid bilayers, with the phosphate heads facing outward and the carbon tails inward. This arrangement forms water-filled spherical vesicles, commonly referred to as liposomes, making them a popular choice for the construction of synthetic cells due to their cellular membrane, easy preparation, and high biocompatibility.[5, 6] Liposomes are generally impermeable to ions but can allow the permeation of small neutral molecules. Various methods, such as thin-film hydration,[7, 8] solvent injections,[9] electroformation,[10] and microfluidics,[11, 12] facilitate the creation of liposomes in sizes ranging from tens of nanometers to several micrometers.[13] The structural and physicochemical characteristics of liposomes, including size, stability, and surface charge, can be fine-tuned by incorporating materials like cholesterol and N-[1(2,3-dioleoyloxy)propyl]-N,N,N-trimethylammonium chloride (DOTAP).[14, 15] Additionally, adjusting solution parameters like ionic strength, pH, and temperature can further optimize these properties.[16]

Cell division is a crucial process for the growth, repair, and reproduction of living cells. Studying the mechanical division of liposomes contributes to our understanding of the growth-division cycle of biological cells and aids in exploring the origins of life. Deshpande *et al.* introduced an octanol-assisted liposome on a chip using a microfluidic splitter technique (Figure 1.2a).[17] This method achieved rapid, protein-free division of monodisperse liposomes that possess excess surface area and are of a specific size (ca. 6 μm in diameter) for the stretching at the splitter. Furthermore, research showed that biomolecular processes, such as polymerase chain reaction

(PCR), RNA polymer synthesis, and protein production, can be carried out inside liposomes. This is possible by encapsulating enzymes and other relevant constituents, thereby making liposomes ideal models for synthetic cells in mimicking cell metabolism.[18-21] Investigations into the morphological and functional aspects of liposome-based complexes, formed by integrating nucleic acids or proteins with liposomes (Figure 1.2b), have extended the application of liposomes, including mimicking organelle configuration and dynamics, as well as vesicle transport and communication.[22, 23] However, liposomes also have limitations in terms of chemical functionality and stability, including susceptibility to chemical degradation through lipid oxidation and hydrolysis.[24]

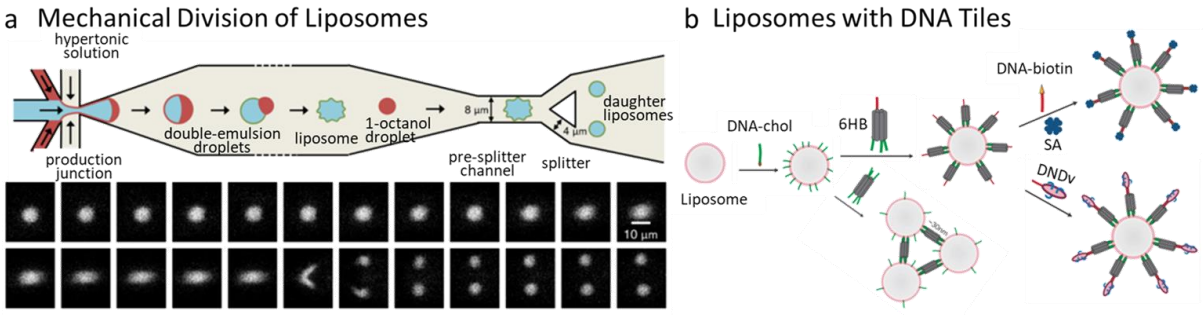

Figure 1.2. Formation and function of Liposome based on different strategies. (a) Liposome division using microfluidic method. Top panel: schematic of the mechanical division of liposomes. Double-emulsion droplets were formed at the production junction, then spontaneously separated into liposomes and octanol droplets. In a hypertonic environment, the liposomes could undergo a volume reduction, thereby establishing a high surface area-to-volume ratio. These "flexible" liposomes then passed through a narrow presplitter channel at high speed, after which they encountered the Y-shaped splitter, leading to their division into two daughter liposomes. Bottom panel: A moving-frame region-of-interest depicting the full division process. The interval between successive frames was 2 ms. Graphics adapted with permission from Ref. *(17)*. **(b)** DNA-mediated liposome coating was used for protein display and distance-controlled cluster formation by employing various DNA tiles. Liposomes coated with six-helix-bundle (6HB) DNA tiles with a single handle were further functionalized for protein display. Liposomes with 6HB DNA tiles with handles at both ends were utilized to create distance-defined liposome clusters. Graphics adapted with permission from Ref. *(22)*.

Fatty acids, another important type of amphiphilic molecules, consist of a single-chain structure with a hydrophilic carboxylic acid head and a hydrophobic aliphatic tail. While they share similarities with phospholipids in their ability to self-assemble into vesicles, fatty acids form vesicles with simpler structures and possess unique properties distinct from conventional phospholipid vesicles (liposomes).[25] A notable difference is their increased permeability to small cations, setting them apart from liposomes in terms of membrane dynamics and interaction with their environment. Unlike double-chained phospholipids, whose synthesis from various compounds under prebiotic conditions remains highly debatable,[26] the simpler structure of fatty acids suggests a greater likelihood of their production from CO and H_2 in conditions that simulate the primitive

Earth.[27, 28] Therefore, fatty acid vesicles serve as compelling membrane models for investigating primordial cells on early Earth.

Fatty acid vesicles typically form within a specific pH range, between 7 and 9, where half of the carboxyl groups become charged.[29] Gebicki and Hicks first reported the formation of fatty acid vesicles from oleic acid under slightly alkaline conditions.[30] Hargreaves and Deamer *et al.* further outlined the minimum physicochemical requirements necessary for fatty acid vesicle formation.[31] They demonstrated that for vesicle formation, the hydrocarbon chain length should be longer than eight carbons, and the temperature should be above the fatty acid's phase transition temperature. However, the high concentrations of Mg^{2+} (50 to 200 mM) needed for RNA copying reactions could cause fatty acid precipitation. Adamala *et al.* demonstrated that citrate-chelated Mg^{2+} could protect fatty acid vesicles from disruption and increased the permeability of small polar molecules, thereby ensuring efficient template-directed RNA synthesis inside vesicles.[32] These findings highlight the potential of fatty acid vesicles in synthetic biology, particularly in the creation of cell-like structures capable of complex biochemical processes.

The pursuit of enhanced robustness in vesicle formation has led to significant interest in synthetic amphiphilic polymers, especially following the limitations observed in phospholipid and fatty acid-based vesicles due to their thin bilayers and low mechanical stability. Drawing inspiration from naturally occurring amphiphiles, researchers have explored the potential of synthetic variants, leading to the pioneering work of the Eisenberg group in 1995.[33] They utilized polystyrene-*b*-poly(acrylic acid) block copolymers to investigate the influence of molecular mass on morphologies. This exploration was further advanced in 1999 by the Discher group, who introduced the concept of "polymersomes" or polymer vesicles, using poly(ethylene oxide)-*b*-polybutadiene block copolymers and drawing an analogy to liposomes.[34] The formation of polymersomes typically employs a variety of copolymers, including diblock, triblock, multiblock, star, grafted, and hyperbranched types (Figure 1.3a).[35, 36] Key factors influencing their formation include molecular weight, the weight fraction of the hydrophilic block, and the interaction strength between the hydrophobic fraction and water. By fine-tuning these parameters, the stability, mechanical properties, and permeability of the polymersomes can be optimized.[37] For instance, a semi-permeable polymersome using a diblock copolymer consisting of styrene and 3-(isocyano-l-

alanyl-amino-ethyl)-thiophene has shown potential in encapsulating enzymes and allowing the substrate to diffuse through the membrane.[38]

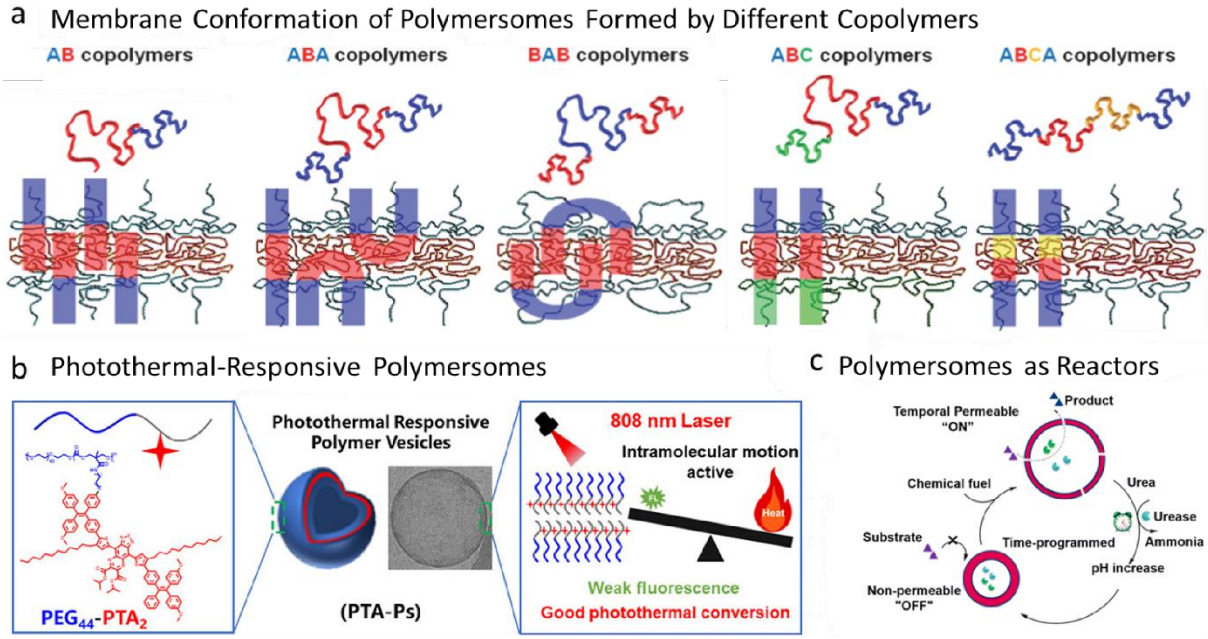

Figure 1.3. Formation and functions of polymersomes. (a) Membrane conformation of polymersomes formed from different copolymers. Hydrophilic segments are colored in blue and green, while hydrophobic blocks are represented in red and yellow. Graphics adapted with permission from Ref. *(35)*. **(b)** Preparation and properties of photothermal-responsive polymersomes. The photothermal moiety PTA was introduced into an amphiphilic block copolymer PEG_{44}-PTA_2, leading to the formation of polymersomes that exhibit good photothermal conversion and weak fluorescence. Graphics adapted with permission from Ref. *(42)*. **(c)** pH-sensitive polymersomes were used as self-adaptive nanoreactors, which could be achieved by incorporating horseradish peroxidase (HRP) and urease into the polymersomes. Upon exposure to a chemical fuel (an acidic urea solution), these polymersomes could undergo temporary swelling and increased permeability, coupling with a decrease in pH, activating the "ON" state of HRP enzymatic catalysis. As the fuel (urea) was consumed, an increase in pH, owing to the ammonia produced, resulted in the shrinking of polymersomes, thus transitioning to a catalytic "OFF" state. Graphics adapted with permission from Ref. *(45)*.

Moreover, targeting specific cells could be achieved through modifications with proteins or sugars,[39, 40] while incorporating stimuli-responsive units enabled polymersomes to react to environmental changes, such as pH, light, heat, oxidation, and reduction.[41] An innovative development in this field was the introduction of a photothermal-responsive polymersome by Luo *et al.*, employing a poly(ethylene glycol)-*b*-poly(trimethylene carbonate) block copolymer with a photothermal agent (PTA) (Figure 1.3b).[42] This design allows the temperature of the polymersome solution to increase rapidly under near-infrared laser irradiation, demonstrating its potential for photothermal therapy in anticancer treatments. Owing to their enhanced chemical properties and biocompatible, polymersomes are suitable for versatile applications in synthetic vesicle research, such as drug delivery, nanoreactors, nanocarriers, and artificial cells. The encapsulation of catalytic species like enzymes within

polymersomes opens opportunities for nanoreactor applications.[43, 44] Che *et al.* presented self-adaptive nanoreactors by encapsulating pH-responsive polymersomes with enzymes such as horseradish peroxidase (HRP) and urease, and incorporating acidic urea fuel (Figure 1.3c).[45]

As previously mentioned, liposomes, composed of natural components like phospholipids, have been studied as artificial cells since the 1970s.[46] Despite their limited chemical functionality and stability, they laid the groundwork for subsequent advancements. In the 1990s, polymersomes based on synthetic block copolymers emerged, offering improved surface functionality and toughness, but they lacked the biomimetic resemblance to cells.[34] To address these limitations and combine the advantageous properties of both liposomes (such as competitive biocompatibility and permeability) and polymersomes (such as tunable physical properties), hybrid vesicles comprised of both amphiphilic lipids and copolymers have attracted particular interest among researchers over the past two decades.[47] These hybrid vesicles are anticipated to provide tunable properties and enhanced functionalization control. Khan *et al.* reported that the properties of hybrid vesicles could be adjusted by varying the copolymer composition and the lipid-to-polymer ratio.[48]

1.1.2 Colloidosomes

The development of artificial cells using organic materials like lipids and/or polymers has made significant progress, but these materials often show limitations in terms of controlled permeability and mechanical strength, which are crucial for some applications, such as biosensors, enzyme reactors, and drug delivery systems. To overcome these challenges, researchers have developed inorganic colloidosomes. Colloidosomes are predominantly synthesized through the self-assembly of colloidal materials at the interface of two immiscible phases, such as water and oil.[49] The structure of these colloidosomes is characterized by interstices between assembled colloidal materials, such as silica nanoparticles, Au-Ag nanorods, iron nanoparticles, and clay. These colloidal materials are either inherently amphiphilic or chemically modified to become so, and then chemically crosslinked to create stable colloidosomes. The interstices between the particles resulted in the formation of pores on membrane surfaces, contributing to the selective permeability of the colloidosomes. The Pickering emulsion method, in particular, offers a versatile and gentle approach

to creating colloidosomes, making it a favored technique in applications involving temperature-sensitive biomolecules, including proteins and nucleic acids (Figure 1.4).[50]

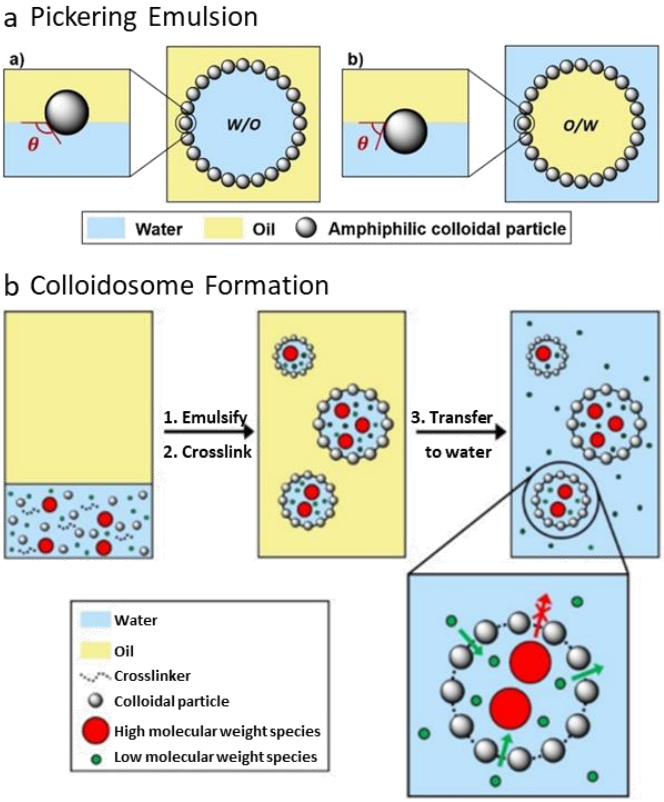

Figure 1.4. Colloidosome formation by Pickering emulsion technique. (a) Pickering emulsions are formed by the adsorption of amphiphilic colloidal particles at the surface between two immiscible liquids. When particles are more hydrophobic, they tend to have a high contact angle (θ > 90°), resulting in the formation of water-in-oil (w/o) emulsions. Conversely, when particles are more hydrophilic, oil-in-water (o/w) emulsions are typically formed. **(b)** Pickering emulsions are further processed through chemical crosslinking to form colloidosomes. These colloidosomes have a semipermeable membrane characterized by molecular weight cut-off properties. High molecular weight molecules (red) are retained inside the colloidosomes, while low molecular weight molecules (green) can freely diffuse in and out of the colloidosome membrane. Graphics adapted with permission from Ref. *(50)*.

The permeability of colloidosomes can be engineered through the modification of sensitive polymers to the particles that form their membrane. Li *et al.* produced nanoparticle-stabilized colloidosomes (Pickering emulsions) with pH-responsive permeability by covalently grafting a pH-responsive copolymer onto the silica-based membrane.[51] These colloidosomes could facilitate controlled enzymatic dephosphorylation reactions at various pH levels. Furthermore, researchers reported a protocelluar signaling process by transferring H_2O_2 generated within silica colloidosomes to Fe-rich montmorillonite (FeM) clay colloidosomes (Figure 1.5a–c).[52] This transfer led to the polymerization of N-isopropyl acrylamide (NIPAAm) to the

PNIPAAm polymer shell on the membrane. The PNIPAAm shell could then assist in regulating enzyme catalysis within FeM-clay colloidosomes. Additionally, they demonstrated that colloidosomes could undergo spontaneous growth and division by adjusting the balance between internal pressure and membrane rigidity (Figure 1.5d,e).[53]

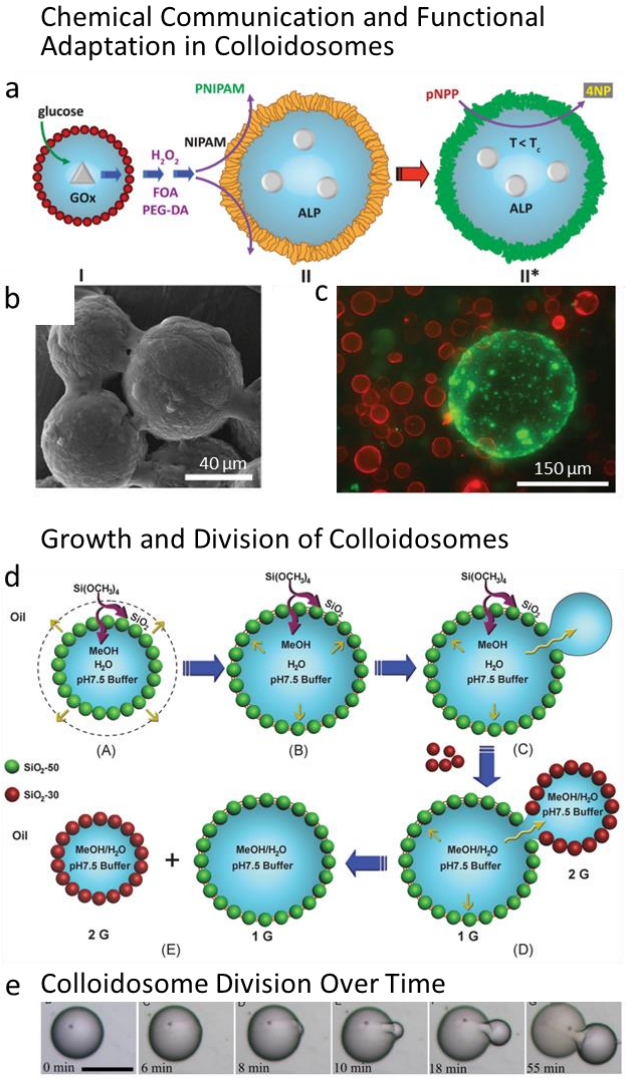

Figure 1.5. Functions of colloidosomes. (a-c) Chemical communication and functional adaption in colloidosomes. **(a)** Adding glucose to silica colloidosomes (I, red shell) that contain glucose oxidase, generated a H_2O_2 signal, which diffused to larger FeM-clay colloidosomes (II, orange shell), containing alkaline phosphatase (ALP). The H_2O_2 signal triggered colloidosomes to catalytically polymerize NIPAAm, forming a green fluorescent PNIPAAm shell on their membranes (II*, green shell). Following this signal-induced polymerization, a gating mechanism was activated within colloidosome II*, which regulated the dephosphorylation of pNPP to 4NP. **(b)** SEM image of FeM-clay colloidosomes with PNIPAAm polymer coating. **(c)** Fluorescence microscopy image of Rhodamine B-labelled silica colloidosomes (red) and the emergence of PNIPAAm/FeM-clay colloidosomes (green). Graphics adapted with permission from Ref. *(52)*. (d-e) Growth and division of silica colloidosomes by expanding their internal volume until reaching a critical volume, at which they split into two separate colloidosomes. **(d)** The scheme of the growth and division in colloidosomes involves a process where first-generation colloidosomes, composed of silanol and dimethylsilane groups, grow in size. This growth was enhanced by methanol, a hydrophilic molecule generated by the crosslinker tetramethoxysilane on the colloidosomes. As methanol accumulates, it caused the colloidosomes to expand until they reach a critical volume, at which the colloidosomes ruptured and subsequently divided into two separate entities. **(e)** Time-dependent optical microscopy images of the colloidosome division. Graphics adapted with permission from Ref. *(53)*.

1.1.3 Membraneless Coacervates

Spatiotemporal compartmentalization through liquid-liquid phase separation (LLPS) in living cells plays a crucial role in biological reactions and cellular functionalities. A particular class of dynamic compartments in cells called membraneless organelles (MLOs) has been found. Unlike traditional membrane-bound organelles, MLOs function in the absence of a surrounding lipid bilayer, which usually consist of various proteins and nucleic acids. Coacervation refers to the condensation of biomacromolecules to self-assemble into a liquid state (Figure 1.6).[54] This process is typically driven by weak interactions, such as electrostatic interactions, hydrophobic interactions, and π-stacking among proteins, nucleic acids, peptides, and synthetic biomolecules. To understand the properties, behaviors, and functions of MLOs in cells, membraneless coacervates formed through LLPS have shown great potential as model systems. Koga *et al.* reported that spontaneous phase separation of mononucleotides and cationic peptides into microscale coacervates with tunable stability at varied temperatures and salt concentrations.[55] The incorporation of nanoparticles and adenosine triphosphate (ATP) within these coacervates enables them to serve as reservoirs for nanoparticle-mediated oxidase reaction, as well as for glucose phosphorylation and dehydrogenation. Moreover, Donau *et al.* demonstrated the transient formation of RNA-based coacervates by introducing a fuel-driven reaction cycle into a mixture of polymeric RNA and a peptide.[56]

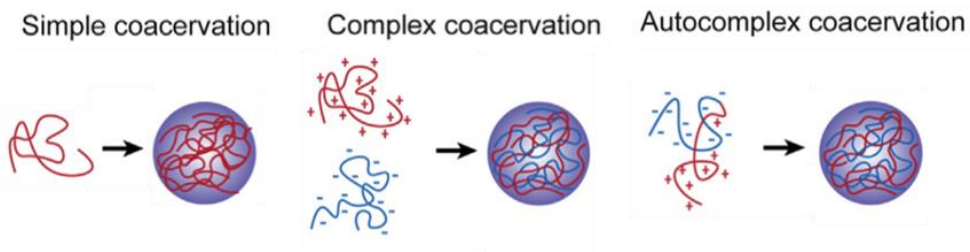

Figure 1.6. Coacervate structures comprise various macromolecules. Simple coacervation involves phase separation by one type of molecule, exemplified by cooling agarose in water. Complex coacervation results from interactions between oppositely charged molecules, as seen between nucleotides and peptides. Autocomplex coacervation occurs with self-organizing amphiphilic polymers, like the assembly of block copolymers in water. Graphics adapted with permission from Ref. *(54)*.

Coacervates and MLOs share striking similarities in their properties due to their identical formation concept of LLPS of macromolecules in dilute solution. Both behave like liquid droplets, with coacervates characterized as dense viscoelastic liquids whose viscosity can be modulated by factors such as chemical structure, length of the macromolecules, salt concentration, or temperature. Moreover, MLOs exhibit various

states, including liquid, gel and glass, showing dynamic behaviors like fusion, flow, dripping and wetting. Various methods, such as fluorescence recovery after photobleaching (FRAP), microrheology and fluorescence correlation spectroscopy, are employed to estimate the viscosity of MLOs.[57] MLOs can undergo complete or incomplete recovery after photobleaching, and their merging behavior varies — some fuse into a singular droplet, while others maintain an irregular shape after merging. Additionally, researchers suggest that MLOs display age-dependent dynamics, showcasing transitions from a liquid state to a gel or even a solid state.[58]

Developing multiphase coacervates by hierarchical organization to mimic the subcompartmentalization in MLOs has garnered significant attention. MLOs, including nucleolus, stress granules, and Cajal bodies, feature subcompartments organized hierarchically, ensuring efficient spatiotemporal functions within cells.[59] For instance, distinct subcompartments within the nucleolus are essential for ribosome biogenesis.[60] The formation of multiphase coacervates can be realized through the mixing of coacervates. Lu *et al.* demonstrated two possible scenarios in systems with mixtures of two coacervates: complete wetting resulting in a core/shell coacervate with one type inside the other, or a mixed coacervate; and partial wetting leading to a Janus-like structure with attached lenses.[61] The combination of coacervates with similar chemical characteristics resulted in a mixed coacervate, while those with varying chemical characteristics underwent phase separation into a multiphase coacervate. These wetting behaviors are closely related to the interfacial tensions and critical salt concentration. Coacervates with the highest interfacial tension, like the densest coacervates with the highest critical salt concentration, exhibiting greater hydrophobic properties or smaller coacervates, are more prone to engulfment.

1.2 DNA-based Synthetic Cells

The widespread utilization of DNA in constructing nano/micromaterials through a bottom-up approach is attributed to the programmability and selectivity of Watson-Crick base pairing, coupling with a decrease in the cost of gene synthesis. DNA nanotechnology represents the assembly of DNA strands into high-order structures, used as building blocks. Examples include DNA tiles and DNA origami, which can further assemble into complex and large-scale structures like DNA lattices, DNA

particles, and DNA nanotubes. These structures possess programmability, functionalization, and biocompatibility, making them highly applicable in biological fields, such as drug delivery, regulated adhesion, enzyme reaction, and communication.

The origins of life on Earth and the emergence of the first cells remain subjects that are not fully understood. Protocells, simplistic cell-like compartments, are widely recognized as models crucial for simulating the initial stages of cellular life.[62] The integration of protocells with the precise control and information storage capabilities inherent in DNA yields DNA-based synthetic cells. It offers unique insights into the potential roles of DNA during the early stages of life, providing a bridging of the understanding gap between living and non-living matter. Diverse categories of DNA-based synthetic cells exist, including DNA-encapsulated vesicles, DNA-hybrid coacervates, and all-DNA coacervate droplets, each distinguished by their unique structural and compositional attributes.

1.2.1 DNA Characteristics

(1) Watson-Crick base paring: J.D. Watson and F.H.C. Crick discovered the double-helical structure of DNA through the systematic arrangement of four nucleotide (nt) bases including adenine (A), thymine (T), guanine (G), and cytosine (C) (Figure 1.7a).[63] The systematic arrangement follows the principles of complementary base pairing: A binds to T via two hydrogen bonds, and G to C via three hydrogen bonds. This base pairing concept enables us to precisely design and predict the assembly of DNA sequences and the conformation of DNA structures.

(2) Toehold-mediated strand displacement: This strand displacement represents a mechanism for displacing a target strand from a double-stranded DNA (dsDNA) substrate complex by the introduction of a single-stranded DNA (ssDNA) invading strand (Figure 1.7b).[64, 65] The initiation of this displacement is enhanced by an overhang, also called “toehold”, which constitutes a short single-stranded segment in the dsDNA substrate complex. The attachment of the ssDNA invading strand to one of the substrates triggers a branch migration process, leading to the displacement of the targeted strand in the substrate complex. The rate of strand displacement can be tuned by adjusting the toehold binding strength, which is influenced by factors such as DNA length and GC content. The reaction rate constant without a toehold was determined to be approximately 1 M^{-1} s^{-1}.[65, 66] The reaction rate exhibits an increase

with the elongation of the toehold length, reaching a saturation point at approximately 6-10 nt (ca. 3×10^6 M^{-1} S^{-1}).[67] Genot *et al.* represented the precise adjustment of the reaction rate by introducing spacers (including ssDNA, dsDNA, or polyethylene glycol) between the toehold and displacement domains of both the substrate and invading strand.[64] Various toehold lengths, ranging from 6 to 14 nts, were employed; and the results showed that the introduction of flexible ssDNA spacers to both substrates and invading strands resulted in a remarkable increase in the reaction rate by over three orders of magnitude. Conversely, the incorporation of rigid dsDNA spacers, led to a reduction in the reaction rate by two or three orders of magnitude. The incorporation of spacers provides a method for precise control over reaction kinetics, offering potential applications in various biotechnological and molecular engineering fields.

(3) Polymerase chain reaction amplification (PCR). PCR is a method for the rapid amplification of specific DNA segments, leading to an exponential increase in the number of oligomers. This process yields millions to billions of copies of the original segments within a short time frame of 20-30 cycles, typically taking only a few minutes, achieved through a series of temperature changes (Figure 1.7c).[68] Key constituents essential for a successful PCR process include the DNA template, DNA polymerase, primers, and deoxynucleotide triphosphates (dNTPs). The DNA template acts as the pre-existing strand that is to be replicated. A thermostable DNA polymerase, commonly exemplified by Taq polymerase, plays a pivotal role in producing new DNA strands during the amplification process. Primers, short DNA strands approximately 20 nts in length, are designed to be complementary to specific regions of the template strand, providing the starting point for the DNA amplification. dNTPs function as the building blocks for the synthesis of new DNA strands, enhancing the incorporation of nucleotides into the growing chain. The PCR process involves a cyclic temperature regimen, typically encompassing denaturation, annealing, and extension steps, ensuring the precise replication of the target DNA segments. PCR finds widespread application in the fields of biology and medicine, such as molecular biology research, acellular cloning, and disease diagnosis.

(4) Commercial synthesis. DNA synthesis achieved commercial viability in the 1980s, followed by the establishment of high-throughput array-based methods in the 1990s.[69] This advancement enables researchers to integrate synthetic genes into diverse fields of biology and medicine, including applications in drug delivery devices, catalytic

reactions, and vaccine development. Promising technologies, such as chemical methods, enzymatic processes, and hybrid approaches, were developed to generate both short DNA chains, termed oligonucleotides, and longer strands with attributes such as high purity, scalability, and cost-effectiveness. The conventional solid-phase chemical reaction, predominantly used for DNA synthesis, imposes limitations on cost-effective synthesis, restricting the attainable length to approximately 200-300 nts. This limitation arises from diminishing yields due to the incorporation of phosphoramidite nucleotides and the use of solvents, leading to the generation of hazardous waste. Subsequently, an alternative enzymatic DNA synthesis strategy has been developed to produce high-molecular-weight ssDNA using a template-free polymerase terminal deoxynucleotidyl transferase (TdT) (Figure 1.7d).[70, 71] TdT is a unique polymerase with the capability of catalyzing the addition of random nucleotides to the 3' end of ssDNA without requiring a template. The enzyme binds reversibly to an oligonucleotide, also known as a "primer", which then combines with the incoming dNTP to form a ternary primer-TdT-dNTP complex. This complex allows the addition of dNTPs to the 3'-hydroxy terminus (3'-OH) of the primer. The molecular weight of the synthesized DNA can be controlled by manipulating the ratio of monomer (dNTPs) to primer, consistent with concepts observed in living polymerization reactions. While the TdT-catalyzed polymerization approach offers advantages such as flexibility, simplicity, and efficiency, its inherent template-free nature limits its ability to produce ssDNA with predetermined, specific sequences. Nevertheless, the rapid and versatile nature of TdT-catalyzed polymerization makes it a valuable tool for DNA synthesis, particularly in applications where sequence specificity is not a primary consideration.

In addition to the template-independent, TdT-mediated polymerization reaction for DNA synthesis, the rolling circle amplification (RCA) technique is another method used for synthesizing long DNA molecules (Figure 1.7e).[72] This approach lies in its requirement for both a DNA polymerase enzyme and a designed circular DNA template. The creation of this circular template, a pivotal element in the RCA process, can be achieved by joining a linear template with a ligation strand through a ligase-mediated reaction. The amplification process begins with the binding of a DNA primer to the circular template, acting as the initiation point for nucleotide addition. Utilizing a DNA polymerase, e.g. Phi29 polymerase, dNTPs are added onto the 3'-end of the primer, guided by the circular template. As the polymerase progresses around the

circular template, it results in the synthesis of an extensive ssDNA molecule. A notable advantage of RCA lies in its ability to significantly amplify signal intensity. Compared to other amplification methods, RCA has the potential to increase the signal strength by approximately 1000-fold to 10000-fold. This feature renders it an incredibly powerful tool for detecting low-abundance DNA sequences, thereby substantially enhancing sensitivity in various molecular biology applications.

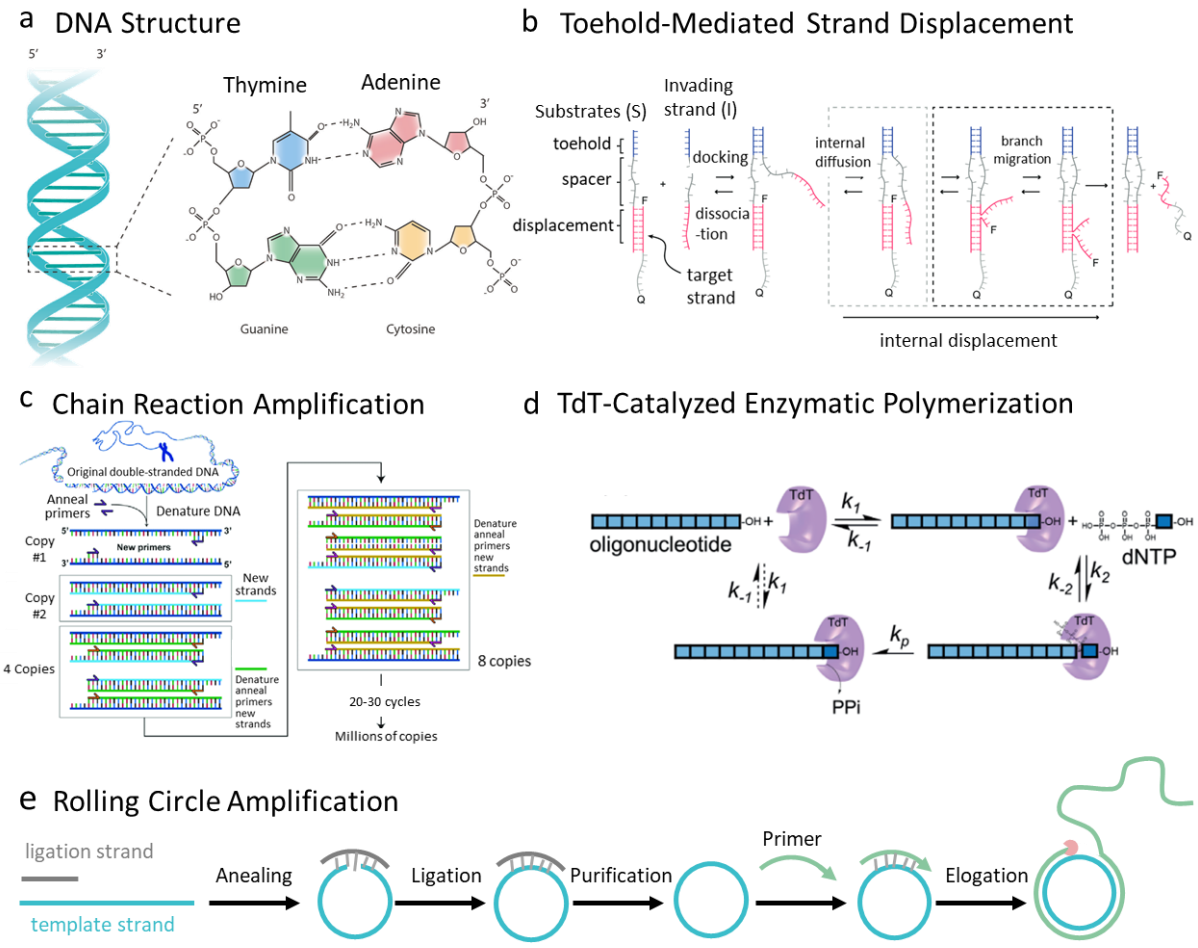

Figure 1.7. DNA characteristics for nanoscience. (a) The double-helical structure of DNA is formed through Watson-Crick base pairing, involving four nucleotide bases: adenine (A), thymine (T), guanine (G), and cytosine (C). Graphics adapted with permission from Ref. *(63)*. **(b)** Toehold-mediated strand displacement: a ssDNA invading strand displaces a target strand from a dsDNA substrate complex. This process begins with an overhang, or toehold, on the dsDNA substrate, which allows the ssDNA invading strand to attach. This attachment initiates a branch migration, resulting in the displacement of the targeted strand from the substrate complex. Graphics adapted with permission from Ref. *(64)*. **(c)** Polymerase chain reaction amplification is used to rapidly make millions to billions of copies of a specific DNA sample. Graphics adapted with permission from Ref. *(68)*. **(d)** Reaction mechanism of TdT-catalyzed polymerization: TdT binds with primer (i.e., oligonucleotide) and dNTP, leading to the formation of elongated DNA strands. Graphics adapted with permission from Ref. *(70)*. **(e)** In the rolling circle amplification technique, a circular DNA template is first prepared. Then, a DNA primer binds to this circular template, initiating enzyme-induced amplification, which results in the formation of a long ssDNA. Graphics adapted with permission from Ref. *(72)*.

1.2.2 DNA-Encapsulated Vesicles

DNA molecules are encapsulated in the lipid bilayers or integrated on the membrane of the lipid vesicles to mimic the characteristics and functions of living cells, including simple protein expression, replication, or growth and division processes. Noireaux *et al.* performed a study where they achieved cell-free protein expression within a phospholipid vesicle.[73] The system encapsulated essential components, including an engineered plasmid DNA, enzymes, and small molecule precursors. The expression of protein within the vesicle was sustained for 5 h, which is more than double the duration observed in bulk solution and resulted in a twofold increase in protein concentration. To address the challenge of low vesicle permeability and to further extend the expression duration, they introduced molecular pores in the membrane. These pores, formed by α-hemolysin – a protein expressed by a second gene – allowed for the influx of new nutrients. This innovative approach enabled the continuation of protein expression for an extended period of up to 4 days.

The process of targeted vesicle fusion, a critical mechanism in living cells, is mediated by the SNARE protein complex on the membrane.[74] This process is vital for reloading substances, extending biological reaction durations, and transporting proteins and lipids between various organelles within the cell. Drawing inspiration from this cellular activity, Stengel *et al.* introduced a vesicle fusion model by incorporating functional DNA strands into the membranes of phospholipid vesicles.[75] The hybridization of these DNA strands induced bilayer contact, thereby driving the fusion process. The efficiency of vesicle fusion can be fine-tuned by modifying DNA architecture and chemistry, leading to efficient mixing of cargoes and control of biological reactions. Building on this concept, Peruzzi *et al.* further demonstrated that DNA-functionalized vesicles could precisely target and delivered cargo to specific vesicle groups via engineering vesicle fusion (Figure 1.8a,b).[76] Additionally, this DNA-mediated fusion has been found to initiate cell-free protein synthesis, thereby enhancing both the control and efficiency of biological reactions within vesicle systems.

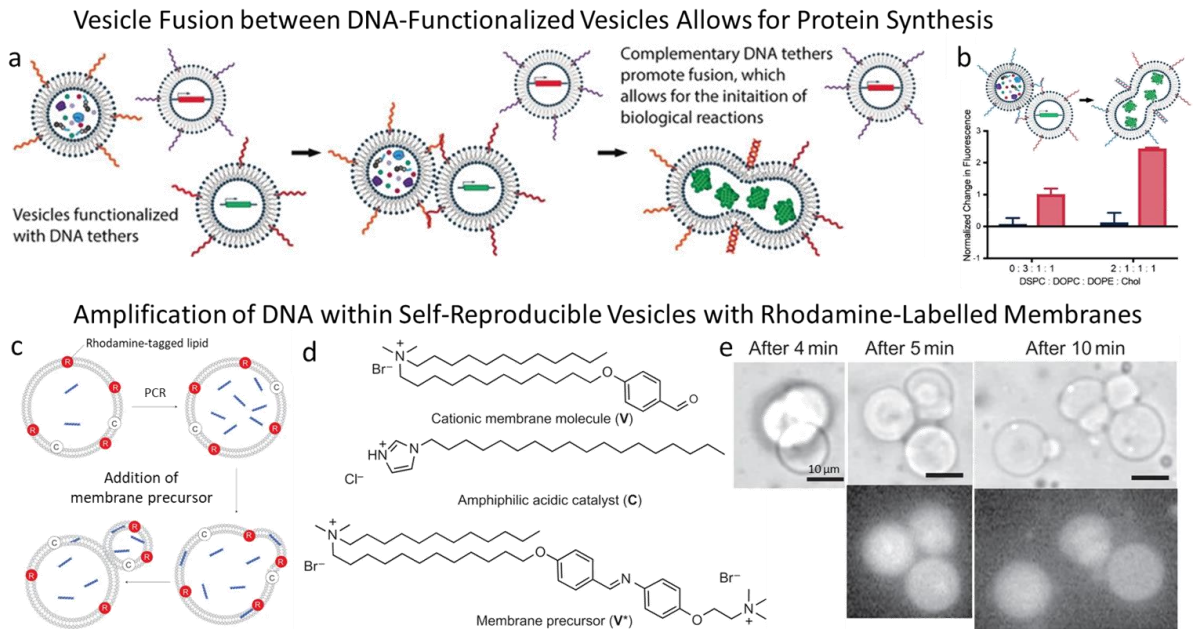

Figure 1.8. Protein synthesis and DNA amplification within vesicles. (a–b) Controlled protein synthesis within vesicles was achieved by DNA-induced vesicle fusion. **(a)** Vesicle membranes were functionalized with specific DNA strands. Vesicles carrying DNA strands that can hybridize with each other facilitated fusion, thereby delivering cargo to targeted vesicles and triggering cell-free protein expression within these vesicles. **(b)** DNA-mediated fusion and membrane composition affected the synthesis of fluorescent proteins. In vesicles without DNA functionalization, protein fluorescence showed slight differences due to the absence of fusion, whereas an increase in protein fluorescence was detected within DNA-functionalized vesicles. Membrane compositions that promote fusion led to enhanced protein production. Graphics adapted with permission from Ref. *(76)*. **(c–e)** DNA amplification in vesicles and inducing growth-and-division of the vesicles. **(c)** Mechanism of vesicle growth and division induced by the presence of amplified DNA. DNA amplification occurred successfully through PCR within Rhodamine-stained vesicles containing molecules V and C. Some DNA molecules adhered to the inner surface of the vesicle membrane due to electrostatic interactions between anionic DNA and cationic V. With the addition of V*, membrane molecule V could be produced catalytically by C. This process resulted in an imbalance in the number of membrane molecules between the inner and outer leaflets, which in turn induced the growth and division of the vesicles. **(d)** Chemical structures of membrane molecule V, catalyst C, and membrane precursor V*. **(e)** Real-time fluorescence microscopy images of morphological changes in the growth and division of vesicles upon the addition of V*. Graphics adapted with permission from Ref. *(80)*.

Self-reproduction is also a vital function in living cells, crucial for maintaining genetic continuity, enhancing cell growth and development, and enabling tissue repair and regeneration. Therefore, the model protocells should possess the capability for self-reproducing the compartment and self-replicating genetic material to accurately mimic these essential biological processes. Researchers have extensively studied the replication and synthesis of informational molecules, namely DNA and RNA, within vesicles.[77-79] For instance, Oberholzer *et al.* presented DNA replication within liposomes using PCR, leveraging the thermal stability of liposomes even under the high temperature necessary for PCR.[77] The coupling of informational molecule replication with vesicle reproduction is crucial for understanding cellular functions. In a pioneering work, Walde *et al.* described the concurrent synthesis of RNA polymers and the self-reproduction of fatty acid vesicles, aided by the addition of membrane

precursors.[79] Based on this, Kurihara *et al.* delved deeper into the mechanisms underlying the amplification of informational molecules, specifically DNA, within a self-reproducible vesicle and examined their impact on vesicle division (Figure 1.8c–e).[80] Their research demonstrated the successful DNA amplification within lipid vesicles using PCR and underscored the essential role of this amplified DNA in the growth-and-division of the vesicles. They discovered that DNA adhering to the inner membrane surface, caused by the accumulation of cationic molecules within the inner leaflet of the lipid bilayer, plays a more pivotal role in driving the growth-and-division of vesicles than the addition of membrane precursor.

1.2.3 DNA-Hybrid Coacervates

Nucleic acids are highly negatively charged molecules, that easily interact with other positively charged molecules in cells. For instance, genomic DNA and histone proteins spontaneously phase separate into chromosomes.[81] Therefore, negatively charged DNA is integrated with various positively charged substances, such as proteins, peptides, amino acids, and synthetic materials, to construct DNA-hybrid cell-like models.[82-84] These materials, bearing opposite charges, spontaneously assemble into liquid-like droplets known as complex coacervates. The formation of these coacervates occurs through LLPS, driven by a range of interactions, like electrostatic attractions, hydrogen bonding, and cation-π interactions. A distinct feature of these coacervates is their molecule-crowded interior, which contrasts with the predominantly water-filled interior of lipid vesicles.

To mimic the molecularly crowded characteristic of cellular environments, Shakya *et al.* employed positively charged protein histones and negatively charged ssDNA to form liquid-like droplets in the presence of Na^+.[85] Their findings indicated that the molecules within these coacervates exhibit non-Fickian diffusion, primarily attributed to cation-π interactions. This observation is significant for advancing our understanding of LLPS behavior, DNA accessibility, and transcription kinetics within living cells. Recognizing the important role of compartmentalization in regulating cellular processes, Lu *et al.* engineered synthetic compartments by strategically combining ssDNA/poly-L-lysine ($PLys(Me)_3$) and ssDNA/GFP-K_{72} coacervates in a saline environment (Figure 1.9a,b).[61] This approach resulted in the formation of a core-shell structure, where the ssDNA/$PLys(Me)_3$ coacervates constituted the inner core, encapsulated by an outer layer of ssDNA/GFP-K_{72} coacervates. This multiphase

coacervate formation is largely attributed to the associated differences in macromolecular density between the two coacervate types. Such an arrangement showcases the potential for creating complex molecular architectures through the strategic combination of different coacervates.

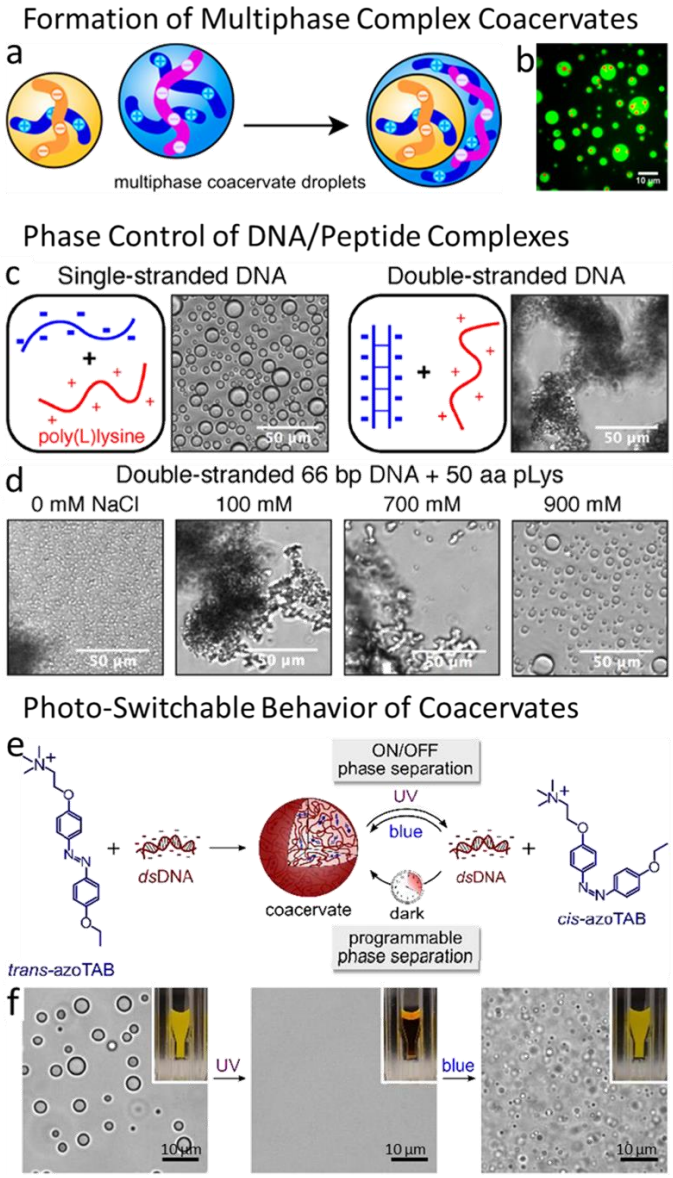

Figure 1.9. Various types of DNA-hybrid coacervates by electrostatic interactions. (a–b) Formation of multiphase complex coacervates through the mixing populations of two different coacervates. The coacervates with the highest interfacial tension tend to be engulfed by another coacervate, leading to the production of multiphase coacervates characterized by a lower total interfacial energy. **(a)** In this process, smaller coacervates are more likely to be engulfed by larger ones. **(b)** Confocal fluorescence microscopy image of ssDNA/PLys(Me)$_3$ core (red) coacervates in a ssDNA/GFP-K$_{72}$ outer (green) coacervate phase. Graphics adapted with permission from Ref. *(61)*. **(c–d)** DNA structures and salt concentration influence the morphologies of DNA/peptide complex. **(c)** ssDNA typically formed liquid coacervates, while dsDNA often resulted in the formation of solid precipitates. **(d)** In the dsDNA/peptide system, the transition from solid to liquid was observed at a NaCl concentration of 900 mM. Graphics adapted with permission from Ref. *(86)*. **(e–f)** Reversible switch of photo-sensitive coacervates formed by combining dsDNA and light-responsive azobenzene cation. **(e)** Scheme of the formation of photo-sensitive coacervates and their disassemble/reassemble behavior under sequential UV/blue light exposure due to azobenzene *trans/cis* photo-isomerization. The reassembly process could also be achieved by treatment in darkness by regulating *cis-trans* thermal relaxation. **(f)** Images of the mixture of dsDNA and azobenzene cation in the dark, under UV light, and blue light. Graphics adapted with permission from Ref. *(84)*.

In addition to ssDNA, dsDNA is also considered for the generation of DNA-hybrid coacervates owing to their markedly distinct properties. ssDNA exhibits flexibility, in contrast to the stiffer nature of dsDNA. This difference in structural properties leads to various outcomes when mixed with cationic peptides: ssDNA tends to form liquid coacervates, whereas dsDNA often results in solid precipitates. Vieregg *et al.* observed similar behavior and further demonstrated the impacts of factors such as polymer length, structure, concentration, and salt concentration on the resultant morphologies when combining oligonucleotides with cationic polymers, including peptides and polyamines (Figure 1.9c,d).[86] Their finding revealed that polymer length and concentration show a modest influence on the formation of coacervates with the ssDNA complex and the generation of precipitates with the dsDNA complex. Notably, an increase in NaCl concentration typically led to larger coacervate sizes, while a solid-liquid transition was observed in the dsDNA system at higher NaCl concentrations. Martin *et al.* successfully synthesized light-responsive coacervates by leveraging electrostatic interactions between dsDNA and an azobenzene cation (Figure 1.9e,f).[84] These coacervates exhibited the unique capability to disassemble and reassemble within just a few seconds under UV and blue light, respectively. This dynamic behavior is attributed to the photo-isomerization of azobenzene, which undergoes *trans/cis* transformations in response to light exposure.

1.2.4 All-DNA Coacervate Droplets

The inherent programmability of DNA enables the creation of desired nanostructures capable of self-assembling into dynamic all-DNA droplets. These droplets include membrane-less coacervates and core/shell protocells, integrating fluid-like properties with DNA programmability.[87, 88] These advantages allow for the precise engineering of the structures, functions, and behaviors of the droplets. As promising cell-like models, all-DNA droplets are entirely composed of DNA and assembled through LLPS in the presence of salt, without the need for additional biomolecules or synthetic polymers. Their formation is driven by a range of weak interactions, such as hydrophobic interactions, π-stacking, π-cation, and hydrogen bonding. Primarily, there are two types of all-DNA droplets: (1) formed through the self-assembly of branched DNA nanostructures, also known as DNA nanostars or branched DNA motifs. This category includes Y- and X-shaped nanostructures (also called Y- and X-motifs), which serve as fundamental building blocks. (2) constructed by the hybridization of polymerized

long DNA strands, either specific ssDNA polymers or multivalent DNA polymers with side chains.

The formation of DNA nanostar-based droplets through LLPS is mediated by the sticky ends of each arm on the nanostars. Each nanostar is composed of three or four dsDNA arms joined at a junction by flexible, unhybridized bases, with palindromic sticky ends (SEs) of ssDNA (Figure 1.10a,b).[89, 90] Appropriate Y-motifs were designed by Sato and co-workers to investigate the formation of DNA droplets during a cooling process from about 95 °C (Figure 1.10b,c).[91] They observed a dispersion at 70 °C, liquid droplets at 62 °C, and solid hydrogels at 25 °C. They demonstrated the effect of temperature and DNA concentration on droplet formation which is reversible by temperature adjustment. The interaction strength among motifs, such as SE sequences and ionic strength, has a key role in the formation and properties of droplets. The common length of SEs used to form droplets is 4 to 12 nt.[91, 92] Higher salt concentration leads to larger and more stable droplets.[93] The dynamics and physical properties of these droplets are also dependent on the nanomechanical and physicochemical properties of the nanostars, such as the branch number, arm length, and structure flexibility.[91, 94, 95]

In addition to the nanostar-based fabrication, our group recently presented that long polymerized ssDNA can successfully form all-DNA droplets. There are two methods: one involves another long ssDNA to stabilize the structure, and the other uses additional short oligonucleotides to bind the structures. As for the former method, two sequence-controlled multiblock ssDNA polymers, p(A_{20}-i) and p(T_{20}-j), were synthesized by RCA and treated with a heating/cooling ramp in the presence of Mg^{2+} (Figure 1.10d,e).[96] This process leads to the formation of protocells with a liquid interior of p(A_{20}-i) trapped by a crosslinked shell of p(A_{20}-i)/p(T_{20}-j). A_{20} and T_{20} refer to homosequences containing 20 nucleobases of adenine and thymine, respectively, while i and j represent barcode segments for functionalization. The protocell formation is attributed to the reversible phase separation of p(A_{20}-i) in the presence of Mg^{2+}, while p(T_{20}-j) does not undergo phase separation. The macromolecularly crowded, liquid-like interior of the protocells allows catalytic signal conversion and induces morphological transformations inside protocells.[97, 98] In addition, parameters including temperature, salt concentration, DNA sequences, and DNA length play an important role in determining the morphological and physical properties of the protocells. For instance, homogenous microgels can be produced by modifying p(A_{20}-i) with a

palindromic XL sequence to form p(A_{20}-i)-XL, due to the intermolecular duplex crosslinks of XL segments.

The other method for constructing all-DNA droplets was also developed by our group, Deng *et al.* demonstrated a concept for the formation of multivalent DNA coacervates, driven by ATP-induced LLPS, using sequence-defined DNA polymers with complementary side chains (Figure 1.10f).[99] These polymers were generated through ATP-powered ligation. By combining this ligation-induced polymerization with endonuclease-mediated depolymerization, it was possible to create transient DNA coacervates. Moreover, the lifetimes of these coacervates could be precisely controlled by modulating the ATP concentration.

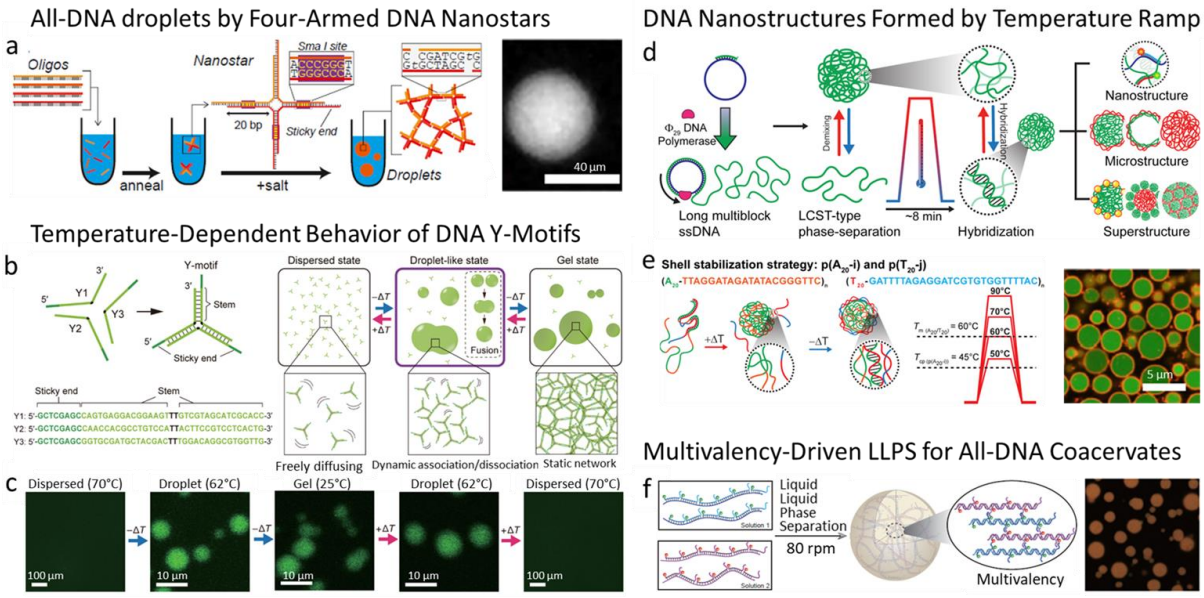

Figure 1.10. Formation of all-DNA coacervate droplets by various DNA designs. (a) Left: Scheme of DNA droplets formed from four-armed DNA nanostars through an annealing process. Right: An image of the formed droplets. Graphics adapted with permission from Ref. *(89)*. **(b–c)** Structure and sequence of Y-motif, along with its reversible state changes in response to different temperatures. **(b)** Y-motifs with palindromic sticky ends were designed to construct all-DNA droplets. At high temperatures, these Y-motifs were in a "dispersed state". As the temperature decreased, they assembled into a "droplet-like state", allowing fusion. Upon further cooling, they transitioned into a "gel state". The temperature threshold for droplet formation was determined by the sequences and concentrations of the DNA. **(c)** Images display the various states of Y-motifs at different temperatures. Graphics adapted with permission from Ref. *(91)*. **(d–e)** Formation of DNA nanostructures from multiblock ssDNA using a temperature ramp method. **(d)** Multiblock ssDNA, synthesized by RCA, underwent phase separation into various nanostructures, such as protocells, capsules, and hydrogels. **(e)** Left: Formation of protocells with liquid-like cores and crosslinked shells by treating a mixture of two DNA polymers, p(A_{20}-i) and p(T_{20}-j), with a heating/cooling ramp. The protocell formation is mainly due to the reversible phase separation of p(A_{20}-i) in the presence of Mg^{2+}, while p(T_{20}-j) doesn't undergo phase separation. The 15 °C difference between the melting temperature of A_{20}/T_{20} ($T_{m(A20/T20)}$ = 60 °C) and the cloud point temperature of p(A_{20}-i) ($T_{cp(p(A20-i))}$ = 45 °C) is important for the protocell formation. Upon heating to 90 °C, p(A_{20}-i) separates into droplets, while p(T_{20}-j) dissolves in the solution. During cooling, rehybridization of A_{20} and T_{20} on the droplet surfaces prevents dissolution of the p(A_{20}-i) cores, leading to the formation of core-shell protocells. Right: Images of protocells. Graphics adapted with permission from Ref. *(96)*. **(f)** Left: Schematic illustration of multivalency-driven LLPS of two DNA systems with complementary side-chain interactions for coacervate formation. Right: Images of formed coacervates. Graphics adapted with permission from Ref. *(99)*.

Fusion represents a key dynamic behavior of DNA nanostar-based droplets, reminiscent of the droplet formation via the LLPS process within living cells. Fusion can occur during the droplet formation when two droplets containing identical SEs come into contact (Figure 1.11a,b).[91] These droplets coalesce into a single, larger droplet, resulting in their growth. This behavior can be attributed to the complementary interaction of the SE and the low surface tension of the droplets. In contrast, droplets with orthogonal sequences in the SE do not show fusion behavior due to the sequence-specific selectivity in droplet interactions.

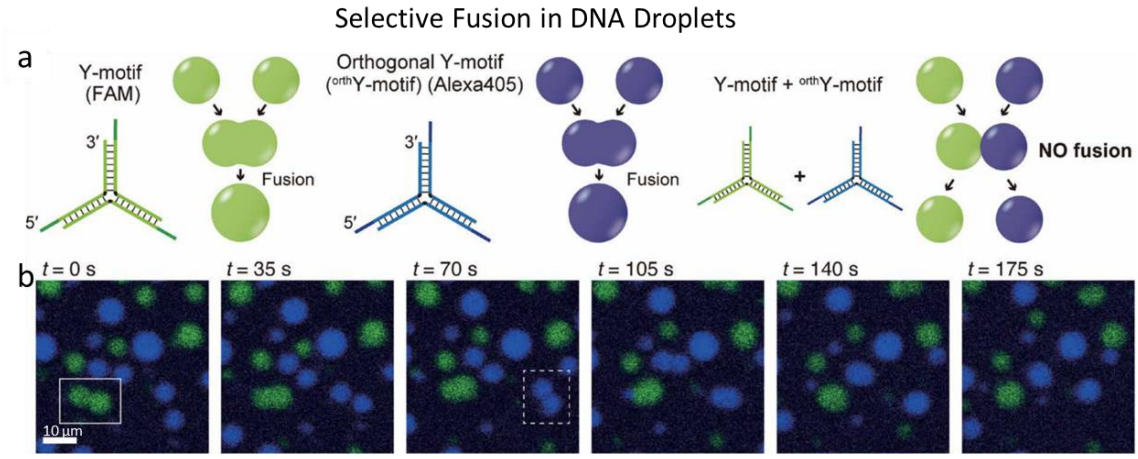

Figure 1.11. **Sequence-dependent selective fusion in DNA droplets. (a)** Schematic representation of selective fusion in droplets containing Y-motif or ^{orth}Y-motif. The sticky end (SE) of the ^{orth}Y-motif is not complementary to the SE of the Y-motif. Fusion only happens between droplets composed of identical motifs, but not between droplets formed by different motifs. **(b)** Time-dependent images of the selective fusion. Graphics adapted with permission from Ref. *(91)*.

Controlling the dynamic behaviors between immiscible DNA droplet systems with orthogonal sequences enables the formation of multi-compartment structures. This mimics the spatiotemporal compartmentalization observed in living cells, which is crucial for biochemical reactions and cellular functionalities due to the creation of segregated microenvironments. Achieving this process involves introducing a DNA linker capable of binding with both of the orthogonal SEs (Figure 1.12a).[100] By adjusting the quantity of the DNA linker, it is possible to form various compartmentalized structures, like Janus-shaped droplets and patchy-like droplets. This variation is achieved through engineering the interfacial free energy between the immiscible phases.

In addition, the enzyme-responsive linker can further regulate the dynamics of droplets, inducing remodeling events, such as Janus-like segregation and fission (Figure 1.12b–d). Sato *et al.* employed S-motif linkers to the system containing two orthogonal Y-

motifs (Y-motif, ^{orth}Y-motif), leading to the formation of dynamic mixed droplets composed of three of these DNA motifs (Figure 1.12b).[91] The S-motif linker is a six-junction motif that can hybridize with the SEs of the two orthogonal Y-motifs, which can act as a cross-bridge for the two orthogonal Y-motifs to decrease the surface tension. To achieve dynamic remodeling, the S-motif was replaced with the CS-motif, which bond to SEs of both Y- and ^{orth}Y-motifs and features specific RNA segments around its center (Figure 1.12c). With the addition of RNase A which can only degrade RNA, the CS motif was gradually cleaved into two portions, inducing the fission of DNA droplets into multiple droplets. The time-dependent images further showed the formation of mixed droplets (t = 0 s) and then gradually separated inside (t = 30 s), resulting in two or three droplets (t = 150 s). This splitting behavior helps to have a better understanding of the biological cellular division and gives a new view for the study of the origin of life. By tunning the mixing ratio of S- and CS-motifs and employing this RNase-induced enzymatic reaction, different compartment structures could be constructed: Janus-like droplets formed at a 90% CS-motif ratio, while patchy-like droplets appeared when the CS-motif ratio was decreased to 50% (Figure 1.12d).

Recently, Saleh *et al.* explored the interactions between droplets and enzymes at the microscopic level.[89, 101] They developed a system for enzyme-induced degradation of DNA droplets by integrating the DNA-cleaving restriction enzyme, SmaI, into the arms of the DNA motifs (Figure 1.12e). Their findings revealed that this droplet degradation is influenced by the dynamic properties of the droplets, particularly about the phase-transition point (i.e., the dissolution temperature T_b). They observed that liquid droplets far from this threshold (T_b-T > 3 °C) form a relatively stable meshwork, causing enzymes to act on the droplet surface due to cleavage occurring before significant penetration. Conversely, when closer to T_b (T_b-T ≈ 3 °C), the liquid meshwork is less stable, allowing for faster enzyme movement and penetration, which outpaces the degradation rate and leads to vacuole formation within the droplets.

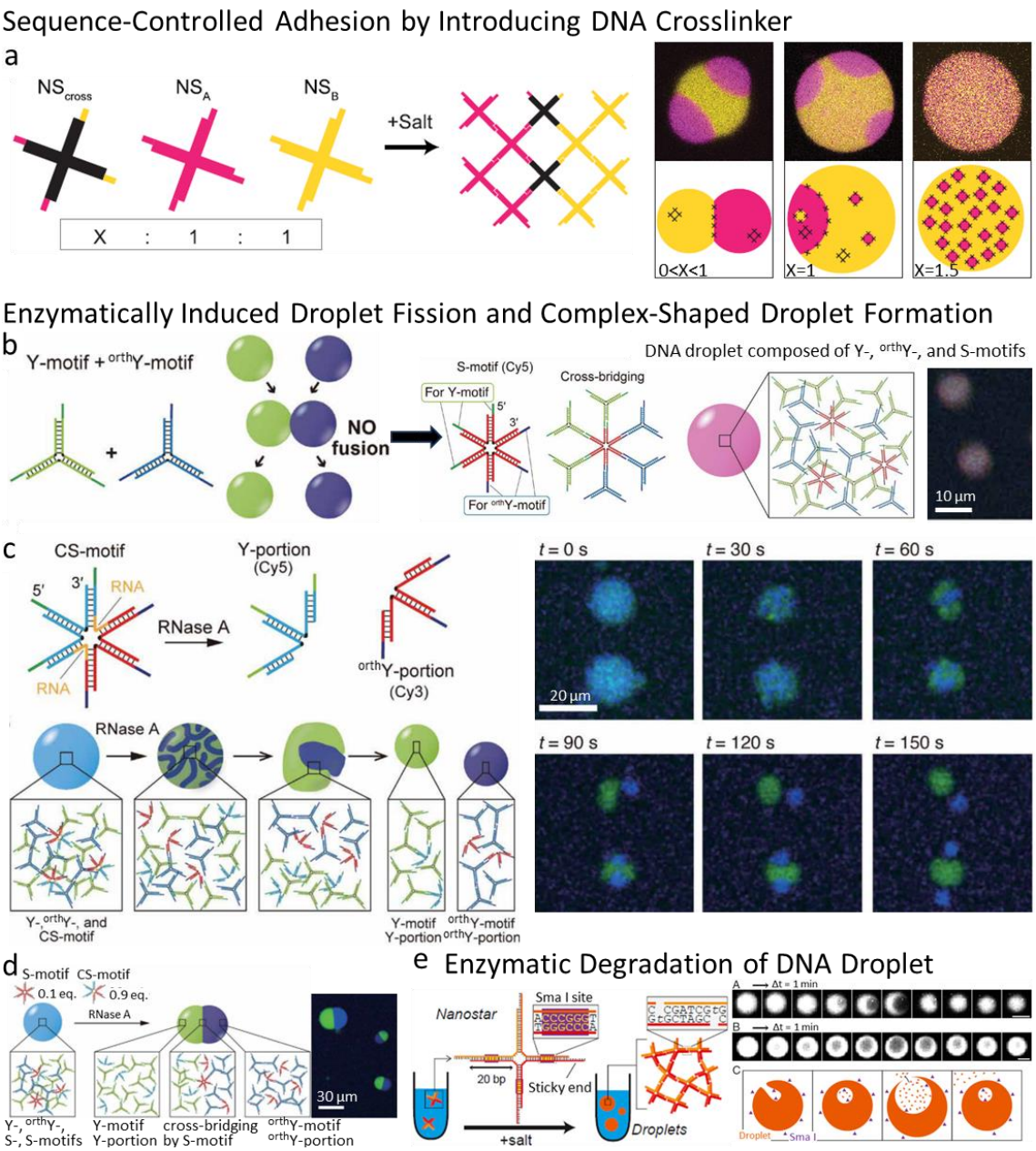

Figure 1.12. Controlled muti-compartmentalization and fission of DNA droplets through the introduction of DNA crosslinkers and enzymatic reactions. (a) Formation of multi-compartment structures by controlling droplet adhesion through the introduction of DNA crosslinker. Three types of droplets were formed: A-type droplets, B-type droplets, and crosslinker droplets, which consist of NS_A nanostars (pink), NS_B nanostars (yellow), and NS_{cross} nanostars, respectively. The NS_A and NS_B nanostars were specifically engineered to possess orthogonal overhangs, while the NS_{cross} nanostars were designed with both overhangs of NS_A and NS_B nanostars. By combining A-type and B-type droplets with crosslinker droplets in varying proportions, a series of multi-compartment structures could be formed. These include Janus-shaped droplets and patchy-like droplets, with the specific structure determined by the ratio of the three droplet types. Graphics adapted with permission from Ref. *(100)*. **(b–d)** Formation of complex-shaped droplets and fission of droplets. **(b)** DNA droplets, containing Y-motif, ^{orth}Y-motif, and S-motif crosslinker, were formed by mixing these three DNA nanostars with the ratio of 3:3:1. **(c)** Droplet fission through enzymatic reaction. Left: Scheme of droplet fission. Droplets were formed by combining CS-motif crosslinker (with DNA-RNA segments) with Y- and ^{orth}Y-motifs. The addition of RNase A, which degrades the RNA parts, caused the CS-motif to divide, separating the Y- and ^{orth}Y-motifs within the droplets, leading to their division into multiple droplets. Right: Real-time images of the RNase-induced droplet fission. **(d)** Janus-like droplets were synthesized by introducing RNase A into the droplets composed of Y-motif, ^{orth}Y-motif, S-motif, and CS-motif. Graphics adapted with permission from Ref. *(101)*. **(e)** Vacuole formation in a DNA droplet was initiated by enzyme-triggered degradation. The enzyme SmaI (purple triangles), penetrated deep into a liquid DNA droplet (orange), producing fragments (orange lines). This process generated osmotic pressure, leading to the creation and expansion of vacuoles. These vacuoles were dynamic, undergoing cycles of growth, popping, and regrowth. Graphics adapted with permission from Ref. *(89, 101)*.

Furthermore, signal transduction via reaction networks within cells and organisms results in downstream functional responses and structural developments. Recently, Samanta *et al.* have advanced this field by integrating catalytic signal processing into highly programmable all-DNA protocells (Figure 1.13).[97, 98] These protocells are characterized by a liquid ssDNA core within a hydrogel-like dsDNA shell, offering a crowded environment for chemical reactions. An RNA-cleaving DNAzyme, a type of specialized DNA oligonucleotide designed for cleaving RNA linkage embedded in a DNA substrate, was encapsulated within these protocells by targeting the core-barcode segment (Figure 1.13a).[98] The catalytic efficiency of the encapsulated DNAzyme was evaluated using a self-reporting substrate (Subs-1) that contains an RNA linkage and a fluorescence resonance energy transfer (FRET) pair (Cy5 and a black hole quencher (BHQ)). The enzymatic action of DNAzyme on this substrate separated the FRET pair, enhancing the fluorescence signal. Comparative analyses revealed that DNAzyme's efficiency in cleaving RNA bonds is about twice as high within the protocells as in solution (Figure 1.13b,c), largely attributed to the crowded conditions within the protocells that mimic natural intracellular environments,[102] potentially optimizing DNAzyme function. This system not only shows the enhanced activity of DNAzyme in protocells but also illustrates the potential of such engineered models to replicate complex biochemical processes.

Moving beyond conventional DNAzyme-catalyzed signal conversion applications, our group further explored non-DNA signal processing within DNA environments by initiating the generation of self-reporting, non-DNA metabolites via ring-closing metathesis (RCM) reactions within DNA protocells (Figure 1.13d–h).[97] To achieve this, artificial metalloenzymes (ArMs) were incorporated into the protocells by initially attaching a complementary biotinylated ssDNA sequence (Biot-m*) to the core-barcode sequence (m). Subsequently, streptavidin (Sav) and a biotinylated olefin metathesis catalyst (Biot-Ru) were introduced (Figure 1.13d), ensuring the immobilization of ArMs which then catalyzed DNA-orthogonal RCM reactions, resulting in the production of a fluorescent umbelliferone signal from a caged precursor (Subs-I) (Figure 1.13e,f). Notably, the resulting fluorescence was detected not only in the core but also in the shell of the protocells, suggesting the successful release and intercalation of the produced metabolite with dsDNA structure[103] (Figure 1.13g). This intercalation process weakens the shell’s dsDNA structure, causing

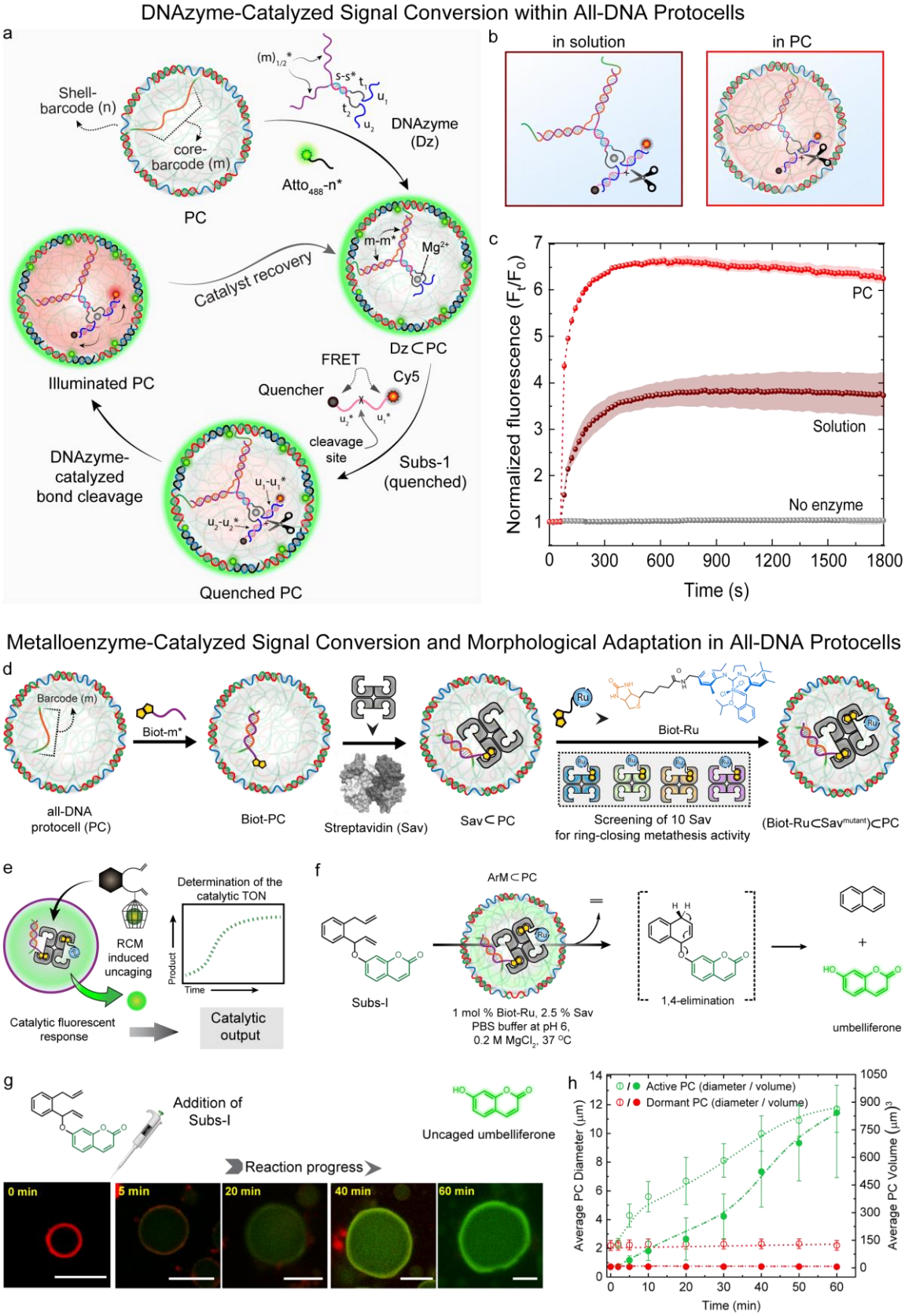

Figure 1.13. **Signal processing and morphological adaption within crowded all-DNA protocells. (a–c)** DNAzyme-mediated signal conversion within protocells. **(a)** DNAzyme-induced cleavage inside protocells by introducing a self-reporting substrate (Subs-1), which consists of an RNA linkage and a FRET pair (Cy5 and BHQ), into the DNAzyme-capsulated protocells. This led to the cleavage of Subs-1 into two parts that melt away due to their low melting temperatures, leading to the separation of Cy5 and BHQ and an increase in fluorescence (magenta). **(b)** Schematic of two scenarios demonstrating DNAzyme-catalyzed cleavage occurring both in solution

and within protocells. **(c)** Time-dependent spectrofluorimetric analysis of DNAzyme-catalyzed cleavage in protocells compared with that in solution, along with a control experiment where the auto-cleavage of Subs-1 is also presented in the absence of DNAzyme (gray trace). Graphics adapted with permission from Ref. *(98)*. **(d–h)** Artificial metalloenzyme (ArM)-catalyzed signal conversion and morphological adaptation in protocells. **(d)** Incorporation of ArM into protocells using biotin-streptavidin (Sav) technology. **(e)** ArM-mediated uncaging reactions within protocells resulted in the generation of a fluorescent signal. **(f)** ArM-catalyzed uncaging of umbelliferone inside the protocells from a caged precursor (Subs-I). **(g)** Time-dependent confocal laser scanning microscopy (CLSM) images of ArM-catalyzed uncaging of umbelliferone (green) in protocells that have their shells labeled (red). Upon the injection of Subs-I, green fluorescence emerged and gradually increased in the core of the protocells. A slight decrease in red fluorescence from the shells was observed, attributed to protocell swelling. **(h)** Time-dependent increases in the size of active and dormant protocells (namely, (Biot-Ru⊂Sav)⊂protocell and Sav⊂protocell). A control experiment in which the catalytic activity was assessed inside protocells without the capsulation of Bio-Ru catalyst (termed dormant protocells). Notably, significant expansion was observed in the active protocells, while dormant protocells exhibited no expansion, underscoring the role of catalytic reactions in inducing protocell growth. Graphics adapted with permission from Ref. *(97)*.

increased membrane dynamics, protocell swelling, and eventual growth (Figure 1.13g,h). These findings present new avenues for investigating life-like behaviors and bioorthogonal chemical transformations within synthetic protocells.

1.3 Liquid-Liquid Phase Separation (LLPS) Applied to Synthetic Cell

Synthetic cells are cell-mimicking compartments that exhibit properties similar to those observed in living organisms. LLPS is essential for the organization and functionality of living cells, contributing to organelle formation, regulation of cellular activities, and involvement in disease mechanisms. Utilizing LLPS in constructing synthetic cells has become a promising strategy, significantly enhancing our understanding of biological principles and behaviors. This approach not only deepens our comprehension of cell biology and the origin of life but also opens up potential avenues for developing disease therapies.[104]

1.3.1 LLPS in Polymer Solutions

In vitro, LLPS forms distinct phases through macromolecular crowding with various biological or synthetic polymers, occurring via segregative or associative mechanisms. Segregative LLPS results in separate phases, each enriched with different macromolecules, while associative phase separation generates a unified phase composed of a mixture of macromolecules (Figure 1.14a,b).[105, 106]

Segregative LLPS, which typically occur in aqueous two-phase systems (ATPS), neutral polymers or polymer-salt mixtures form immiscible phases. A classical ATPS example employs mixtures of dextran and poly(ethylene glycol) (PEG), separating into dextran-rich and PEG-rich phases beyond certain concentration thresholds (Figure 1.14b,c).[107, 108] The separation threshold is influenced by factors such as polymer

molecule weight and temperature; lower molecular weights generally require higher concentrations for phase separation. ATPS properties, such as particle size and viscosity, can be modulated by adjusting polymer molecular weights or ratios of polymer volume, making these systems valuable for biology applications, particularly for extracting cellular components by exploiting phase-specific affinities. For example, hydrophobic components like denatured proteins tend to accumulate in the PEG-rich phase, whereas hydrophilic components including nucleic acids or globular proteins preferentially partition into the dextran-rich phase.[109, 110]

Associative LLPS, alternatively, results in a polymer-rich phase and a dilute supernatant, driven by polymer affinity in a process known as coacervation. This is classified into two categories: simple coacervation and complex coacervation. Simple coacervation involves the desolvation process of a single polymer type, while complex coacervation arises from electrostatic interactions between two oppositely charged polymers. The liquid-like microdroplets produced by complex coacervation are considered protocell models to investigate the prebiotic organization and MLOs.[55] The formation and behavior of these coacervates are also influenced by factors such as pH, which must be optimized to ensure polyelectrolyte charging, as well as ionic strength and temperature, which affect molecular interactions and, consequently, phase separation dynamics.[111, 112]

Understanding phase separation in biological systems is fundamental, and constructing physical phase diagrams is crucial to grasping this concept. These diagrams illustrate various states under a series of conditions, showing the formation and dissolution of phase separation can be effectively controlled by manipulating factors such as polymer composition, pH, or temperature (Figure 1.14c–e). In the binary phase diagram (Figure 1.14e), the binodal line represents the threshold where phase separation becomes thermodynamically feasible, indicating the temperatures and compositions conducive to phase separation.[113] Above this binodal line, the mixture remains a homogenous solution; below it, distinct phases emerge. At lower concentrations, the mixture exists in a single-phase state. Within the binodal line, the spinodal line indicates the boundary between two distinct regions: a metastable region where phase separation initiates by nucleation, and a stable region driven by diffusion. Therefore, there are two main mechanisms for the LLPS: nucleation with subsequent growth; and spinodal decomposition.[114, 115] Nucleation and growth start with the

emergence of minimal phase “nuclei”, which grow into larger distinct regions. In contrast, spinodal decomposition is a spontaneous process occurring within the unstable region, where the mixture separates into distinct phases directly, bypassing the nucleation event.

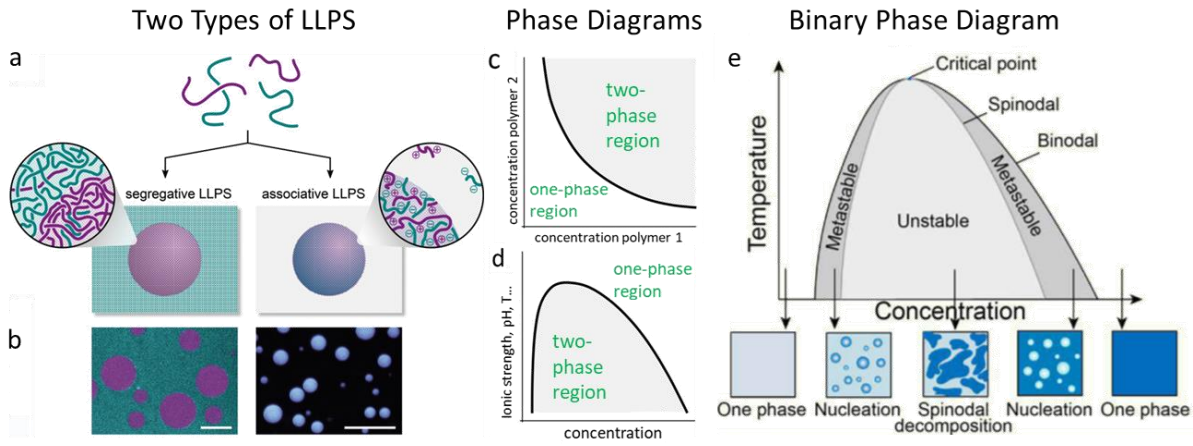

Figure 1.14. Types of liquid-liquid phase separation (LLPS) used in synthetic cells. (a) Scheme of segregative and associative LLPS. Segregative LLPS occurs when two different polymers in a solution segregate into distinct phases, each enriched with one of the polymers. Associative LLPS takes place when two similar polymers in a solution aggregate and form a new, separate phase from the initial solution. **(b)** Images of LLPS-based systems. Left: Image of ATPS, a typical system of segregative LLPS, consisting of PEG (cyan) and dextran (magenta). Right: Image of complex coacervates formed from positively charged polyethyleneimine (PEI) and negatively charged DNA. Graphics adapted with permission from Ref. *(106)*. **(c)** Phase diagram of the ATPS system. Phase separation occurs when polymer concentrations exceed threshold levels. Graphics adapted with permission from Ref. *(107)*. **(d)** Phase diagram of coacervates, illustrating how phase separation is influenced by specific interactions, which are affected by factors like ionic strength, pH, and temperature. Graphics adapted with permission from Ref. *(106)*. **(e)** Phase diagram of two polymers in water, showing the binodal and spinodal curves. Depending on the polymer concentration and environmental stimuli (e.g., temperature, pH), the system can exist as a single phase or segregate into two distinct phases. Graphics adapted with permission from Ref. *(113)*.

1.3.2 LLPS in Living Cells and Synthetic Cells

Compartmentalization is a key fundamental aspect of structural and functional organization in living cells, segregating internal components into distinct compartments or organelles. This spatiotemporal organization plays a vital role in cellular processes, including matter exchanges, energy fluxes, and protein synthesis. Cells feature both membrane-bound organelles and membraneless organelles (MLOs), and each contributes to this compartmentalization. MLOs allow for the free exchange of molecules with the surrounding cytoplasm, as they are not confined by a lipid membrane. The formation and function of MLOs, typically assembled from RNA and proteins, are often driven by LLPS (Figure 1.15a–c).[60] The nucleolus, for example, is a multilayered droplet, enabling smaller droplets to merge into larger entities while maintaining their liquid-like properties (Figure 1.15a,d). This LLPS-driven assembly of the nucleolus from proteins and RNA is reversible, allowing it to disassemble during

events such as cell division or in response to stress.[116, 117] However, dysregulation of LLPS can lead to various diseases, including Amyotrophic Lateral Sclerosis ALS, highlighting its importance in cellular health and disease mechanisms.[118]

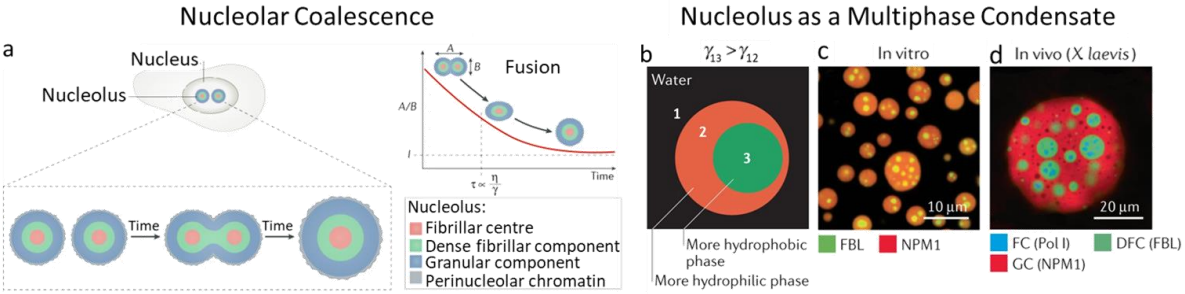

Figure 1.15. Dynamic properties and multiphase structures of nucleolus driven by LLPS. (a) Nucleolar coalescence is a consequence of the liquid dynamic nature of nucleoli, resulting in the formation of larger droplets with minimized surface area. The timescale of coalescence (τ), which is associated with the ratio of effective viscosity (η) and surface tension (γ), can be determined by plotting the aspect ratio of coalescing nucleoli as a function of time. **(b)** Scheme of multiphase droplets. The more effectively hydrophobic liquid (green; 3) possesses a higher surface tension with water (1) compared to the more hydrophilic liquid (red; 2) ($\gamma_{13} > \gamma_{12}$). This difference in surface tension drives the multiphase arrangement, as it minimizes the free energy of the system. **(c)** Droplets composed of the nucleolar proteins (NPM1) and fibrillarin (FBL). **(d)** Example of a large coalesced nucleolus in the *Xenopus laevis* germinal vesicle. Graphics adapted with permission from Ref. *(60)*.

Inspired by the natural LLPS behaviors in living cells, LLPS-based synthetic cells are designed to mimic key properties and functions of biological cells. This approach leverages LLPS as a method for the compartmentalization and organization of biomolecules within synthetic systems. Various LLPS systems have been investigated to understand the processes possibly leading to the emergence of the first cells on Earth. These systems include ATPS,[107] coacervates formed by biomolecules and polymers,[55, 119] and membraneless droplets composed of diverse polymers like polyesters.[120] By studying these models, scientists aim to gain insights into the origins of life. Moreover, compartments constructed through LLPS have been employed in creating synthetic cells, mimicking biological functions including catalytic reactions,[45] droplet engulfment,[61] and even cell growth and division.[53]

1.4 Aim of this Thesis

LLPS is a fundamental phenomenon observed in living cells, driving the organization of biomolecules into liquid condensates and contributing to cellular dynamics and functions. Inspired by this natural process, synthetic LLPS-driven compartments, particularly complex coacervates, have emerged as promising models for studying cellular behaviors and shedding light on the origins of life. Unlike classical synthetic models such as liposomes, polymersomes, and colloidosomes, complex coacervates

present a novel avenue due to their molecularly crowded interiors and dynamic exchanges with the surroundings. While these synthetic systems exhibit basic life-like traits such as maintaining internal molecule environments and responsiveness to external stimuli, understanding the mechanisms governing their formation — both spherical and nonspherical structures — remains a challenge.

DNA has emerged as an attractive building block for the development of coacervates owing to its high programmability and sequence-specificity. Although DNA-based synthetic cells have shown promise, their construction typically requires specific conditions, including additional composition adjustments, annealing processes, or high-temperature treatments, indicating the pathway complexity of the systems. Furthermore, researchers address the general phenomenon of multiphase droplet coexistence observed in living cells, which enables the segregation of different biomolecular processes into separated regions. The mechanisms driving multiphase formation and coexistence remain elusive. To bridge this gap, researchers have endeavored to engineer LLPS-driven multiphase DNA coacervates in vitro, employing inducers like DNA linkers and recognition enzymes. However, the study of multicompartment systems is still at a relatively primary stage, necessitating a robust background in precise DNA sequence design to achieve efficient multicompartmentalization.

Motivated by the groundbreaking research and the significant challenges posed by LLPS-mediated DNA-based synthetic cells, this thesis focuses on fabricating DNA coacervate systems. These systems employ metal-dependent or multivalency-driven LLPS of ssDNA components to precisely control dynamics and structures through simple strategies, advancing our understanding of cellular behaviors and biological functions. The development of such easy-to-use model systems hinges upon the modulation of LLPS behaviors by DNA strands within synthetic constructs. Achieving this goal represents some challenges in this thesis, including understanding the phase transition mechanisms, attaining transient coacervation, and manipulating compartment morphologies in a tunable manner. The subsequent section will provide a detailed overview of the projects included in this thesis, along with an overall layout of its structure.

1.5 Thesis Outline

This thesis focuses on the design and development of cell-like models that exhibit dynamic and controllable attributes, aiming to mimic the organizational and functional complexities of living cells. Inspired by natural LLPS-driven organelles, the creation of bioinspired LLPS systems has gained much ground, enhancing our understanding of biological systems. This thesis introduces the formation and functions of all-DNA coacervate droplets through DNA demixing behavior and demonstrates how to leverage synergies between the DNA world and synthetic amphiphilic copolymers to create switchable hydrophobic compartments. It provides an in-depth analysis of the mechanisms underlying the synthetic system formation and their applications across various fields, ranging from information exchange to catalytic microreactor operations.

Chapter 1 provides an introduction to the construction of synthetic cells, leveraging both synthetic and natural components through a bottom-up approach. This chapter elaborates on the formation, properties, and functions of synthetic models by classifying them based on their components and structural configurations. It also includes a detailed comparison of LLPS in different mediums, including polymer solution, biological cells, and synthetic cells.

Chapter 2 presents mechanistic insights into two different metal ion-dependent phase separations (Ca^{2+} vs. Mg^{2+}) of ssDNA, enhancing the straightforward formation of all-DNA coacervate droplets (Figure 1.16a,b). This opens new avenues for designing systems that enable information exchange between coacervates. Critical factors influencing droplet morphology, such as ssDNA chain length, [Ca^{2+}], and temperature, are thoroughly discussed.

Building on the foundations laid in Chapter 2, **Chapter 3** explores the development of Mg^{2+}-mediated DNA core/shell protocells, which serve as protocell models. This chapter highlights the subcompartmentalization within synthetic cells by incorporating a temperature-responsive DNA-*b*-polymer copolymer into all-DNA core/shell protocell models, in which the temperature-induced phase segregation of the synthetic copolymer leads to the formation of artificial organelle structures depending on the viscoelastic properties of the protocell interior (Figure 1.16c). These hydrophobic subcompartments are designed to act as reaction crucibles, enhancing bimolecular reactions.

In **Chapter 4**, the thesis demonstrates a simple approach for creating multivalency-driven coacervates using long ssDNA homopolymers combined with palindromic binders, introducing a synthetic and programmable coacervate droplet system (Figure 1.16d). This chapter reveals the influence of the length and sequence of the multivalent binders on coacervate formation and discusses methods to introduce switching and autonomous behavior in reaction circuits, as well as techniques to engineer wetting, engulfment, and fusion in multi-coacervate systems, all at physiological temperatures.

Chapter 5 concludes the thesis by summarizing the main findings and offering insights into potential future directions of the research.

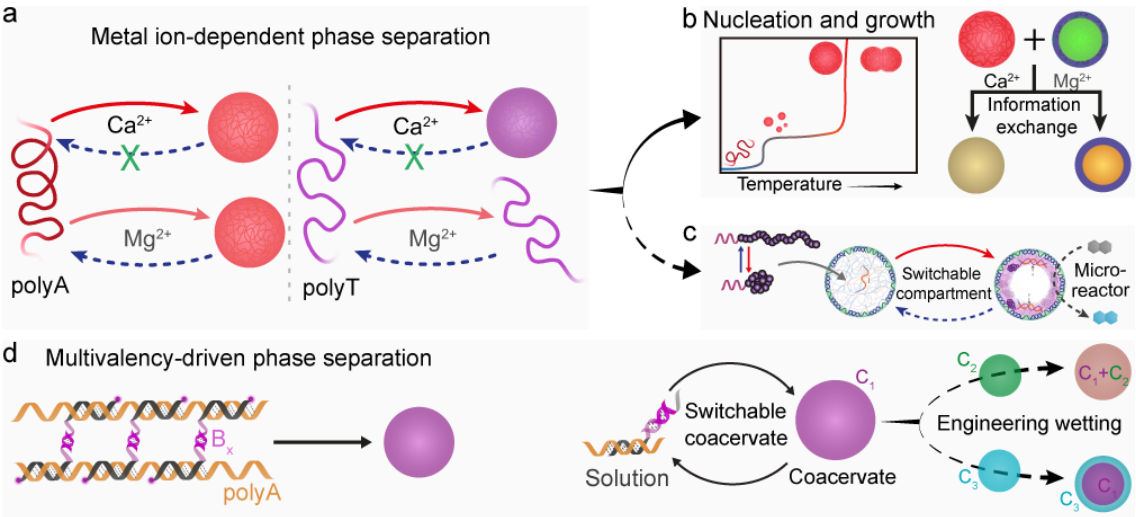

Figure 1.16. Graphical abstract of this thesis. (a) Phase separation of ssDNA with Ca^{2+} and Mg^{2+} ions via a temperature ramp. polyA undergoes irreversible phase separation with Ca^{2+} and reversible phase separation with Mg^{2+}. Phase separation of polyT occurs only in the presence of Ca^{2+} and not for Mg^{2+}. **(b)** DNA droplets can be formed by a two-stage phase separation of polyA via the Ca^{2+}-pathway. Pathway-controlled information exchange by mingling interactions of droplet and protocell mixtures by Ca^{2+}-pathway and Mg^{2+}-pathway. **(c)** Switchable hydrophobic compartments in DNA protocells enhance chemical conversion. **(d)** Multivalency-driven DNA coacervate for engineering wetting, engulfment, and switchable behavior.

1.6 References

1. Xu, C., Hu, S. & Chen, X. Artificial cells: from basic science to applications. *Mater. Today* **19**, 516-532 (2016).
2. Spoelstra, W.K., Deshpande, S. & Dekker, C. Tailoring the appearance: what will synthetic cells look like? *Curr. Opin. Biotechnol.* **51**, 47-56 (2018).
3. Jack W. Szostak, David P. Bartel & Luisi, P.L. Synthesizing life. *Nature* **409**, 387-390 (2001).
4. Solé, R.V. Evolution and self-assembly of protocells. *Int. J. Biochem. Cell Biol.* **41**, 274-284 (2009).
5. Elsana, H. et al. Evaluation of novel cationic gene based liposomes with cyclodextrin prepared by thin film hydration and microfluidic systems. *Sci. Rep.* **9**, 15120 (2019).
6. Filipczak, N., Pan, J., Yalamarty, S.S.K. & Torchilin, V.P. Recent advancements in liposome technology. *Adv. Drug Deliv. Rev.* **156**, 4-22 (2020).
7. Al-Amin, M.D. et al. Dexamethasone Loaded Liposomes by Thin-Film Hydration and Microfluidic Procedures: Formulation Challenges. *Int. J. Mol. Sci.* **21**, 1611 (2020).

8. Cai, X. et al. Multifunctional Liposome: A Bright AIEgen-Lipid Conjugate with Strong Photosensitization. *Angew. Chem. Int. Ed.* **57**, 16396-16400 (2018).
9. Sadownik, A., Stefely, J. & Regen, S.L. Polymerized Liposomes Formed under Extremely Mild Conditions. *J. Am. Chem. Soc.* **108**, 7789-7791 (1986).
10. Estes, D.J. & Mayer, M. Electroformation of giant liposomes from spin-coated films of lipids. *Colloids Surf. B Biointerfaces* **42**, 115-123 (2005).
11. Deng, N.N., Yelleswarapu, M. & Huck, W.T. Monodisperse Uni- and Multicompartment Liposomes. *J. Am. Chem. Soc.* **138**, 7584-7591 (2016).
12. Deshpande, S. & Dekker, C. On-chip microfluidic production of cell-sized liposomes. *Nat. Protoc.* **13**, 856-874 (2018).
13. Lombardo, D. & Kiselev, M.A. Methods of Liposomes Preparation: Formation and Control Factors of Versatile Nanocarriers for Biomedical and Nanomedicine Application. *Pharmaceutics* **14**, 543 (2022).
14. Lopez-Pinto, J.M., Gonzalez-Rodriguez, M.L. & Rabasco, A.M. Effect of cholesterol and ethanol on dermal delivery from DPPC liposomes. *Int. J. Pharm.* **298**, 1-12 (2005).
15. Harries, D., May, S., Gelbart, W.M. & Ben-Shaul, A. Structure, Stability, and Thermodynamics of Lamellar DNA-Lipid Complexes. *Biophys. J.* **75**, 159-173 (1998).
16. Sułkowski, W.W., Pentak, D., Nowak, K. & Sułkowska, A. The influence of temperature, cholesterol content and pH on liposome stability. *J. Mol. Struct.* **744-747**, 737-747 (2005).
17. Deshpande, S., Spoelstra, W.K., van Doorn, M., Kerssemakers, J. & Dekker, C. Mechanical Division of Cell-Sized Liposomes. *ACS Nano* **12**, 2560-2568 (2018).
18. Oberholzer, T.A., M. & Luisi, P.L. Polymerase chain reaction in liposomes. *Chem. Biol.* **2**, 677-682 (1995).
19. Gao, X. & Huang, L. Cytoplasmic expression of a reporter gene by co-delivery of T7 RNA polymerase and T7 promoter sequence with cationic liposomes. *Nucleic Acids Res.* **21**, 2867-2872 (1993).
20. Chakrabarti, A.C., Breaker, R.R., Joyce, G.F. & Deamer, G.F. Production of RNA by a Polymerase Protein Encapsulated Within Phospholipid Vesicles. *J. Mol. Evol.* **39**, 555-559 (1994).
21. Yu, W. et al. Synthesis of Functional Protein in Liposome. *J. Biosci. Bioeng.* **92**, 590-593 (2001).
22. Zhang, Z. et al. Functionalization and higher-order organization of liposomes with DNA nanostructures. *Nat. Commun.* **14**, 5256 (2023).
23. Herbert, F.C. et al. Stabilization of supramolecular membrane protein-lipid bilayer assemblies through immobilization in a crystalline exoskeleton. *Nat. Commun.* **12**, 2202 (2021).
24. Raju, R., Abuwatfa, W.H., Pitt, W.G. & Husseini, G.A. Liposomes for the Treatment of Brain Cancer—A Review. *Pharmaceuticals* **16**, 1056 (2023).
25. Morigaki, K. & Walde, P. Fatty acid vesicles. *Curr. Opin. Colloid Interface Sci.* **12**, 75-80 (2007).
26. Hargreaves, W., Mulvihill, S. & Deamer, D. Synthesis of phospholipids and membranes in prebiotic conditions. *Nature* **266**, 78-80 (1977).
27. McCollom, T.M., Ritter, G. & Simoneit, B.R. Lipid synthesis under hydrothermal conditions by Fischer-Tropsch-type reactions. *Orig. Life Evol. Biosph.* **29**, 153-166 (1999).
28. Deamer, D.W. & Oro, J. Role of lipids in prebiotic structures. *Biosystems* **12**, 167-175 (1980).
29. Cistola, D.P., Hamilton, J.A., Jackson, D. & Small, D.M. Ionization and Phase Behavior of Fatty Acids in Water: Application of the Gibbs Phase Rule. *Biochemistry* **27**, 1881-1888 (1988).
30. Gebicki, J. & Hicks, M. Ufasomes are Stable Particles surrounded by Unsaturated Fatty Acid Membranes. *Nature* **243**, 232-234 (1973).
31. Hargreaves, W.R. & Deamer, D.W. Liposomes from Ionic, Single-Chain Amphiphiles. *Biochemistry* **17**, 3759-3768 (1978).
32. Adamala, K. & Szostak, J.W. Nonenzymatic template-directed RNA synthesis inside model protocells. *Science* **342**, 1098-1100 (2013).
33. Zhang, L. & Eisenberg, A. Multiple Morphologies of "Crew-Cut" Aggregates of Polystyrene-b-poly(acrylic acid) Block Copolymers. *Science* **268**, 1728-1731 (1995).
34. Discher, B.M. et al. Polymersomes: tough vesicles made from diblock copolymers. *Science* **284**, 1143-1146 (1999).
35. LoPresti, C., Lomas, H., Massignani, M., Smart, T. & Battaglia, G. Polymersomes: nature inspired nanometer sized compartments. *J. Mater. Chem.* **19**, 3576-3590 (2009).
36. Lefley, J., Waldron, C. & Becer, C.R. Macromolecular design and preparation of polymersomes. *Polym. Chem.* **11**, 7124-7136 (2020).
37. Lee, J.C.-M. et al. Preparation, stability, and in vitro performance of vesicles made with diblock copolymers. *Biotech. Bioeng.* **73**, 135-145 (2001).

38. Vriezema, D.M. et al. Vesicles and Polymerized Vesicles from Thiophene-Containing Rod–Coil Block Copolymers. *Angew. Chem. Int. Ed.* **42**, 772-776 (2003).
39. Lee, J.S. & Feijen, J. Polymersomes for drug delivery: design, formation and characterization. *J. Control. Release* **161**, 473-483 (2012).
40. Che, H. & van Hest, J.C.M. Adaptive Polymersome Nanoreactors. *ChemNanoMat* **5**, 1092-1109 (2019).
41. Che, H. & van Hest, J.C.M. Stimuli-responsive polymersomes and nanoreactors. *J. Mater. Chem. B* **4**, 4632-4647 (2016).
42. Luo, Y. et al. Polymer Vesicles with Integrated Photothermal Responsiveness. *J. Am. Chem. Soc.* **145**, 20073-20080 (2023).
43. Zhu, Y., Cao, S., Huo, M., van Hest, J.C.M. & Che, H. Recent advances in permeable polymersomes: fabrication, responsiveness, and applications. *Chem. Sci.* **14**, 7411-7437 (2023).
44. Gouveia, M.G. et al. Polymersome-based protein drug delivery - quo vadis? *Chem. Soc. Rev.* **52**, 728-778 (2023).
45. Che, H., Cao, S. & van Hest, J.C.M. Feedback-Induced Temporal Control of "Breathing" Polymersomes To Create Self-Adaptive Nanoreactors. *J. Am. Chem. Soc.* **140**, 5356-5359 (2018).
46. Rowland, R.N. & Woodley, J.F. The stability of liposomes in vitro to pH, bile salts and pancreatic lipase. *Biochim. Biophys. Acta* **620**, 400-409 (1980).
47. Le Meins, J.F., Schatz, C., Lecommandoux, S. & Sandre, O. Hybrid polymer/lipid vesicles: state of the art and future perspectives. *Mater. Today* **16**, 397-402 (2013).
48. Khan, S., McCabe, J., Hill, K. & Beales, P.A. Biodegradable hybrid block copolymer - lipid vesicles as potential drug delivery systems. *J. Colloid Interface Sci.* **562**, 418-428 (2020).
49. Thompson, K.L., Williams, M. & Armes, S.P. Colloidosomes: synthesis, properties and applications. *J. Colloid Interface Sci.* **447**, 217-228 (2015).
50. Park, J.H. et al. Colloidosomes as a Protocell Model: Engineering Life-Like Behaviour through Organic Chemistry. *Eur. J. Org. Chem.* **2022**, e202200968 (2022).
51. Li, M., Harbron, R.L., Weaver, J.V., Binks, B.P. & Mann, S. Electrostatically gated membrane permeability in inorganic protocells. *Nat. Chem.* **5**, 529-536 (2013).
52. Sun, S. et al. Chemical Signaling and Functional Activation in Colloidosome-Based Protocells. *Small* **12**, 1920-1927 (2016).
53. Li, M., Huang, X. & Mann, S. Spontaneous growth and division in self-reproducing inorganic colloidosomes. *Small* **10**, 3291-3298 (2014).
54. Yewdall, N.A., André, A.A.M., Lu, T. & Spruijt, E. Coacervates as models of membraneless organelles. *Curr. Opin. Colloid Interface Sci.* **52**, 101416 (2021).
55. Koga, S., Williams, D.S., Perriman, A.W. & Mann, S. Peptide-nucleotide microdroplets as a step towards a membrane-free protocell model. *Nat. Chem.* **3**, 720-724 (2011).
56. Donau, C. et al. Active coacervate droplets as a model for membraneless organelles and protocells. *Nat. Commun.* **11**, 5167 (2020).
57. Wei, M.T. et al. Phase behaviour of disordered proteins underlying low density and high permeability of liquid organelles. *Nat. Chem.* **9**, 1118-1125 (2017).
58. Alberti, S. & Dormann, D. Liquid-Liquid Phase Separation in Disease. *Annu. Rev. Genet.* **53**, 171-194 (2019).
59. Sawyer, I.A., Sturgill, D. & Dundr, M. Membraneless nuclear organelles and the search for phases within phases. *WIREs RNA* **10**, e1514 (2019).
60. Lafontaine, D.L.J., Riback, J.A., Bascetin, R. & Brangwynne, C.P. The nucleolus as a multiphase liquid condensate. *Nat. Rev. Mol. Cell Biol.* **22**, 165-182 (2021).
61. Lu, T. & Spruijt, E. Multiphase Complex Coacervate Droplets. *J. Am. Chem. Soc.* **142**, 2905-2914 (2020).
62. Dzieciol, A.J. & Mann, S. Designs for life: protocell models in the laboratory. *Chem. Soc. Rev.* **41**, 79-85 (2012).
63. Watson, J.D. & Crick, F.H.C. Molecular Structure of Nucleic Acids: A Structure for Deoxyribose Nucleic Acid. *Nature* **171**, 737-738 (1953).
64. Genot, A.J., Zhang, D.Y., Bath, J. & Turberfield, A.J. Remote toehold: a mechanism for flexible control of DNA hybridization kinetics. *J. Am. Chem. Soc.* **133**, 2177-2182 (2011).
65. Reynaldo, L.P., Vologodskii, A.V., Neri, B.P. & Lyamichev, V.I. The kinetics of oligonucleotide replacements. *J. Mol. Biol.* **297**, 511-520 (2000).
66. Zhang, D.Y. & Winfree, E. Control of DNA Strand Displacement Kinetics Using Toehold Exchange. *J. Am. Chem. Soc.* **131**, 17303-17314 (2009).
67. Yurke, B. & Mills, A.P. Using DNA to Power Nanostructures. *Genet. Program. Evol. Mach.* **4**, 111-122 (2003).

68. Waters, A. & Lemaire, M. in D.F. Geary, F. Schaefer (eds.) Pediatric Kidney Disease 107-149 (2016).
69. Kosuri, S. & Church, G.M. Large-scale de novo DNA synthesis: technologies and applications. *Nat. Methods* **11**, 499-507 (2014).
70. Palluk, S. et al. De novo DNA synthesis using polymerase-nucleotide conjugates. *Nat. Biotechnol.* **36**, 645-650 (2018).
71. Tang, L., Navarro, L.A., Jr., Chilkoti, A. & Zauscher, S. High-Molecular-Weight Polynucleotides by Transferase-Catalyzed Living Chain-Growth Polycondensation. *Angew. Chem. Int. Ed.* **56**, 6778-6782 (2017).
72. Liu, D., Daubendiek, S.L., Zillman, M.A., Ryan, K. & Kool, E.T. Rolling Circle DNA Synthesis: Small Circular Oligonucleotides as Efficient Templates for DNA Polymerases. *J. Am. Chem. Soc.* **118**, 1587-1594 (1996).
73. Noireaux , V. & Libchaber, A. A vesicle bioreactor as a step toward an artificial cell assembly. *PNAS* **101**, 17669-17674 (2004).
74. Jahn, R., Lang, T. & Sudhof, T.C. Membrane Fusion. *Cell* **112**, 519-533 (2003).
75. Stengel, G., Zahn, R. & Hook, F. DNA-Induced Programmable Fusion of Phospholipid Vesicles. *J. Am. Chem. Soc.* **129**, 9584-9585 (2007).
76. Peruzzi, J.A., Jacobs, M.L., Vu, T.Q., Wang, K.S. & Kamat, N.P. Barcoding Biological Reactions with DNA-Functionalized Vesicles. *Angew. Chem. Int. Ed.* **58**, 18683-18690 (2019).
77. Oberholzer, T., Albrizio, M. & Albrizio, P.L. Polymerase chain reaction in liposomes. *Chem. Biol.* **2**, 677-682 (1995).
78. Mansy, S.S. et al. Template-directed synthesis of a genetic polymer in a model protocell. *Nature* **454**, 122-125 (2008).
79. Walde, P., Goto, A., Monnard, P., Wessicken, M. & Luisi, P.L. Oparin's Reactions Revisited: Enzymatic Synthesis of Poly(adenylic acid) in Micelles and Self-Reproducing Vesicles. *J. Am. Chem. Soc.* **116**, 7541-7547 (1994).
80. Kurihara, K. et al. Self-reproduction of supramolecular giant vesicles combined with the amplification of encapsulated DNA. *Nat. Chem.* **3**, 775-781 (2011).
81. Bloomfield, V.A. DNA condensation. *Curr. Opin. Struct. Biol.* **6**, 334-341 (1996).
82. Fraccia, T.P. & Jia, T.Z. Liquid Crystal Coacervates Composed of Short Double-Stranded DNA and Cationic Peptides. *ACS Nano* **14**, 15071-15082 (2020).
83. Kamagata, K., Kusano, R., Kanbayashi, S., Banerjee, T. & Takahashi, H. Single-molecule characterization of target search dynamics of DNA-binding proteins in DNA-condensed droplets. *Nucleic Acids Res.* **51**, 6654-6667 (2023).
84. Martin, N. et al. Photoswitchable Phase Separation and Oligonucleotide Trafficking in DNA Coacervate Microdroplets. *Angew. Chem. Int. Ed.* **58**, 14594-14598 (2019).
85. Shakya, A. & King, J.T. Non-Fickian Molecular Transport in Protein–DNA Droplets. *ACS Macro Letters* **7**, 1220-1225 (2018).
86. Vieregg, J.R. et al. Oligonucleotide-Peptide Complexes: Phase Control by Hybridization. *J. Am. Chem. Soc.* **140**, 1632-1638 (2018).
87. Udono, H., Gong, J., Sato, Y. & Takinoue, M. DNA Droplets: Intelligent, Dynamic Fluid. *Adv. Biol.* **7**, e2200180 (2023).
88. Takinoue, M. DNA droplets for intelligent and dynamical artificial cells: from the viewpoint of computation and non-equilibrium systems. *Interface Focus* **13**, 20230021 (2023).
89. Saleh, O.A., Wilken, S., Squires, T.M. & Liedl, T. Vacuole dynamics and popping-based motility in liquid droplets of DNA. *Nat. Commun.* **14**, 3574 (2023).
90. Biffi, S. et al. Phase behavior and critical activated dynamics of limited-valence DNA nanostars. *PNAS* **110**, 15633-15637 (2013).
91. Sato, Y., Sakamoto, T. & Takinoue, M. Sequence-based engineering of dynamic functions of micrometer-sized DNA droplets. *Sci. Adv.* **6**, eaba3471 (2020).
92. Sato, Y. & Takinoue, M. Sequence-dependent fusion dynamics and physical properties of DNA droplets. *Nanoscale Adv.* **5**, 1919-1925 (2023).
93. Jeon, B.J. et al. Salt-dependent properties of a coacervate-like, self-assembled DNA liquid. *Soft Matter* **14**, 7009-7015 (2018).
94. Agarwal, S., Osmanovic, D., Klocke, M.A. & Franco, E. The Growth Rate of DNA Condensate Droplets Increases with the Size of Participating Subunits. *ACS Nano* **16**, 11842-11851 (2022).
95. Do, S., Lee, C., Lee, T., Kim, D. & Shin, Y. Engineering DNA-based synthetic condensates with programmable material properties, compositions, and functionalities. *Sci. Adv.* **8**, eabj1771 (2022).
96. Merindol, R., Loescher, S., Samanta, A. & Walther, A. Pathway-controlled formation of mesostructured all-DNA colloids and superstructures. *Nat. Nanotechnol.* **13**, 730-738 (2018).

97. Samanta, A., Sabatino, V., Ward, T.R. & Walther, A. Functional and morphological adaptation in DNA protocells via signal processing prompted by artificial metalloenzymes. *Nat. Nanotechnol.* **15**, 914-921 (2020).
98. Samanta, A., Horner, M., Liu, W., Weber, W. & Walther, A. Signal-processing and adaptive prototissue formation in metabolic DNA protocells. *Nat. Commun.* **13**, 3968 (2022).
99. Deng, J. & Walther, A. Programmable and Chemically Fueled DNA Coacervates by Transient Liquid-Liquid Phase Separation. *Chem* **6**, 3329-3343 (2020).
100. Jeon, B.J., Nguyen, D.T. & Saleh, O.A. Sequence-Controlled Adhesion and Microemulsification in a Two-Phase System of DNA Liquid Droplets. *J. Phys. Chem. B* **124**, 8888-8895 (2020).
101. Saleh, O.A., Jeon, B.J. & Liedl, T. Enzymatic degradation of liquid droplets of DNA is modulated near the phase boundary. *PNAS* **117**, 16160-16166 (2020).
102. Ludwanowski, S., Samanta, A., Loescher, S., Barner-Kowollik, C. & Walther, A. A Modular Fluorescent Probe for Viscosity and Polarity Sensing in DNA Hybrid Mesostructures. *Adv. Sci.* **8**, 2003740 (2020).
103. Ou, C.N., Tsai, C.H., Tsai, K.J. & Song, P.S. Photobinding of 8-Methoxypsoralen and 5,7-Dimethoxycoumarin to DNA and Its Effect on Template Activity. *Biochemistry* **17**, 1047-1053 (1978).
104. Spruijt, E. Open questions on liquid-liquid phase separation. *Commun. Chem.* **6**, 23 (2023).
105. Piculell, L. & Lindman, B. Association and segregation in aqueous polymer/polymer, polymer/surfactant, and surfactant/surfactant mixtures: similarities and differences. *Adv. Colloid Interface Sci.* **41**, 149-178 (1992).
106. Martin, N. Dynamic Synthetic Cells Based on Liquid-Liquid Phase Separation. *Chembiochem* **20**, 2553-2568 (2019).
107. Keating, C.D. Aqueous Phase Separation as a Possible Route to Compartmentalization of Biological Molecules. *Acc. Chem. Res.* **45**, 2114-2124 (2012).
108. Stenekes, R.J.H., Franssen, O., Bommel, E.M.G. & Crommelin, W.E. The use of aqueous PEG/dextran phase separation for the preparation of dextran microspheres. *Int. J. Pharm.* **183**, 29-32 (1999).
109. Strulson, C.A., Molden, R.C., Keating, C.D. & Bevilacqua, P.C. RNA catalysis through compartmentalization. *Nat. Chem.* **4**, 941-946 (2012).
110. Long, M.S. & Keating, C.D. Nanoparticle Conjugation Increases Protein Partitioning in Aqueous Two-Phase Systems. *Anal. Chem.* **78**, 379-386 (2006).
111. Krishna Kumar, R., Harniman, R.L., Patil, A.J. & Mann, S. Self-transformation and structural reconfiguration in coacervate-based protocells. *Chem. Sci.* **7**, 5879-5887 (2016).
112. Crowe, C.D. & Keating, C.D. Liquid-liquid phase separation in artificial cells. *Interface Focus* **8**, 20180032 (2018).
113. Shuyu, S., Wen, S., Xiaoyi, O. & Ping, W. Phase separation in synthetic biology. *Quant. Biol.* **9**, 378-399 (2021).
114. Tanaka, H. Viscoelastic phase separation in biological cells. *Commun. Phys.* **5**, 167 (2022).
115. Heckel, J., Batti, F., Mathers, R.T. & Walther, A. Spinodal decomposition of chemically fueled polymer solutions. *Soft Matter* **17**, 5401-5409 (2021).
116. Boulon, S., Westman, B.J., Hutten, S., Boisvert, F.M. & Lamond, A.I. The nucleolus under stress. *Mol. Cell* **40**, 216-227 (2010).
117. Hernandez-Verdun, D. Assembly and disassembly of the nucleolus during the cell cycle. *Nucleus* **2**, 189-194 (2011).
118. Pakravan, D., Orlando, G., Bercier, V. & Van Den Bosch, L. Role and therapeutic potential of liquid-liquid phase separation in amyotrophic lateral sclerosis. *J. Mol. Cell Biol.* **13**, 15-28 (2021).
119. Ghosh, B., Bose, R. & Tang, T.Y.D. Can coacervation unify disparate hypotheses in the origin of cellular life? *Curr. Opin. Colloid Interface Sci.* **52**, 101415 (2021).
120. Jia, T.Z. et al. Membraneless polyester microdroplets as primordial compartments at the origins of life. *PNAS* **116**, 15830-15835 (2019).

2 Mechanistic Insights into the Phase Separation Behavior and Pathway-Directed Information Exchange in all-DNA Droplets

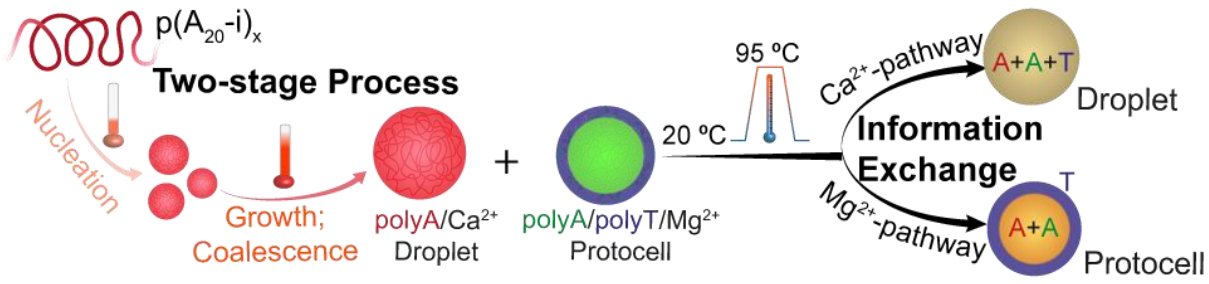

Preliminary note: *This chapter is based on the article published in Angew. Chem. Int. Ed. 61, e202208951 (2022). Minor changes have been made concerning formatting style.*

Abstract: Liquid-liquid phase separation provides a versatile approach to fabricating cell-mimicking coacervates. Recently, it was discovered that phase separation of single-stranded DNA (ssDNA) allows for forming protocells and microgels in multicomponent systems. However, the mechanism of the ssDNA phase separation is not comprehensively understood. Here, we present mechanistic insights into the metal-dependent phase separation of ssDNA and leverage this understanding for a straightforward formation of all-DNA droplets. Two phase separation temperatures are found that correspond to the formation of primary nuclei and a growth process. Ca^{2+} allows for irreversible, whereas Mg^{2+} leads to reversible phase separation. Capitalizing on these differences makes it possible to control the information transfer of one-component DNA droplets and two-component core–shell protocells. This study introduces new kinetic traps of phase separating ssDNA that lead to new phenomena in cell-mimicking systems.

2.1 Introduction

In living cells, liquid-liquid phase separation (LLPS) has been identified as a fundamental phenomenon that drives the assembly of various biomacromolecules into dynamic, often liquid-like colloidal entities.[1-6] The generation of these biological condensates involves for instance demixing of specific proteins with recognition domains and RNAs in a pathway commonly known as complex coacervation.[7, 8] Some of the well-known cellular membrane-less organelles include nucleoli,[9] Cajal bodies[10] and promyelocytic leukemia nuclear bodies in the nucleus,[11] while germ granules and stress granules form in the cytoplasm.[12] As the evidence of numerous subcellular functions and biochemical pathways presenting in these condensates—such as signal transduction, RNA metabolism, DNA damage response, and ribosomal biogenesis—are mounting,[13-15] an interest in employing similar LLPS-driven compartments as an ex vivo protocellular model[16, 17] has been rising in the urge of designing soft materials with life-like traits.

In contrast to oil droplets, coacervates formed via different pathways,[18] such as phase separation of solutes utilizing homolytic interactions or complex coacervation by heterotypic interactions of oppositely charged solutes, contain a large amount of water providing a hydrodynamic molecularly crowded confinement in which enzymes,[19-22] and ribozymes[23] can be active. In recent years, complex coacervates have been recognized as a more suitable protocell model with respect to classical liposomes,[24,

[25] polymersomes,[26] colloidosomes,[27] proteinosomes,[28] due to their molecularly crowded interior resembling the cytoplasmic confinement as well as their ability to ensure facile exchange of matter/energy with their surroundings without employing complex transport machinery. Even though complex coacervates using biologically relevant synthetic constituents, such as short oligonucleotide[3, 22, 29] and peptides,[16, 30] have been reported, achieving control over morphology and dynamic behavior of droplets by varying the biological information encoded in the constituents, such as nucleotide sequence, remains challenging.

Since DNA has emerged as a powerful building block for developing hierarchical nano/microstructures because of its programmability and sequence-specificity, engineering all-DNA coacervates in a bottom-up approach would provide a platform to study chemical reactions and self-assembly processes in a DNA-based crowded environment. There have been reports on designing DNA-rich microgels using multivalent cross-linking of X- and Y-tiles,[31-33] whereas we have recently reported the formation of all-DNA coacervates by simple phase separation of polyadenine (polyA)-rich ssDNA polymers.[21, 34, 35] This approach provides ample parameters (e.g., temperature, ionic strength, DNA chain length) to modulate the morphological and physical properties of the resulting coacervates. We showed that a plethora of all-DNA mesoscopic structures could be realized by combining the phase separation behavior with canonical DNA duplex recognition, leading to capsules or core–shell structures. Although complex structures could be reliable formed by kinetic pathway guidance during temperature ramps, details of the structure formation pathways and a quantitative understanding remain elusive.

In this article, we report a detailed mechanistic understanding of the DNA demixing behavior, and illustrate two different metal ion-dependent phase separation pathways (Ca^{2+} vs. Mg^{2+}). We demonstrate that the phase separation process is in fact a two-stage process and that this heat-induced LLPS is only reversible for Mg^{2+}, but all-DNA coacervate droplets remain stable after cooling for Ca^{2+}. This new Ca^{2+}-specific kinetic trapping can be utilized for simple Ca^{2+}/all-DNA droplet formation, and also opens a new design space to trigger information exchange between coacervates and protocells stemming from distinct ion-specific pathways.

2.2 Results and Discussion

2.2.1 Metal-dependent Phase Separation

Previously, we demonstrated that adenine (A) and thymine (T)-rich ssDNA polymers (namely p(A_{20}-i)$_x$ and p(T_{20}-j)$_y$) exhibit different phase separation behavior in the presence of divalent counterions.[34] The repeating units of the ssDNA consist of a A_{20} block (or T_{20} block) and a 21 nucleobases (nb) long barcode sequence i (or j). The barcode sequences are used to post-functionalize the droplets with dye-appended complementary strands (e.g., dye-conjugated i* or j* for visualization), and have been chosen to avoid self-dimerization and hairpin formation. Additionally, the i/i* and j/j* (T_m≈65 °C) duplexes are stable at room temperature (RT). Our previous focus had been on Mg^{2+}—the most commonly used bivalent counterion for DNA nanoscience—for which we could show that p(A_{20}-i)$_x$ features a length- and Mg^{2+} concentration-dependent lower critical solution temperature (LCST) behavior and undergoes a *reversible* heat-driven solubility-to-insolubility transition. On the contrary, p(T_{20}-j)$_y$ remains in solution at similar Mg^{2+} concentration when heated. We also reported that this sequence-dependent LCST behavior can be leveraged for pathway-dependent core–shell like p(A_{20}-i)$_x$/p(T_{20}-j)$_y$ protocell formation using a simple temperature ramp, during which the polyA-rich demixed phase is kinetically trapped during cooling by hybridization with polyT-rich ssDNA.

In contrast to earlier work on Mg^{2+} ions, we herein focus largely on Ca^{2+} ions for which we identify subtle but important differences, in particular with respect to the reversibility and sequence-specificity of the phase separation processes. In more detail, we present a more straightforward pathway to form independent all-DNA p(A_{20}-i)$_x$ and p(T_{20}-j)$_y$ droplets—stable at RT—using an irreversible heat-triggered phase separation process in the presence of Ca^{2+} ions (Figure 2.1a–c). We also demonstrate that the phase separation of p(A_{20}-i)$_x$/Ca^{2+} passes through two different transition temperatures during the heating, confirming a nucleation and growth mechanism for the formation of p(A_{20}-i)$_x$ droplets (Figure 2.1a). In more detail, we report a detailed mechanistic study to explain the Ca^{2+}-dependent coacervation pathway by varying the ssDNA chain length, Ca^{2+} concentration, and incubation temperature using real-time monitoring of the cloud point behavior and morphological development by in situ confocal laser scanning microscopy (CLSM) and dynamic light scattering (DLS). Whenever needed we also compare to the Mg^{2+}-dependent pathway. Furthermore,

we capitalize on the understanding of the differences between reversible Mg^{2+}-type phase separation and irreversible Ca^{2+} type phase separation to establish coacervate-protocell communication and information exchange by mingling the interactions inherent to the Ca^{2+} and Mg^{2+}-coacervation pathways (Figure 2.1d).

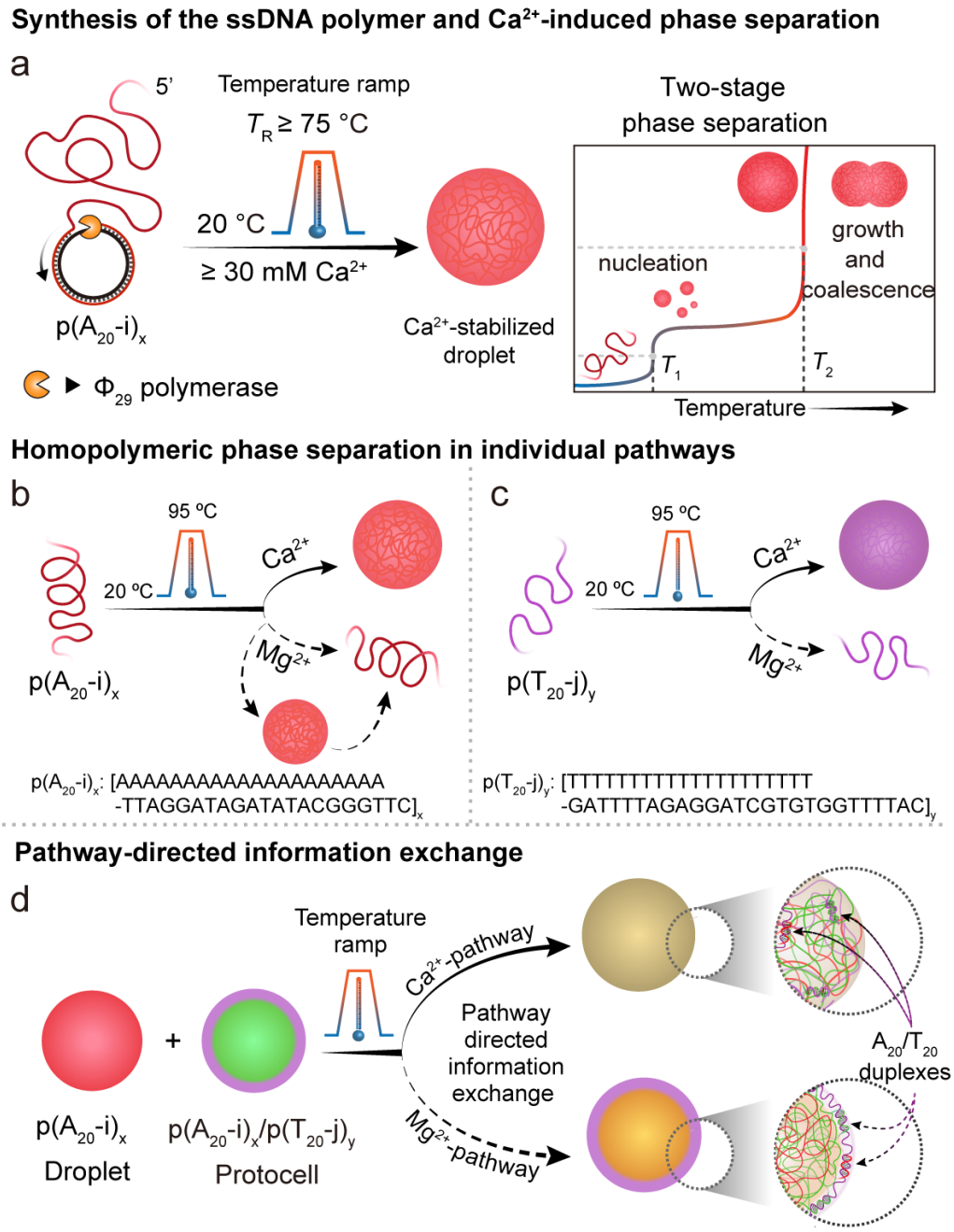

Figure 2.1. Schematic illustration of the synthesis, metal-dependent phase separation, and information exchange of all-DNA droplets. (a) Synthesis of all-DNA multiblock copolymers via rolling circle amplification (RCA), and two stage droplet formation process. **(b)** Phase separation of $p(A_{20}\text{-}i)_x$ with Ca^{2+} and Mg^{2+} ions via a temperature ramp. $p(A_{20}\text{-}i)_x$ undergoes irreversible phase separation with Ca^{2+} and reversible phase separation with Mg^{2+}. **(c)** Phase separation of $p(T_{20}\text{-}j)_y$ occurs only in the presence of Ca^{2+} and not for Mg^{2+}. **(d)** Pathway controlled information exchange by mingling interactions of droplet and protocell mixtures by Ca^{2+}-pathway and Mg^{2+}-pathway.

2.2.2 Effect of ssDNA Chain Length and Ca^{2+} Concentration on Thermo-Responsive Phase Separation

Firstly, to understand the effect of the ssDNA chain length on the phase separation behavior, we synthesized two ssDNA polymers ($p(A_{20}\text{-}i)_x$ and $p(T_{20}\text{-}j)_y$) using an isothermal enzymatic polymerization technique, namely RCA.[36-39] This method yields extremely long sequence-specific multiblock copolymers that are complementary to the sequence encoded in a circular DNA template. Notably, shorter ssDNA multiblock copolymers with varying repeat lengths, x, can be obtained using heat induced cleavage[34] of the RCA product at different incubation times. In total, we prepared six $p(A_{20}\text{-}i)_x$ polymers with x≈12–56 by heating to 95 °C for 5 to 90 min. The average x was calculated from agarose gel electrophoresis (AGE) in Figure 2.2a–c.

Temperature-dependent turbidity measurements at 350 nm (away from the intrinsic DNA absorbance at 260 nm) and DLS allow to analyze the phase separation behavior of $p(A_{20}\text{-}i)_x$ with various chain lengths, and at different Ca^{2+} concentrations (Figure 2.2d,e). We first focus on the effect of chain length. Interestingly, two transition temperatures (T_1 and T_2) are visible while heating the same ssDNA mass concentration of $p(A_{20}\text{-}i)_x/Ca^{2+}$ mixture from 20 °C to 80 °C at 1 °C min^{-1} (Figure 2.2d). Upon increase of the $p(A_{20}\text{-}i)_x$ length from x=12 to 56, T_1 decreases slightly from 40.2 °C to 37.1 °C, and T_2 increases slightly from 75.4 °C to 76.5 °C. The decrease of T_1 with increasing x is in line with general polymer demixing. We suggest—and later provide more evidence—that T_1 and T_2 indicate the nucleation and the growth processes of the phase separation pathway, respectively. The ssDNA polymers $p(A_{20}\text{-}i)_x$ nucleate into small stable nanoscopic seeds above T_1, and as the temperature reaches T_2, the seeds quickly grow and coalesce, leading to the formation of microscopic droplets. Additionally, a plateau in the scattering intensities between T_1 and T_2 appears for $p(A_{20}\text{-}i)_x$ with x > 15. This observation indicates that the $p(A_{20}\text{-}i)_x$ with x≈15 shorter chain length exhibits a more gradual growth, while the longer $p(A_{20}\text{-}i)_x$ experiences a sudden aggregation at T_2. We selected $p(A_{20}\text{-}i)_{27}$ to investigate the effect of the Ca^{2+} concentration on the phase separation (Figure 2.2e). In absence of Ca^{2+}, $p(A_{20}\text{-}i)_{27}$ does not show phase separation. However, two transition temperatures appear consistently for higher Ca^{2+} concentrations. The influence of the Ca^{2+} concentration is much more profound on the details of the phase separation as compared to the influence of chain length. The T_1 decreases strongly from 61.4 °C to

31.1 °C when increasing the Ca^{2+} concentration from 10 mM to 200 mM, whereas T_2 exhibits a slight decrease from 77.5 °C to 75.5 °C. This indicates that varying the Ca^{2+} concentration dramatically alters the primary nucleation temperature (T_1) even though the growth temperature (T_2) is not largely affected.

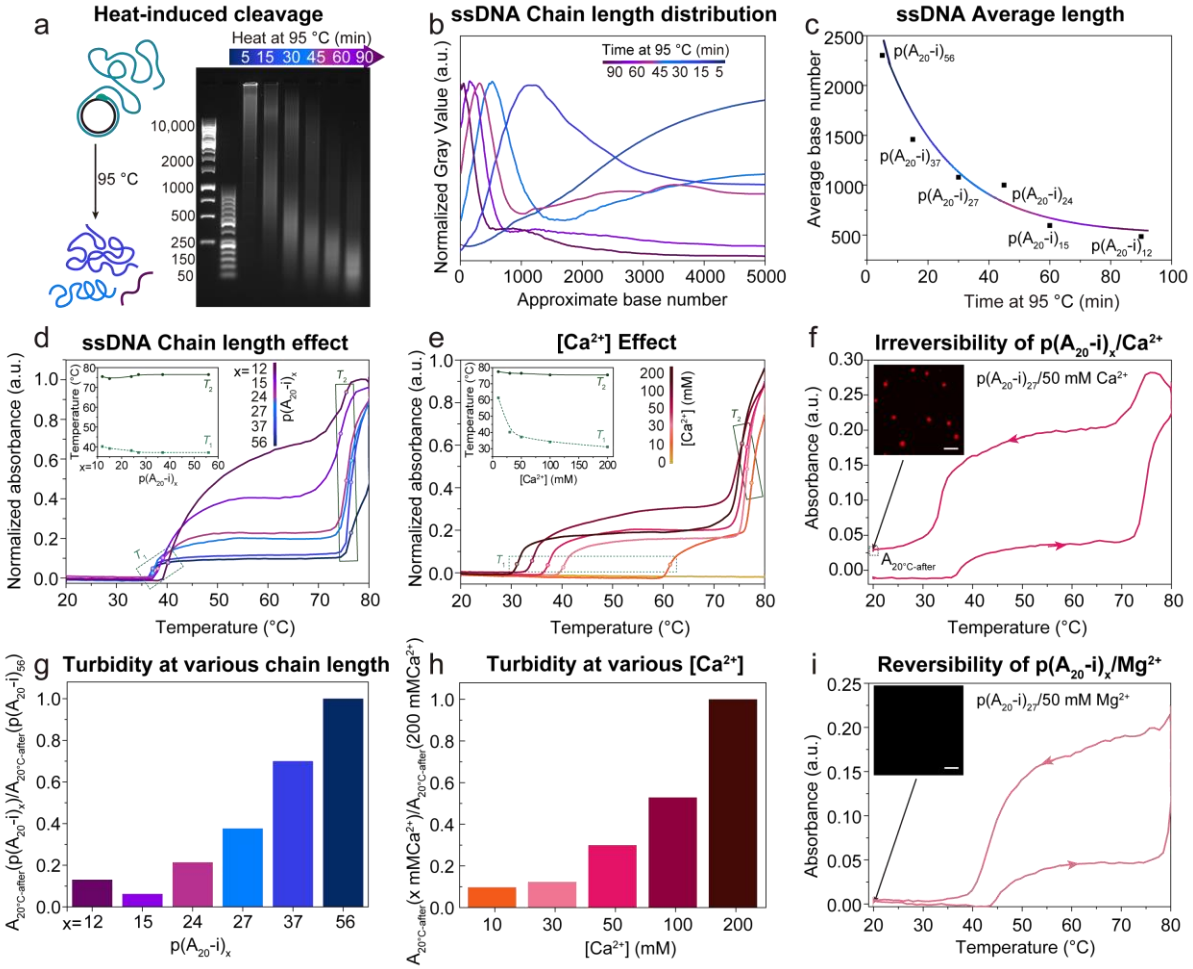

Figure 2.2. Effect of ssDNA chain length and Ca^{2+} concentration on thermo-responsive phase separation. **(a)** Time-dependent AGE for the thermal cleavage of $p(A_{20}\text{-}i)_x$ by heating to 95 °C for different incubation times (5, 15, 30, 45, 60, 90 min). **(b)** Corresponding greyscale analysis of AGE with $p(A_{20}\text{-}i)_x$ length as calculated from the DNA ladders (50 bp and 1k bp). **(c)** Average length of $p(A_{20}\text{-}i)_x$ with incubation time. The actual chain length at short times is longer than this calculated average length because some long DNA strands, especially those longer than 10k (the upper limit of the ladder), cannot be counted. **(d)** Temperature-dependent absorbance at 350 nm of $p(A_{20}\text{-}i)_x$/50 mM Ca^{2+} with different chain lengths. The inset shows T_1 and T_2 with different chain lengths. **(e)** Temperature-dependent absorbance at 350 nm of $p(A_{20}\text{-}i)_{27}/Ca^{2+}$ at varying Ca^{2+} concentrations. The inset shows T_1 and T_2 with different Ca^{2+} concentrations. **(f)** Cyclic temperature ramp showing absorbance at 350 nm of $p(A_{20}\text{-}i)_{27}$/50 mM Ca^{2+}. The inset displays a CLSM image after the heating/cooling cycle. **(g)** Turbidity of $p(A_{20}\text{-}i)_x$/50 mM Ca^{2+} with different chain lengths at 20 °C after heating/cooling cycle. **(h)** Turbidity of $p(A_{20}\text{-}i)_{27}/Ca^{2+}$ with varying Ca^{2+} concentrations at 20 °C after heating/cooling cycle. **(i)** Cyclic temperature ramp showing absorbance at 350 nm of $p(A_{20}\text{-}i)_{27}$/50 mM Mg^{2+}. The inset displays a CLSM image after the heating/cooling cycle. Temperature ramp rate: 1 °C min^{-1}. Scale bar: 10 µm.

Since a detailed understanding of the phase separation behavior is crucial for constructing complex mesoscopic all-DNA droplet morphologies, we paid acute attention to potential differences between the previously established Mg^{2+}-type phase separation[21, 34] and the Ca^{2+}-dependent pathway discovered here. The most critical

and consistent observation is the reversibility of the phase separation in the case of Mg^{2+}, whereas the phase separation is irreversible for Ca^{2+} as highlighted in the heating/cooling cycles in Figure 2.2f,i. The behavior is robust and can be repeated as shown in Figure S2.2a,b. Substantial scattering remains after cooling of $p(A_{20}\text{-}i)_{27}/Ca^{2+}$ (Figure 2.2f), whereas the turbidity completely disappears for $p(A_{20}\text{-}i)_{27}/Mg^{2+}$. Correspondingly, CLSM after cooling does not show any structures for the Mg^{2+}-based system, whereas plenty of DNA droplets with ≈2 µm diameter are observed for the Ca^{2+}-pathway (Figure 2.2f,i; inset). Notably, the decrease in turbidity from high temperature to RT in the $p(A_{20}\text{-}i)_{27}/Ca^{2+}$ system does not need to arise from a partial re-dissolution, but rather stems from a reswelling of the collapsed droplets which goes along with a lower refractive index mismatch between the coacervate and the solution that causes the scattering. The resulting droplets are stable at RT for weeks. The remaining turbidity is a function of the chain length and the Ca^{2+} concentration, which reflects size (see also below, Figure 2.4c,d) and compaction, respectively (Figure 2.2g,h). The Ca^{2+} concentration is expected to lead to different swelling after the heating/cooling cycle, which again rather influences the refractive index contrast and not the particle fraction. Critically, these observations reveal a new Ca^{2+}-induced pathway for forming stable all-DNA droplets without any auxiliary agents to arrest the metastable coacervates kinetically. Previously a surface complexing $p(T_{20}\text{-}j)_y$ or a palindromic, self-crosslinking XL domain in $p(A_{20}\text{-}i\text{-}XL)_x$ was needed in the Mg^{2+}-pathway to stabilize any reversibly forming polyA droplets at high temperature.[34]

2.2.3 Formation of DNA Droplets via the Ca^{2+}-Pathway

To better understand this new Ca^{2+}-pathway for all-DNA droplet formation, we investigated structure formation via CLSM in both ex situ and in situ experimental setups (Figure 2.3a,f,h,j). For the ex situ measurements, we heated and incubated (5 min) a mixture of $p(A_{20}\text{-}i)_{27}$ and 50 mM Ca^{2+} at different top temperatures during a temperature ramp. After the cooling step, a stoichiometric amount of a complementary dye-labeled ssDNA ($Atto_{647}$-i*) was added for CLSM as $Atto_{647}$-i* binds to the barcode i. A series of CLSM micrographs (Figure 2.3b; Figure S2.1a,b) shows that distinct spherical droplets can be observed only when the incubation temperature of the temperature ramp reaches 75 °C. No droplets are formed below 75°C. This ramp temperature is close to the T_2 (76.5 °C) of $p(A_{20}\text{-}i)_{27}$ in the Ca^{2+}-pathway (Figure 2.2e) and indeed confirms that larger scale aggregation by growth and coalescence can

only be observed when heating to or above T_2. The droplet size increases when the incubation temperature is elevated from 75 °C to 95 °C, as derived from statistical image analysis (Figure 2.3d,e). To understand structural processes in the turbidity plateau region between T_1 and T_2, we conducted DLS at RT and at 55°C (Figure 2.3c). An evident change in size occurs from a population of dissolved ssDNA polymers with a $<Dh>_z$ of ca. 20 nm at RT to a $<Dh>_z$ of ca. 200 nm at 55 °C. The DLS count rate also increases from 3.9 to 34.9 $kHzmW^{-1}$ (Figure 2.3c), which aligns with the turbidity increase seen in UV-Vis temperature ramps (Figure 2.2d–f). Obviously, such structures are below the resolution limit of the CLSM. Since the equilibration process in the DLS is slow compared to the temperature ramp used in a thermocycler, a stable collapse and the formation of primary nuclei at this temperature can be concluded. Hence, these observations support the phase separation pathway determined from the UV-Vis spectroscopy, with a primary nucleation step above T_1 and rapid microdroplet formation by growth and coalescence at T_2.

For visual observation of the droplet formation process, we also performed in situ CLSM imaging using a heating stage to monitor the structural transformations during a heating cycle (25→85°C) of a mixture of $p(A_{20}\text{-}i)_{27}$ in the presence of 50 mM Ca^{2+}. For this purpose, we synthesized a covalently labeled $p(A_{20}\text{-}i)_{27}$-Cy5 by co-polymerizing a dUTP-Cy5 monomer (≈2% of dTTP) during the RCA process, which makes the ssDNA polymer intrinsically fluorescent. No distinguishable structures are observed until the temperature reaches ≈85°C. A population of droplets appears after 20 s at 85°C, and successively, the spherical droplets grow in size and eventually undergo coalescence (Figure 2.3g,i). The coalescence of the droplets at 85 °C indicates a dynamic behavior of the phase-separated droplets (Figure 2.3i). We also heated the sample only to the plateau between T_1 and T_2. Similar to the DLS results, CLSM does not show any structures, even using a much slower heating rate and maintaining the temperature for ca. 5 min (Figure 2.3j,k). These in situ CLSM imaging results, together with the DLS data, confirm the presence of a nucleation step with stable nuclei above T_1 and a subsequent growth and coalescence phase above T_2, which is termed as a “two-stage process”.

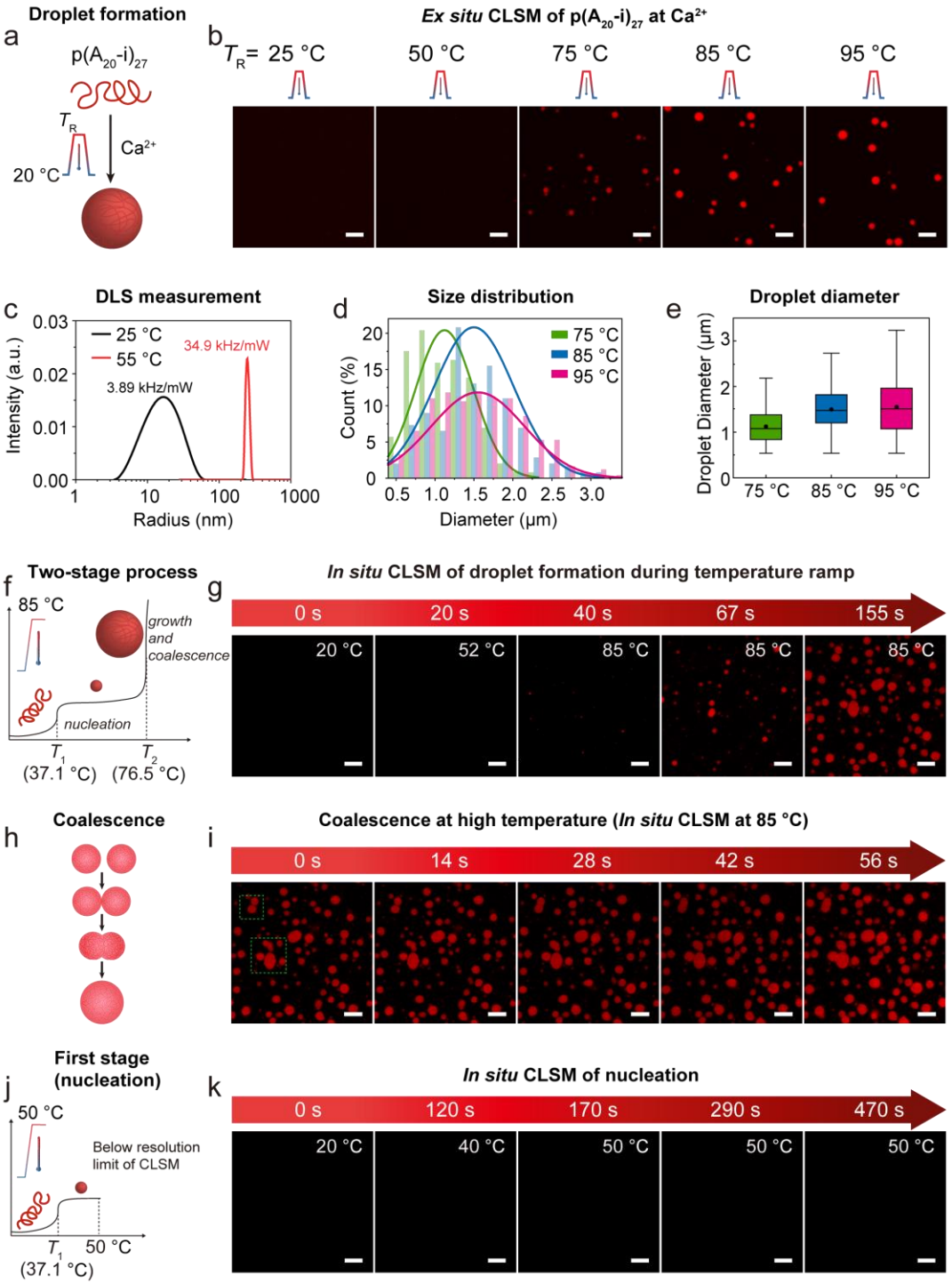

Figure 2.3. Formation of polyA DNA droplets via the Ca^{2+}-pathway. (a) Schematic illustration of the formation of droplets. **(b)** Ex situ CLSM images of 0.08 g L^{-1} solution of $p(A_{20}\text{-}i)_{27}$ with 50 mM Ca^{2+} after incubating at different temperatures for 5 min with a heating and cooling rate of 3 °C s^{-1}. Imaging is done after the completion of the temperature ramp. A minimum temperature of 75 °C is needed for visible droplet formation. **(c)** Diameter profile of 0.003 g L^{-1} solutions of $p(A_{20}\text{-}i)_{27}$ with 50 mM Ca^{2+} measured by DLS at RT and 55 °C. **(d)** Diameter distribution from (b). **(e)** Droplet diameter from (b). The point and line inside the box correspond to the mean and median line of the droplet population. The box represents a five-number summary of the droplet data set, extending from the first quartile to the third quartile. Error bars are the standard deviation of ca. 30 droplet counts. **(f)** Two-stage phase separation of $p(A_{20}\text{-}i)_{27}$ via the Ca^{2+}-pathway. **(g)** In situ CLSM images of 0.12 g L^{-1} solution of $p(A_{20}\text{-}i)_{27}$-Cy5 with 50 mM Ca^{2+} during heating to 85 °C and maintaining at 85 °C with a heating rate of 1.5 °C s^{-1}. **(h)** Schematic illustration of the coalescence of DNA droplets. **(i)** In situ CLSM images of the coalescence of droplets at 85 °C. **(j)** The first stage of phase separation (nucleation) of $p(A_{20}\text{-}i)_{27}/Ca^{2+}$. **(k)** In situ CLSM images of 0.12 g L^{-1} solution of $p(A_{20}\text{-}i)_{27}$-Cy5 with 50 mM Ca^{2+} during heating to 50 °C with a heating rate of 0.15 °C s^{-1}. Scale bar: 5 µm.

For a more comprehensive understanding, we also investigated whether this two-stage process also holds for the phase separation of $p(A_{20}\text{-}i)_{27}$ with 50 mM Mg^{2+}. Indeed, Figure S2.3 also shows the absence of any structures by CLSM in the plateau between T_1 and T_2, thus also confirming a nucleation and growth process. Hence, despite mechanistic similarities between Ca^{2+} and Mg^{2+} in the two-stage process during phase separation, the reversibility of the process is fundamentally different, which relates to the binding interaction of polyA chains with both ions. Previous reports have indicated a higher binding affinity of Ca^{2+} over Mg^{2+} with DNA oligomers in solution,[40-42] and this difference is accentuated at a high concentration of DNA.[41, 43] The higher binding affinity of Ca^{2+} to polyA and polyT chains can be attributed to its more polarizable aqueous shell,[44] enhancing the interaction with the nucleobases apart from the phosphate backbone.[45, 46] Thus, we hypothesize that the higher interaction of the DNA polymers with Ca^{2+} and low chain mobility in the coacervate state causes permanent kinetic trapping of the droplets.

2.2.4 Effect of polyA Chain Length and Ca^{2+} Concentration on Droplet Formation and Properties

Furthermore, we investigated the effect of the ssDNA chain length and the Ca^{2+} concentration on the droplet morphology using CLSM at a constant top temperature in the temperature ramp of 95 °C. Figure 2.4a–e and Figure S2.1c–e show that spherical droplets with moderate dispersity can be formed for $p(A_{20}\text{-}i)_x$ with x between 15 to 37 (50 mM Ca^{2+}). Longer chain lengths, such as $p(A_{20}\text{-}i)_{56}$, lead to aspherical morphologies that arise from coalescence and insufficient mobility of long chains to regain a spherical droplet state.[47] Very short chain lengths ($x < 15$) do not lead to specific structures, which we relate to insufficient kinetic trapping of the phase-separated state (Figure 2.4b). Hence, to synthesize spherical all-DNA droplets via Ca^{2+}-pathway, the optimum number of repeating units in $p(A_{20}\text{-}i)_x$ lies in the range of ≈15–37 (Figure 2.4d) to balance phase separation propensity and chain dynamics that are both a function of the polymer length. As for the influence of Ca^{2+}, we prepared several $p(A_{20}\text{-}i)_{27}$ mixtures with varying Ca^{2+} concentrations from 0 to 200 mM. Figure 2.4f–h and Figure S2.1f,g depict spherical droplets with moderate dispersity for Ca^{2+}≥30 mM, setting the lower limit for efficient kinetic trapping of the high temperature-induced morphology.

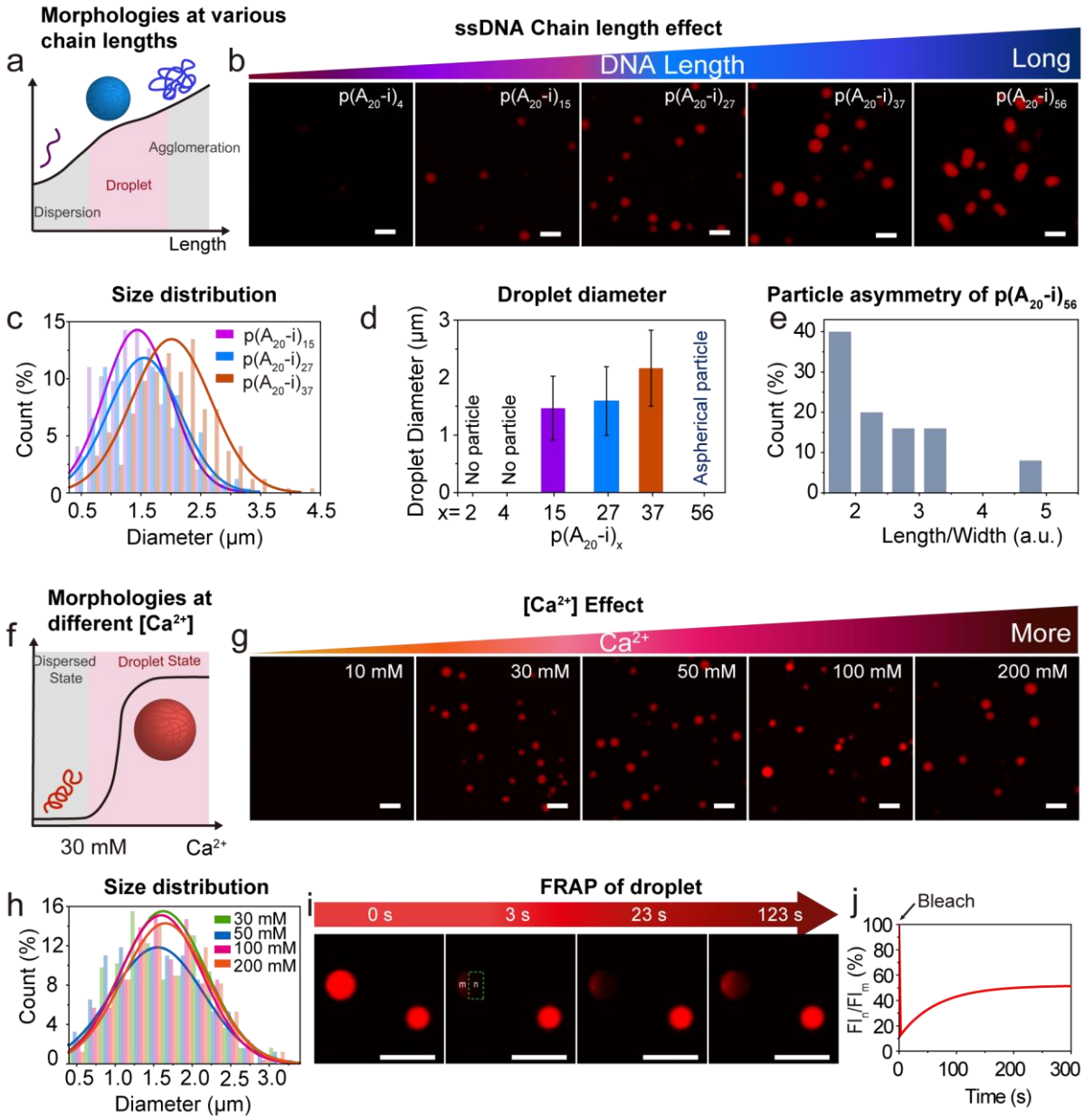

Figure 2.4. Effect of polyA chain length and Ca^{2+} concentration on droplet formation and properties. (a–e) Effect of ssDNA chain length. **(a)** Schematic illustration of $p(A_{20}\text{-i})_x/Ca^{2+}$ morphologies with different chain lengths. **(b)** CLSM images of 0.08 g L^{-1} solution of $p(A_{20}\text{-i})_x$/50 mM Ca^{2+} with an increasing chain length. **(c)** Size distribution of droplet from (b). **(d)** Droplet diameter distribution. Error bars correspond to standard deviations from three duplicate experiments. Ca. 300 droplets were counted. **(e)** Particle asymmetry of $p(A_{20}\text{-i})_{56}/Ca^{2+}$ from (b). **(f–h)** Effect of Ca^{2+} concentration. **(f)** Schematic illustration of $p(A_{20}\text{-i})_{27}/Ca^{2+}$ morphologies at different Ca^{2+} concentrations. **(g)** CLSM images of 0.08 g L^{-1} solution of $p(A_{20}\text{-i})_{27}/Ca^{2+}$ with an increasing Ca^{2+} concentration. **(h)** Size distribution of droplets from (g). **(i–j)** FRAP of $p(A_{20}\text{-i})_{27}$/50 mM Ca^{2+} droplet. **(i)** CLSM images of the droplets during a FRAP experiment: pre-bleach (0 s), bleach (3 s), after-bleaching (23 s and 123 s). **(j)** The corresponding fluorescence intensity from (i) confirms the $p(A_{20}\text{-i})_x/Ca^{2+}$ droplet to have a rather gelled interior. The temperature ramp to 95 °C for 5 min at a heating and cooling rate of 3 °C s^{-1} is used for all the experiments unless otherwise specified. Scale bar: 5 μm.

As mentioned above, the $p(A_{20}\text{-i})_x$ droplets formed via the Mg^{2+}-pathway at elevated temperature dissolve at RT, while the droplets formed via the Ca^{2+}-pathway remain stable at RT. Hence, it is of particular interest to understand the physical state of the droplet interior stabilized at RT formed via the Ca^{2+}-pathway, which is elucidated by

fluorescence recovery after photobleaching (FRAP; Figure 2.4i,j). Approximately 40% of the fluorescence is recovered after 5 min when a part of a droplet is bleached using a 638 nm laser line, indicating a slow diffusion of the polymer chains in the coacervate state, and a rather gelled interior. Our previous work demonstrated that the fluorescence of $p(A_{20}\text{-}i)_x/p(T_{20}\text{-}j)_y$ protocells with liquid polyA cores formed with Mg^{2+} can be fully recovered in a few seconds.[34] This indicates that these Ca^{2+}-based $p(A_{20}\text{-}i)_{27}$ droplets are more solid than the Mg^{2+}-based $p(A_{20}\text{-}i)_{27}/p(T_{20}\text{-}j)_{27}$ protocells, underscoring a difference in binding of Ca^{2+} vs. Mg^{2+} with the polyA chains.

2.2.5 Information Exchange between Coacervate Droplets and Core–Shell Protocells

After having understood mechanistic details on the Ca^{2+}-mediated phase separation of $p(A_{20}\text{-}i)_x$ and its important difference to the Mg^{2+}-mediated phase separation, we raised the question to what extent more complex morphologies can be built up, and whether this new type of kinetic trap can be leveraged for new structure formation pathways. For instance, previously, we could show that a temperature ramp of reversibly phase-separating $p(A_{20}\text{-}i)_x$ in presence of permanently soluble $p(T_{20}\text{-}j)_y$ allows for the formation of core–shell DNA protocells in the presence of Mg^{2+} ions.[34] This process is shown in Figure 2.5c,d. The important prerequisite for this process to work is the solubility of $p(T_{20}\text{-}j)_y$ across the full temperature ramp. However, when $p(T_{20}\text{-}j)_{27}$ is subjected to a temperature ramp at 50 mM Ca^{2+} also $p(T_{20}\text{-}j)_{27}$ coacervates are found (Figure 2.5b). This underscores—similar to $p(A_{20}\text{-}i)_x$—that Ca^{2+} leads to a stronger propensity for phase separation and to a lower nucleobase specificity (Figure 2.5a,b; Figure S2.4a,b). Interestingly, when subjecting a mixture of $p(A_{20}\text{-}i)_{27}$ and $p(T_{20}\text{-}j)_{27}$ to a temperature ramp in the presence of 50 mM Ca^{2+}, an Mg^{2+}-induced protocell architecture cannot be found; instead, mixed coacervates containing both ssDNA equally distributed within the droplet are found (Figure 2.5c). In addition to phase separation by Ca^{2+}, the mixed DNA domains are now additionally stabilized via A_{20}-T_{20} duplex formation during cooling.

On a system level, we hypothesized that such salt-dependent morphologies could be used to create new coacervate structures by mixing multiple coacervate systems and exposing them to a second temperature ramp. To this end, we mixed Ca^{2+}-based $p(A_{20}\text{-}i)_{27}$ droplets (red in Figure 2.5f) with Mg^{2+}-based $p(A_{20}\text{-}i)_{27}/p(T_{20}\text{-}j)_{27}$ protocells (green and magenta, core and shell, Figure 2.5f) and investigated to what extent they

can merge their “genetic content” embedded in the ssDNA sequence (Figure 2.5d,e). Prior to this, we first exchanged the buffer for 10 mM NaCl TE buffer, which led to a swelling of both entities, but complete dissolution was prevented in the protocells due to A_{20}-T_{20} duplexes at the interface and in the Ca^{2+}-based p(A_{20}-i)$_{27}$ droplets due to some remaining Ca^{2+} (Figure 2.5g). After that, we again added new metal ions, Ca^{2+} or Mg^{2+}, to a total concentration of 50 mM.

When the resulting droplet/protocell mixture is subjected to a second temperature ramp, two different morphologies emerge via two different metal ion-dependent pathways (Figure 2.5e,f,h,k; Figure S2.5a–c). In the Ca^{2+}-pathway, the droplets and protocells (both core and shell) undergo mixing with the formation of partly phase-separated Janus-type structures as well as mixed droplets (Figure 2.5h–j; Figure S2.5d). The initial protocells disappear and transform into homogeneously mixed coacervates due to the insolubility of the p(T_{20}-j)$_{27}$ in the presence of Ca^{2+} at elevated temperature. The line segment analysis on the final mixed droplets shows near homogeneous droplets (Figure 2.5i), and the observed Janus-like structures further confirm the coalescence behavior during the formation of the final mixed droplets (Figure 2.5j).

On the other hand, in the Mg^{2+}-dependent pathway, a core–shell protocell with mixed core emerges (Figure 2.5e,k). The p(A_{20}-i)$_{27}$ chains from both the droplet and the protocell integrate to form mixed protocell core. This is clearly seen in the superposition of the red fluorescence originating from the covalently labeled p(A_{20}-i)$_{27}$-Cy5 from the original Ca^{2+}-mediated droplet and of the green fluorescence emerging from the post-staining of p(A_{20}-i)$_{27}$, present in the Mg^{2+}-mediated protocell, with Atto$_{565}$-i*. Additionally, a clear shell of p(T_{20}-j)$_{27}$ post-stained with a magenta Atto$_{488}$-j* conjugate is visible. This homogeneous mixing in the core of both p(A_{20}-i)$_{27}$-based ssDNA from the droplet and the protocell, and the shell localization of p(T_{20}-j)$_{27}$ is enabled by the absence of phase separation of p(T_{20}-j)$_{27}$ in the presence of Mg^{2+} ions (Figure 2.5k,l; Figure S2.5e). The formation of various morphologies via performing a temperature ramp on the droplet and protocell mixture achieves pathway-controlled structuration by metal-dependent phase separation of ssDNA polymers, thus offering the possibility of information exchange of DNA biomaterials.

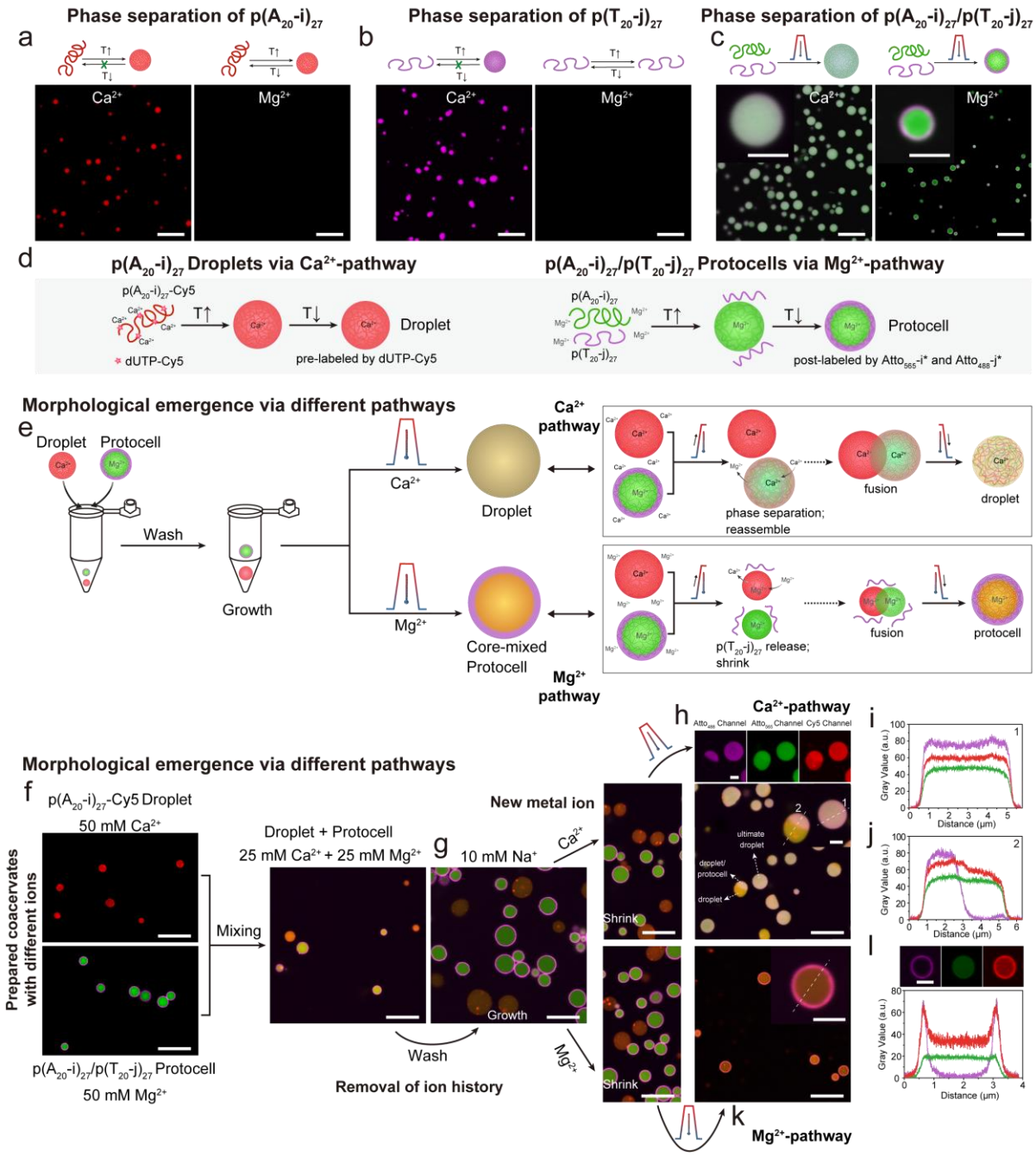

Figure 2.5. Information exchange between coacervate droplets and core–shell protocells in the presence of Ca^{2+} and Mg^{2+} ions. (a) Reversibility of metal-dependent phase separation of p(A_{20}-i)$_{27}$. **(b)** Reversibility of metal-dependent phase separation of p(T_{20}-j)$_{27}$. **(c)** Complex morphologies can be obtained by subjecting a mixture of p(A_{20}-i)$_{27}$ and p(T_{20}-j)$_{27}$ to a temperature ramp at Ca^{2+} or Mg^{2+} ions. **(d)** Synthesis of droplets via Ca^{2+}-pathway and protocells via Mg^{2+}-pathway. **(e–l)** Information exchange of coacervate droplets and core–shell protocells via different phase separation pathways. **(e)** Strategy and mechanisms of information exchange. **(f)** CLSM images of droplets and protocells. **(g)** Structures swell after washing with 10 mM NaCl TE buffer. **(h)** CLSM images of resulting mixed droplets via Ca^{2+}-pathway. **(i–j)** Line segment analysis of the resulting droplets and Janus-like structure. **(k)** CLSM images of the resulting core–shell protocells with mixed core via Mg^{2+}-pathway. **(l)** Line segment analysis of the obtained protocell. Scale bar: 5 μm. inset: 2 μm.

2.3 Conclusion

We have systematically investigated the coacervations of ssDNA polymers based on the thermo-responsive phase separation pathways that are important for a

fundamental understanding of the phase behavior of nucleic acids in biology and nanoscience, as well as for the formation of DNA droplets and DNA-based protocells as entities to study life-like behavior in complex systems. Significantly, by using a combination of ex situ and in situ CLSM and DLS, we have identified similarities and distinct differences in the ion-dependent phase separation behavior between Mg^{2+}- and Ca^{2+}-pathways, both of which follow a two-stage process for coacervation of the ssDNA chains. A first critical temperature is found, T_1, whereupon stable nuclei are formed that are much smaller than the optical diffraction limit, followed by a relatively stable temperature region (in terms of turbidity), and eventually, a second transition, T_2, occurs that leads to micron-scale coacervation by growth and coalescence. The T_1 and T_2 regions depend slightly on the overall chain length but more strongly on the counterion concentration. This behavior is robust. The most striking difference between Ca^{2+} and Mg^{2+} as counterions relates to the reversibility of the phase transition. Mg^{2+} has a fully reversible transition, whereas Ca^{2+} clearly leads to irreversible trapping of the coacervate droplets formed at high temperatures. The stronger propensity of Ca^{2+} for coacervate formation also leads to a different selectivity regarding the nucleobases. While Mg^{2+} leads to selective temperature-induced coacervation of polyA-rich ssDNA, whereas polyT-rich ssDNA remains in solution, Ca^{2+} is clearly indiscriminatory and also leads to temperature-induced coacervation of polyT-rich strands. Additionally, we could derive important aspects regarding sphericity and size of the coacervates by showing that an appropriate length is needed to obtain sufficient phase separation, while excessively long strands hinder re-obtaining a spherical shape after droplet coalescence at high temperature.

In summary, these data show that a careful mapping of the system behavior allows delineating distinct differences regarding ion-dependent and temperature-induced phase separation of ssDNA polymers. We put the different strengths of the approaches to work and could show that a Ca^{2+}-derived polyA-rich droplet (that would be unstable in a Mg^{2+} setting) can merge their information content with a Mg^{2+}-derived core/shell DNA protocell formed by a polyA/polyT (that would equally not form in a Ca^{2+}-setting) by proper salinity adjustment and using a secondary temperature ramp.

These phase behavior of sequence-specific nucleic acid polymers may provide an essential understanding of relevant scenarios in living cells, such as heat shock-mediated droplet formation inside the living cell cytoplasm[48, 49] or the relevance of a

polyA-tag present in each mRNA produced in the nucleus. Furthermore, our studies also may pave the way toward understanding the “origin of life” scenarios where nucleic acids played an essential role in prebiotic confinements.[21, 50]

Together, these investigations of the phase separation mechanisms offer a better understanding of coacervation of DNA-based systems, properties of membrane-less nucleic acid-rich organelles, and emulating life-like functions in future protocellular systems.

2.4 Supplementary Information

2.4.1 Materials

All DNA oligonucleotides and nuclease-free water were purchased from Integrated DNA Technologies (IDT). NxGen T4 DNA ligase (2 U/µL and 20 U/µL), Exonuclease I (20 U/µL), Exonuclease III (200 U/µL), and Φ29 DNA polymerase (10 U/µL) were supplied by Lucigen. Inorganic pyrophosphatase (0.1 U/µL) was supplied from New England Biolabs (NEB). dNTP Bundle (dATP, dCTP, dGTP, dTTP; 4 × 100mM), Aminoallyl-dUTP-Cy5, and Aminoallyl-dUTP-XX-ATTO-488 were supplied by Jena Bioscience GmbH. Calcium acetate, Magnesium acetate, Sodium chloride (NaCl, 99%), acetic acid, Tris(hydroxymethyl)-aminomethane hydrochloride (Tris-HCl, pH=8), Ethylenediaminetetraacetic acid disodium salt dihydrate (EDTA), and Trizma base were purchased from Sigma-Aldrich Chemie GmbH. Agarose low EEO (Agarose Standard) was ordered from AppliChem GmbH. SYBR™ Gold Nucleic Acid Gel Stain, DNA gel loading dye (6x), GeneRuler 50 bp DNA Ladder, and GeneRuler 1 kb DNA Ladder were purchased from Thermo Fisher Scientific. Milli-Q water was used throughout this study.

10x T4 DNA ligase buffer (pH=7.6): 500 mM Tris-HCl, 100 mM $MgCl_2$, 50 mM dithiothreitol and 10 mM ATP.

10x Φ29 DNA polymerase buffer (pH=7.5): 500 mM Tris-HCl, 100 mM $(NH_4)_2SO_4$, 40 mM dithiothreitol and 100 mM $MgCl_2$.

TE Buffer (pH=8): 10 mM Tris-HCl and 1 mM EDTA.

TAE Buffer (pH=8): 40 mM Tris, 20 mM acetic acid and 1 mM EDTA.

2.4.2 General Characterization Methods and Instruments

UV-Vis measurements were performed on an Analytic Jena Scandrop connecting with JUMO DTRON 308 temperature controller.

Agarose gel electrophoresis (AGE) was conducted using 1 wt% agarose gel in TAE buffer and 90 V for 2 h with SYBR gold pre-staining.

Dynamic light scattering (DLS) measurements were conducted on the LS Instruments Naonolab 3D.

Confocal laser scanning microscopy (CLSM) was performed on Leica Stellaris 5 microscope. “In situ CLSM” was performed by connecting a Micro heating stage VAHEAT temperature controller to the Leica microscopy.

2.4.3 Oligonucleotide Sequences

Table S2.1. Oligonucleotide sequences used, with their names, the sequence codes, the purification methods, and the modifications.

	Name	Oligonucleotide sequence (5’-3’)	Purification	Modification
$p(A_{20}\text{-}i)_x$	Template ($Tp(A_{20}\text{-}i)_x$)	/5Phos/ATCTATCCTAATTTTTTTTTTTTTTTTTTTTGAACCCGTAT	HPLC	5’-Phosphorylation
	Primer (i’)	TTAGGATAGATATACGGGT*T*C	Desalting	Phosphorothioated Twice
	Ligation (i)	TTAGGATAGATATACGGGTTC	HPLC	None
	Barcode strand ($Atto_{647}$-i*)	/5ATTO647NN/TGAACCCGTATATCTATCCTAA	HPLC	5’ Atto 647N (NHS ester)
	Barcode strand ($Atto_{565}$-i*)	/5ATTO565N/TGAACCCGTATATCTATCCTAA	HPLC	5’ Atto 565 (NHS ester)
$p(T_{20}\text{-}j)_y$	Template ($T_p(T_{20}\text{-}j)_y$)	/5Phos/ATCCTCTAAAATCAAAAAAAAAAAAAAAAAAAAGTAAAACCACACG	HPLC	5’-Phosphorylation
	Primer (j’)	TTTTAGAGGATCGTGTGGTT*T*T	Desalting	Phosphorothioated Twice
	Ligation (j)	TTTTAGAGGATCGTGTGGTTTT	HPLC	None
	Barcode strand ($Atto_{488}$-j*)	/5ATTO488N/AAAACCACACGATCCTCTAAAA	HPLC	5’ Atto 488 (NHS ester)

2.4.4 Experimental Protocols

2.4.4.1 Synthesis of Circular ssDNA Templates and ssDNA Polymer by Rolling Circle Amplification (RCA)

1 μM linear ssDNA template, 1 μM ligation strand, and 100 mM NaCl were mixed in TE buffer to the final volume of 100 μL. The solution was rapidly heated to 85 °C (for 5 min) at a rate of 3 °C/s and then slowly cooled to 20 °C at a rate of 0.01 °C/s. The annealed solution, 1x T4 DNA ligase buffer, as well as 0.1 U/μL T4 DNA ligase, were added to nucleasefree water to the final volume of 200 μL. The mixture was gently shaken for 3 h at room temperature (RT) and then heated to 70 °C for 20 min at a rate of 3 °C/s to inactivate the T4 DNA ligase. Afterwards, 1 U/μL Exonuclease I and 5 U/μL Exonuclease III were added to the solution and incubated overnight at 37 °C to remove unhybridized ligation strands and non-circularized templates. The mixture was then heated to 80 °C (for 40 min) to inactivate the exonucleases. The circular templates

were purified using 10 kDa Amicon Ultra Centrifugal Filters and washed three times with TE buffer. The obtained circular template concentrations were measured via UV-Vis.

0.05 µM circular template, 0.1 µM primer, 1x Φ29 polymerase buffer, 0.2 U/µL Φ29 polymerase, 0.01 U/µL inorganic pyrophosphatase, 5 mM adjusted dNTP mixture composed of dATP, dTTP, dCTP, and dGTP in a ratio of the corresponding expected ssDNA polymer, and nuclease-free water were mixed to final volume of 200 µL for polymerization reaction. The reaction was conducted at 30 °C for 60 h. The obtained polymers were purified using 30 kDa Amicon Ultra Centrifugal Filters and washed three times with TE buffer. When needed, the polymers were subjected to heat-induced cleavage by heating to 95 °C for an incubation time ranging from 5 to 90 min to get ssDNA with different chain lengths. The ssDNA concentrations were measured via UV-Vis. All samples were further analyzed by AGE.

The covalently labeled ssDNA polymers $p(A_{20}\text{-}i)_x$-Cy5 and $p(T_{20}\text{-}j)_y$-$Atto_{488}$ were synthesized as described above except that dUTP-Cy5 or Aminoallyl-dUTP-XX-ATTO-488 was introduced in the dNTP mixture at a ratio of 2% of dTTP.

2.4.4.2 Phase Separation Behavior of $p(A_{20}\text{-}i)_X$ and its Reversibility

To evaluate the effects of the ssDNA chain length and the Ca^{2+} concentration on the phase separation behavior of $p(A_{20}\text{-}i)_x$, heat-induced cleavage was used to obtain $p(A_{20}\text{-}i)_x$ with different chain lengths and different Ca^{2+} concentrations from 0 to 200 mM were introduced. The samples were prepared by dissolving 0.04 g/L $p(A_{20}\text{-}i)_x$ in TE buffer containing different Ca^{2+} concentrations. Temperature-dependent UV-Vis spectra were recorded by measuring the absorbance at 350 nm every minute. The samples were heated from 20 °C to 80 °C, kept at 80 °C for 30 min, and subsequently cooled to 20 °C (1 °C/min). To evaluate the reversibility of phase separation of $p(A_{20}\text{-}i)_x$, the samples after cooling were observed by CLSM.

2.4.4.3 Formation of $p(A_{20}\text{-}i)_x$ Droplets

A final concentration of 0.08 g/L $p(A_{20}\text{-}i)_x$ was prepared in TE buffer containing different Ca^{2+} concentrations (i.e. 10 mM, 30 mM, 50 mM, 100 mM, 200 mM). The solution was heated to 95 °C for 5 min at a heating and cooling rate of 3 °C/s. All the samples were observed by CLSM after addition of $Atto_{647}$-i*. For further investigation of the temperature-dependent formation of $p(A_{20}\text{-}i)_x/Ca^{2+}$ morphology, the samples

consisting of p(A_{20}-i)$_{27}$, 50 mM Ca^{2+} and TE buffer were heated to different top temperatures (i.e. 25 °C, 50 °C, 70 °C, 75 °C, 80 °C, 85 °C, 90 °C, 95 °C) for 5 min and then observed at RT by CLSM.

For a better understanding of the droplet formation, we also used real-time in situ CLSM to observe the droplet formation process during temperature rise. The samples consisting of p(A_{20}-i)$_{27}$-Cy5, 50 mM Ca^{2+}, and TE buffer were heated to 85 °C (higher than T_2) or 50 °C (the plateau between T_1 and T_2) for 5 min, and the images were recorded.

2.4.4.4 Fluorescence Recovery after Photobleaching (FRAP) of ssDNA Droplets

The p(A_{20}-i)$_x$/50 mM Ca^{2+} droplets with Atto$_{647}$-i* formed as above procedure were first imaged under appropriate 638 nm laser intensity. Photobleaching (3 s) was performed using 100% intensity on the 638 nm line. Images before and after photobleaching were recorded.

2.4.4.5 Phase Separation Behavior Comparison of ssDNA in the Presence of Various Metal Ions

To compare the phase separation behavior of p(A_{20}-i)$_{27}$ and p(T_{20}-j)$_{27}$ at Ca^{2+} and Mg^{2+} ions, the temperature ramp (95 °C for 5 min, 3 °C/s ramp rate) was performed on samples of 0.08 g/L p(A_{20}-i)$_{27}$ at 50 mM Ca^{2+} (or Mg^{2+}) and 0.08 g/L p(T_{20}-j)$_{27}$ at 50 mM Ca^{2+} (or Mg^{2+}), respectively. Atto$_{647}$-i* and Atto$_{488}$-j* were added for the visualization by CLSM after particle formation.

2.4.4.6 Information Exchange of Droplets via Various Ions Pathways

Firstly, the p(A_{20}-i)$_{27}$-Cy5/50 mM Ca^{2+} droplets and the p(A_{20}-i)$_{27}$/p(T_{20}-j)$_{27}$/50 mM Mg^{2+} protocells were prepared by heating the corresponding mixture to 95 °C for 5 min at a heating and cooling rate of 3 °C/s. Then the mixture of droplets and protocells was washed by TE buffer containing 10 mM Na+ to remove excess Ca^{2+} and Mg^{2+} in the solution. Then the sample was split and the concentration of Ca^{2+} or Mg^{2+} was adjusted to 50 mM, respectively. Subsequently both samples were subjected to the same temperature ramp (95 °C for 5 min, 3 °C/s ramp rate). Atto$_{565}$-i* and Atto$_{488}$-j* were added to visualize the prepared p(A_{20}-i)$_{27}$/p(T_{20}-j)$_{27}$/50 mM Mg^{2+} protocells and all the final products.

Real-time in situ CLSM was used to further confirm the morphologies and the formation of mixed droplets by subjecting droplet/protocell mixture to a second

temperature in the presence of Ca^{2+} ions. $p(A_{20}\text{-}i)_{27}$-Cy5 was used to form intrinsically fluorescent $p(A_{20}\text{-}i)_{27}$-Cy5 droplets, and $p(A_{20}\text{-}i)_{27}$ and $p(T_{20}\text{-}j)_{27}$-$Atto_{488}$ were used to form the $p(A_{20}\text{-}i)_{27}/p(T_{20}\text{-}j)_{27}$-$Atto_{488}$ protocells wherein only shells were labeled covalently with $Atto_{488}$. Then the mixture of droplet and protocell was washed with 10 mM Na^+ TE buffer to remove excess Ca^{2+} and Mg^{2+} in the solution. Lastly, 50 mM of Ca^{2+} was added to the solution and the solution was heated up to 95 °C for 5 min at a heating and cooling rate of 3 °C/s. Images were recorded during this process using CLSM with a heating stage.

2.4.5 Supplementary Figures

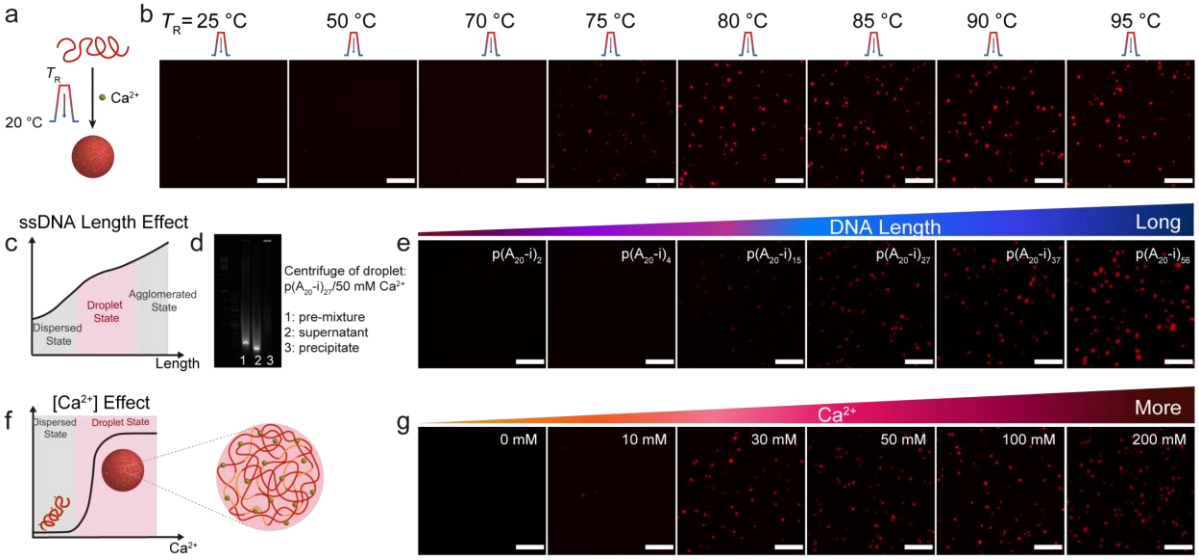

Figure S2.1. Effects of incubation temperature, ssDNA chain length, and Ca^{2+} concentration on droplet formation. (a–b) CLSM images of 0.08 g/L solution of $p(A_{20}\text{-}i)_{27}$ with 50 mM Ca^{2+} by incubated at different top temperatures for 5 min. A minimum temperature of 75 °C is needed for droplet formation. **(c)** Schematic illustration of $p(A_{20}\text{-}i)_x/Ca^{2+}$ morphology at increasing chain length of $p(A_{20}\text{-}i)_x$. **(d)** AGE of the pre-solution of $p(A_{20}\text{-}i)_{27}$ at 50 mM Ca^{2+}, and the supernatant and precipitate of $p(A_{20}\text{-}i)_{27}$/50 mM Ca^{2+} droplet after centrifugation. The formed droplets are blocked in the pocket. Some longer DNA can be detected in the pre-solution, but not in the supernatant. **(e)** CLSM images of 0.08 g/L solution of $p(A_{20}\text{-}i)_x$/50 mM Ca^{2+} at increasing chain length of $p(A_{20}\text{-}i)_x$. **(f)** Morphologies of $p(A_{20}\text{-}i)_{27}$ at various Ca^{2+} concentrations. **(g)** CLSM images of 0.08 g/L solution of $p(A_{20}\text{-}i)_{27}/Ca^{2+}$ at different Ca^{2+} concentrations. Scale bar: 20 µm.

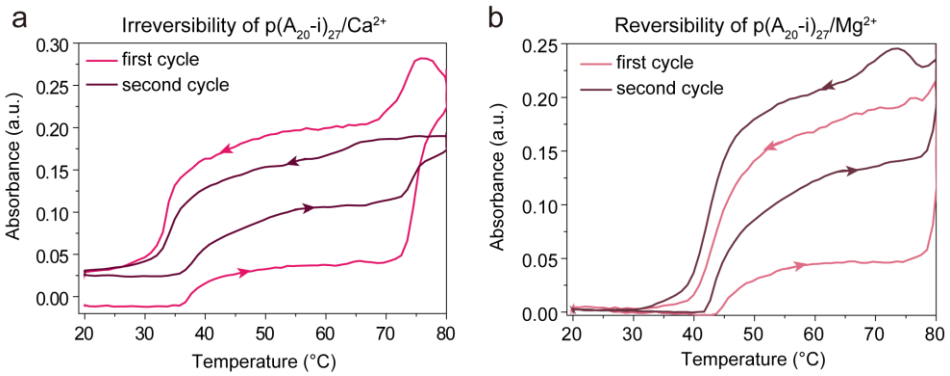

Figure S2.2. Reversibility of ssDNA phase separation at Ca^{2+} and Mg^{2+}. (a) Cyclic temperature ramp showing absorbance at 350 nm of $p(A_{20}\text{-}i)_{27}$/50 mM Ca^{2+}. **(b)** Cyclic temperature ramp showing absorbance at 350 nm of $p(A_{20}\text{-}i)_{27}$/50 mM Mg^{2+}.

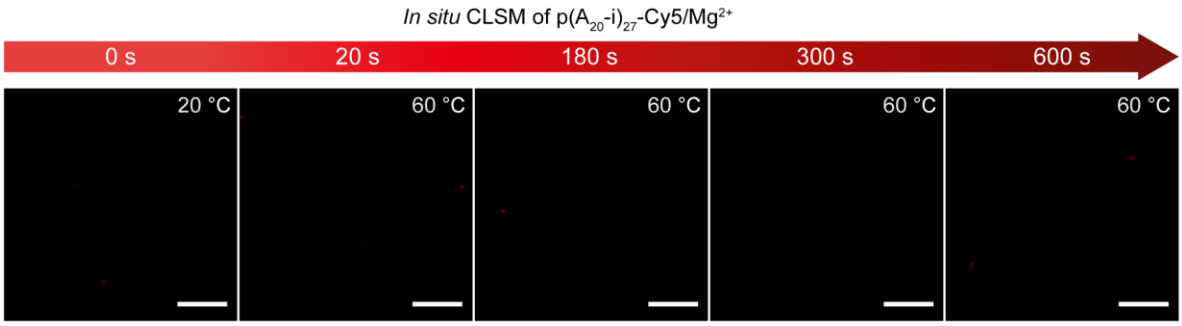

Figure S2.3. Phase separation of $p(A_{20}\text{-}i)_{27}/Mg^{2+}$ after heating to 60 °C. In situ CLSM images of 0.2 g/L solution of $p(A_{20}\text{-}i)_{27}$-Cy5 with 50 mM Mg^{2+} by heating to 60 °C with a heating rate of 3 °C/s. No structures are found. Scale bar: 5 µm.

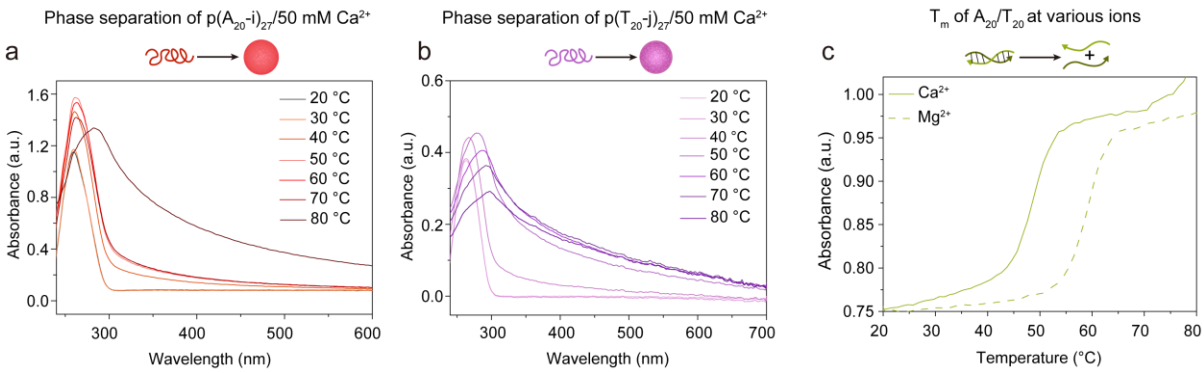

Figure S2.4. Phase separation of ssDNA at Ca^{2+} and Mg^{2+}. (a) UV-Vis spectra of 0.04 g/L solution $p(A_{20}\text{-}i)_{27}$ at 50 mM Ca^{2+} with a temperature ramp rate of 1 °C/min. **(b)** UV-Vis spectra of 0.04 g/L solution $p(T_{20}\text{-}j)_{27}$ at 50 mM Ca^{2+} with a temperature ramp rate of 1 °C/min. **(c)** Melting temperature (T_m) measurement of A_{20}/T_{20} at 50 mM Ca^{2+} or 50 mM Mg^{2+}, showing that $T_{m\ (Ca2+)}$ is slightly lower than $T_{m\ (Mg2+)}$.

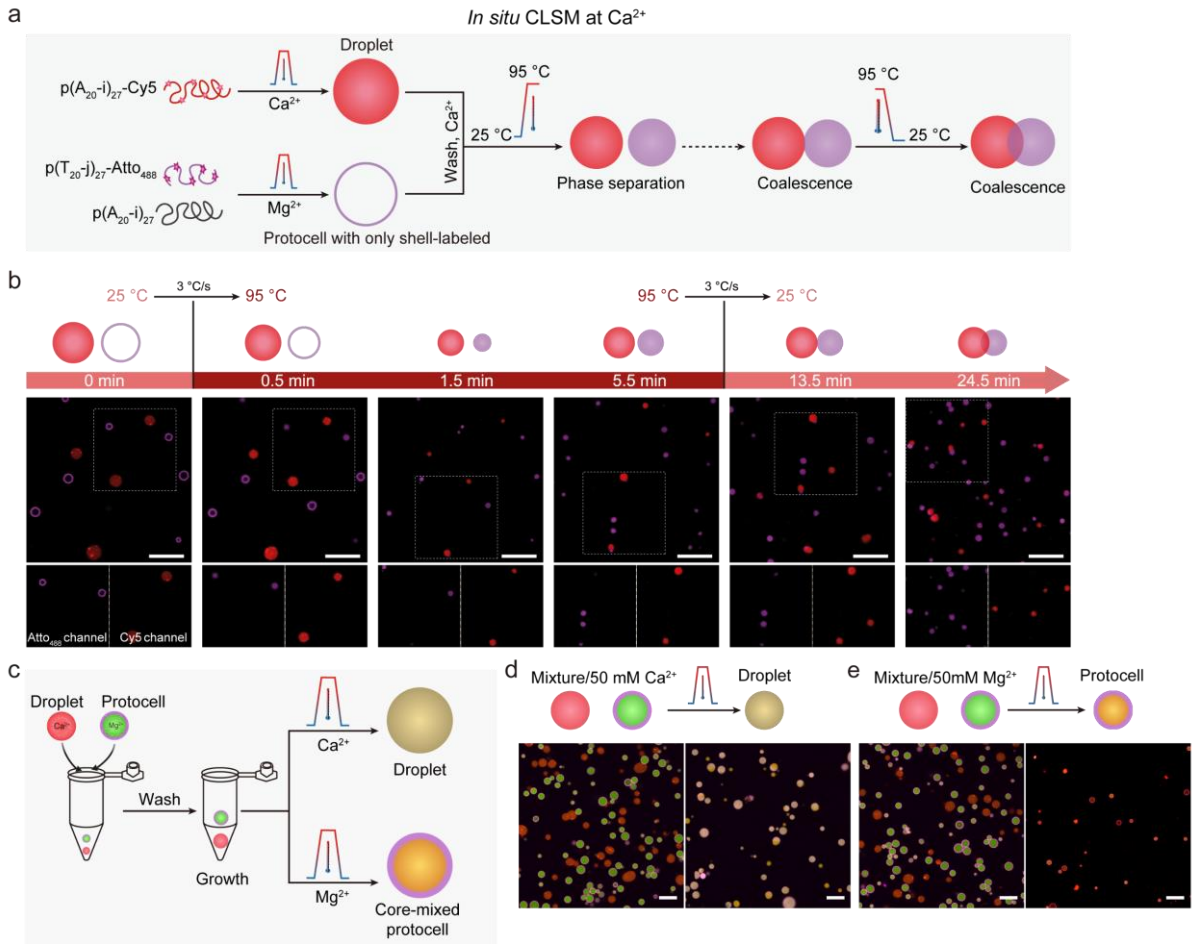

Figure S2.5. Further evidence for information exchange by coalescence. (a) Illustration of in situ CLSM of the mixture of p(A_{20}-i)$_{27}$-Cy5 droplet and p(A_{20}-i)$_{27}$/p(T_{20}-j)$_{27}$-Atto$_{488}$ protocell during temperature ramp in the presence of Ca^{2+} ions. Cy5 and Atto$_{488}$ were introduced during the synthesis of p(A_{20}-i)$_{27}$-Cy5 (red) and p(T_{20}-j)$_{27}$-Atto$_{488}$ (magenta) by RCA. p(A_{20}-i)$_{27}$ refers to the ssDNA without dye. Metastable Janus-like droplets started forming after heating the mixture to 95 °C, suggesting sufficient dynamics for coalescence of the droplets at high temperatures. **(b)** In situ CLSM images of droplet and protocell mixture in the presence of Ca^{2+} ions. **(c)** Strategy of information exchange of droplets via different ion pathways of ssDNA phase separation. **(d)** CLSM images of the mixture of droplet and protocell after the addition of new Ca^{2+} ions and the resulting droplets via Ca^{2+}-pathway. **(e)** CLSM images of the mixture of droplet and protocell after the addition of new Mg^{2+} ions and the resulting core-mixed protocell via Mg^{2+}-pathway. Scale bar: 10 µm.

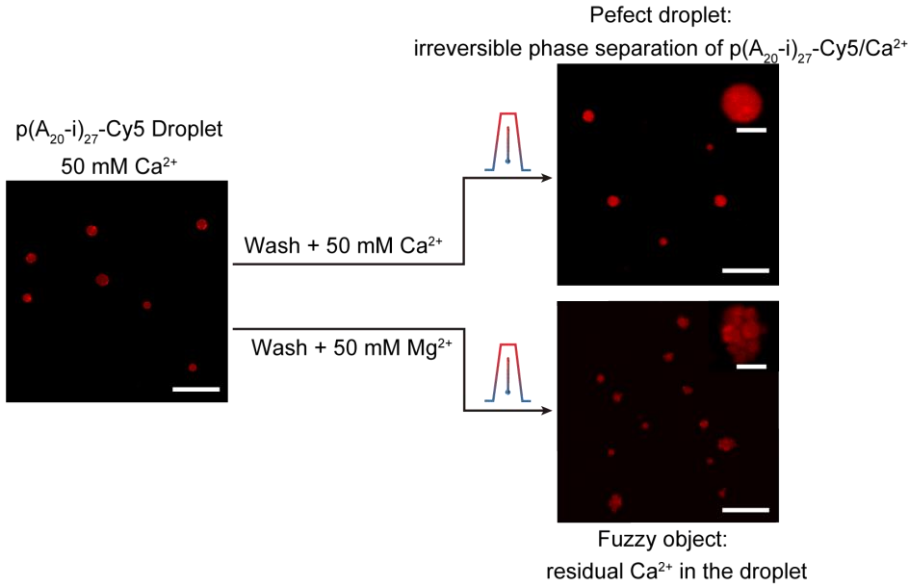

Figure S2.6. Morphological investigations of $p(A_{20}\text{-}i)_{27}/Ca^{2+}$ droplets at Ca^{2+} or Mg^{2+} ions. Morphological investigations of $p(A_{20}\text{-}i)_{27}$-Cy5 droplets prepared via Ca^{2+}-pathway, and subsequently subjected to a temperature ramp in the presence of Ca^{2+} or Mg^{2+} ions. Scale bar: 10 µm. inset: 2 µm.

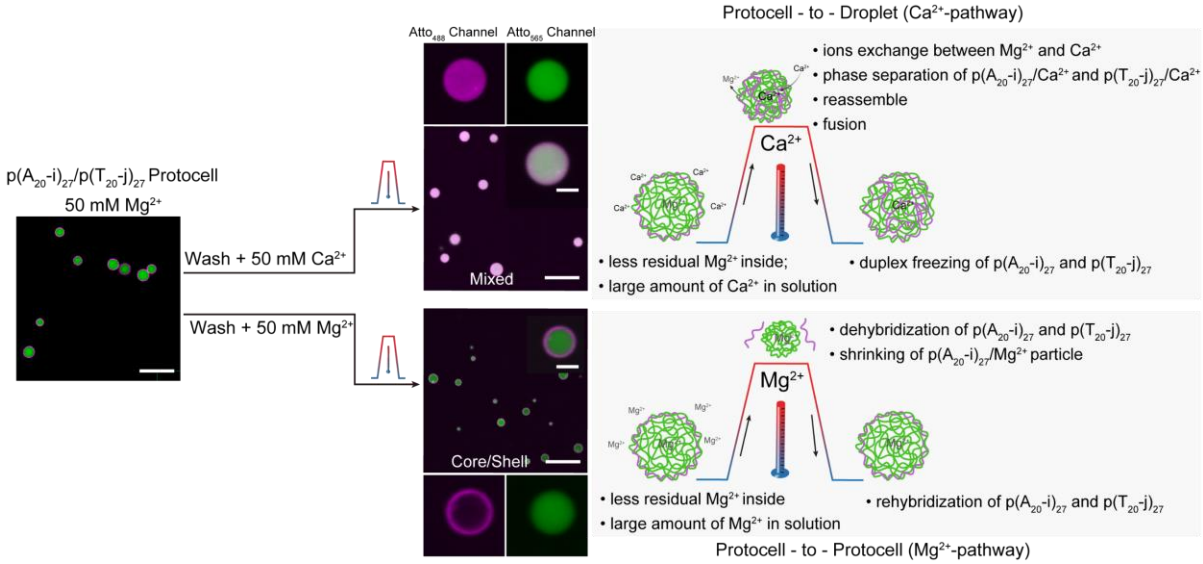

Figure S2.7. Morphological investigations of $p(A_{20}\text{-}i)_{27}/p(T_{20}\text{-}j)_{27}/Mg^{2+}$ protocells at Ca^{2+} or Mg^{2+} ions. Morphological investigations of $p(A_{20}\text{-}i)_{27}/p(T_{20}\text{-}j)_{27}$ protocell prepared via Mg^{2+}-pathway, and subsequently subjected to a temperature ramp in the presence of Ca^{2+} or Mg^{2+} ions. Scale bar: 10 µm. inset: 2 µm.

2.5 References

1. Alberti, S., Gladfelter, A. & Mittag, T. Considerations and Challenges in Studying Liquid-Liquid Phase Separation and Biomolecular Condensates. *Cell* **176**, 419-434 (2019).
2. Hyman, A.A., Weber, C.A. & Julicher, F. Liquid-liquid phase separation in biology. *Annu. Rev. Cell Dev. Biol.* **30**, 39-58 (2014).
3. Yin, Y. et al. Non-equilibrium behaviour in coacervate-based protocells under electric-field-induced excitation. *Nat. Commun.* **7**, 10658 (2016).

4. Banani, S.F. et al. Compositional Control of Phase-Separated Cellular Bodies. *Cell* **166**, 651-663 (2016).
5. Banani, S.F., Lee, H.O., Hyman, A.A. & Rosen, M.K. Biomolecular condensates: organizers of cellular biochemistry. *Nat. Rev. Mol. Cell Biol.* **18**, 285-298 (2017).
6. Kaur, T. et al. Sequence-encoded and composition-dependent protein-RNA interactions control multiphasic condensate morphologies. *Nat. Commun.* **12**, 872 (2021).
7. Goetz, S.K. & Mahamid, J. Visualizing Molecular Architectures of Cellular Condensates: Hints of Complex Coacervation Scenarios. *Dev. Cell* **55**, 97-107 (2020).
8. Brangwynne, C.P., Tompa, P. & Pappu, R.V. Polymer physics of intracellular phase transitions. *Nat. Phys.* **11**, 899-904 (2015).
9. Pederson, T. The nucleolus. *Cold Spring Harb. Perspect. Biol.* **3**, a000638 (2011).
10. Dundr, M. et al. In vivo kinetics of Cajal body components. *J. Cell Biol.* **164**, 831-842 (2004).
11. Mao, Y.S., Zhang, B. & Spector, D.L. Biogenesis and function of nuclear bodies. *Trends Genet.* **27**, 295-306 (2011).
12. Decker, C.J. & Parker, R. P-bodies and stress granules: possible roles in the control of translation and mRNA degradation. *Cold Spring Harb. Perspect. Biol.* **4**, a012286 (2012).
13. Nandana, V. & Schrader, J.M. Roles of liquid-liquid phase separation in bacterial RNA metabolism. *Curr. Opin. Microbiol.* **61**, 91-98 (2021).
14. Nosella, M.L. & Forman-Kay, J.D. Phosphorylation-dependent regulation of messenger RNA transcription, processing and translation within biomolecular condensates. *Curr. Opin. Cell Biol.* **69**, 30-40 (2021).
15. O'Connell, J.D., Zhao, A., Ellington, A.D. & Marcotte, E.M. Dynamic reorganization of metabolic enzymes into intracellular bodies. *Annu. Rev. Cell Dev. Biol.* **28**, 89-111 (2012).
16. Abbas, M., Lipinski, W.P., Wang, J. & Spruijt, E. Peptide-based coacervates as biomimetic protocells. *Chem. Soc. Rev.* **50**, 3690-3705 (2021).
17. Strulson, C.A., Molden, R.C., Keating, C.D. & Bevilacqua, P.C. RNA catalysis through compartmentalization. *Nat. Chem.* **4**, 941-946 (2012).
18. Martin, N. Dynamic Synthetic Cells Based on Liquid-Liquid Phase Separation. *Chembiochem* **20**, 2553-2568 (2019).
19. Love, C. et al. Reversible pH-Responsive Coacervate Formation in Lipid Vesicles Activates Dormant Enzymatic Reactions. *Angew. Chem. Int. Ed.* **59**, 5950-5957 (2020).
20. Nakashima, K.K., Baaij, J.F. & Spruijt, E. Reversible generation of coacervate droplets in an enzymatic network. *Soft Matter* **14**, 361-367 (2018).
21. Samanta, A., Sabatino, V., Ward, T.R. & Walther, A. Functional and morphological adaptation in DNA protocells via signal processing prompted by artificial metalloenzymes. *Nat. Nanotechnol.* **15**, 914-921 (2020).
22. Deng, J. & Walther, A. Programmable ATP-Fueled DNA Coacervates by Transient Liquid-Liquid Phase Separation. *Chem* **6**, 3329-3343 (2020).
23. Poudyal, R.R. et al. Template-directed RNA polymerization and enhanced ribozyme catalysis inside membraneless compartments formed by coacervates. *Nat. Commun.* **10**, 490 (2019).
24. Adamala, K. & Szostak, J.W. Competition between model protocells driven by an encapsulated catalyst. *Nat. Chem.* **5**, 495-501 (2013).
25. Weiss, M. et al. Sequential bottom-up assembly of mechanically stabilized synthetic cells by microfluidics. *Nat. Mater.* **17**, 89-96 (2018).
26. Palivan, C.G. et al. Bioinspired polymer vesicles and membranes for biological and medical applications. *Chem. Soc. Rev.* **45**, 377-411 (2016).
27. Yasuhara, S. et al. Enhancement of Ultrahigh Rate Chargeability by Interfacial Nanodot BaTiO3 Treatment on LiCoO2 Cathode Thin Film Batteries. *Nano Lett.* **19**, 1688-1694 (2019).
28. Ugrinic, M. et al. Microfluidic formation of proteinosomes. *Chem. Commun.* **54**, 287-290 (2018).
29. Aumiller, W.M.J. & Keating, C.D. Phosphorylation-mediated RNA/peptide complex coacervation as a model for intracellular liquid organelles. *Nat. Chem.* **8**, 129-137 (2016).
30. Fraccia, T.P. & Jia, T.Z. Liquid Crystal Coacervates Composed of Short Double-Stranded DNA and Cationic Peptides. *ACS Nano* **14**, 15071-15082 (2020).
31. Xing, Y. et al. Self-assembled DNA hydrogels with designable thermal and enzymatic responsiveness. *Adv. Mater.* **23**, 1117-1121 (2011).
32. Guo, W. et al. Reversible Ag(+)-crosslinked DNA hydrogels. *Chem. Commun.* **50**, 4065-4068 (2014).
33. Li, J. et al. Self-assembly of DNA nanohydrogels with controllable size and stimuli-responsive property for targeted gene regulation therapy. *J. Am. Chem. Soc.* **137**, 1412-1415 (2015).

34. Merindol, R., Loescher, S., Samanta, A. & Walther, A. Pathway-controlled formation of mesostructured all-DNA colloids and superstructures. *Nat. Nanotechnol.* **13**, 730-738 (2018).
35. Ludwanowski, S., Samanta, A., Loescher, S., Barner-Kowollik, C. & Walther, A. A Modular Fluorescent Probe for Viscosity and Polarity Sensing in DNA Hybrid Mesostructures. *Adv. Sci.* **8**, 2003740 (2021).
36. Zhao, W., Ali, M.M., Brook, M.A. & Li, Y. Rolling circle amplification: applications in nanotechnology and biodetection with functional nucleic acids. *Angew. Chem. Int. Ed.* **47**, 6330-6337 (2008).
37. Ali, M.M. et al. Rolling circle amplification: a versatile tool for chemical biology, materials science and medicine. *Chem. Soc. Rev.* **43**, 3324-3341 (2014).
38. Cho, E.J., Yang, L., Levy, M. & Ellington, A.D. Using a Deoxyribozyme Ligase and Rolling Circle Amplification. *J. Am. Chem. Soc.* **127**, 2022-2023 (2005).
39. Ali, M.M. & Li, Y. Colorimetric sensing by using allosteric-DNAzyme-coupled rolling circle amplification and a peptide nucleic acid-organic dye probe. *Angew. Chem. Int. Ed.* **48**, 3512-3515 (2009).
40. Ralec, C., Henry, E., Lemor, M., Killelea, T. & Henneke, G. Calcium-driven DNA synthesis by a high-fidelity DNA polymerase. *Nucleic Acids Res.* **45**, 12425-12440 (2017).
41. Korolev, N., Lyubartsev, A.P., Rupprecht, A. & Nordenskiöld, L. Competitive Binding of Ions to DNA in Oriented DNA Fibers. *Biophys. J.* **77**, 2736-2749 (1999).
42. Bellamy, S.R., Kovacheva, Y.S., Zulkipli, I.H. & Halford, S.E. Differences between Ca^{2+} and Mg^{2+} in DNA binding and release by the SfiI restriction endonuclease: implications for DNA looping. *Nucleic Acids Res.* **37**, 5443-5453 (2009).
43. Ahmad, R., Arakawa, H. & Tajmir-Riahi, H.A. A Comparative Study of DNA Complexation with Mg(II) and Ca(II). *Biophys. J.* **84**, 2460-2466 (2003).
44. Xu, H.-T., Zhang, N., Li, M.-R. & Zhang, F.-S. Comparison of the ionic effects of Ca^{2+} and Mg^{2+} on nucleic acids in liquids. *J. Mol. Liq.* **344**, 117781 (2021).
45. Hackl, E.V., Kornilova, S.V. & Blagoi, Y.P. DNA structural transitions induced by divalent metal ions in aqueous solutions. *Int. J. Biol. Macromol.* **35**, 175-191 (2005).
46. Langlais, M., Tajmir-Riahi, H.A. & Savoie, R. Raman spectroscopic study of the effects of Ca^{2+}, Mg^{2+}, Zn^{2+}, and Cd^{2+} ions on calf thymus. *Biopolymers* **30**, 743-752 (1990).
47. Wu, Y.-H., Wang, D.-M. & Lai, J.-Y. Effects of Polymer Chain Length and Stiffness on Phase Separation Dynamics of Semidilute Polymer Solution. *J. Phys. Chem. B* **112**, 4604-4612 (2008).
48. Wang, B. et al. ULK1 and ULK2 Regulate Stress Granule Disassembly Through Phosphorylation and Activation of VCP/p97. *Mol. Cell.* **74**, 742-757 (2019).
49. Gwon, Y. et al. Ubiquitination of G3BP1 mediates stress granule disassembly in a context-specific manner. *Science* **372**, eabf6548 (2021).
50. Samanta, A., Horner, M., Liu, W., Weber, W. & Walther, A. Signal-processing and adaptive prototissue formation in metabolic DNA protocells. *Nat. Commun.* **13**, 3968 (2022).

3 Switchable Hydrophobic Pockets in DNA Protocells Enhance Chemical Conversion

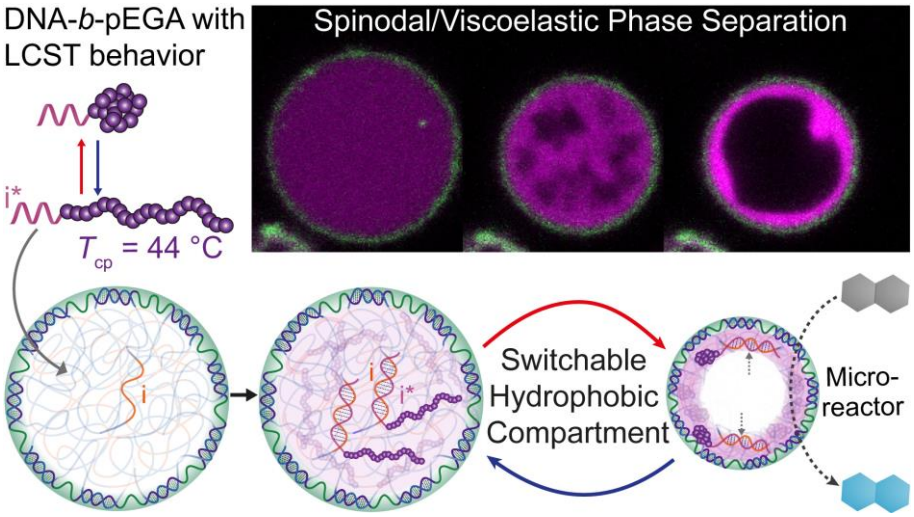

Preliminary note: *This chapter is based on the article published in J. Am. Chem. Soc. 145, 7090−7094 (2023). Minor changes have been made concerning formatting style.*

Abstract: Synthetic cell models provide simple means to better understand living cells and the origin-of-life. Key aspects of living cells are crowded interiors where secondary structures can easily form, such as the cytoskeleton and membraneless organelles/condensates. These can form dynamically and serve structural or functional purposes, such as protection from heat shock or as crucibles for various biochemical reactions. Inspired by these phenomena, we introduce a crowded all-DNA protocell and embed a temperature-switchable DNA-*b*-polymer block copolymer, in which the synthetic polymer can undergo phase segregation at elevated temperatures. We show that phase segregation of the synthetic polymer occurs by spinodal/viscoelastic decomposition and leads to the formation of artificial organelle structures that can reorient into larger phase-segregated domains depending on the viscoelastic properties of the protocell interior. This compartment formation is reversible. Fluorescent sensors confirm the formation of hydrophobic compartments, and we elucidate the enhanced reactivity of a bimolecular reaction within these compartments. This study demonstrates how to harness the individual strength of biological and synthetic polymers to construct advanced biohybrid artificial cells that offer insights into phase segregation under macromolecularly crowded conditions and the formation of syn-thetic organelles and microreactors in response to environmental changes.

3.1 Introduction

Synthetic cells have been identified as simple models for mimicking the behavior of living cells and to better understand the origin of life.[1, 2] Macromolecular coacervates based on DNA, RNA, and peptides are emerging synthetic cell models as they contain a large amount of biomolecules and provide a programmable, molecularly crowded interior in which chemical reactions and morphological transitions can be studied. Various approaches to their formation have been reported.[3–7] We and others introduced all-DNA protocells (PCs),[8–11] that provide a platform to study cell-inspired processes in a crowded interior using programmable design.[12–14]

Spatiotemporal compartmentalization in living cells provides segregated microenvironments in the form of membraneless organelles, which is crucial for biological reactions and cellular functionalities.[15–18] Such condensates typically form via a binodal nucleation−growth mechanism of liquid−liquid phase separation (LLPS). Minimization of interfacial free energy results in spherical shapes. Such condensates

can form in response to external triggers such as heat, leading to the heat shock protection pathway.[19,20] Recently, condensates with nonspherical structures have been discovered, but their formation mechanism remains elusive.[21–24]

Herein, we introduce a bottom-up process to investigate subcompartmentalization in artificial cells by combining all-DNA core/shell PCs[11] with a ssDNA-b-polyethylene glycol acrylate (i*-*b*-pEGA) block copolymer (BCP; Figure 3.1). The ssDNA part (i*) of the BCP is designed to bind to the barcode domains (i) in the PC core. The synthetic part pEGA has a lower critical solution temperature (LCST) that induces phase separation upon heating. We will show that phase separation occurs during a heat shock, and that initial bicontinuous structures reorient to concentric domains. Structure formation can be controlled by changing the viscoelastic properties of the DNA PC core. These compartments entrap hydrophobic molecules and act as reaction crucibles to enhance bimolecular reactions. This compartment technology offers insights into phase separation under crowded conditions and at high concentrations and enables new strategies for switchable reactivity in artificial cells.

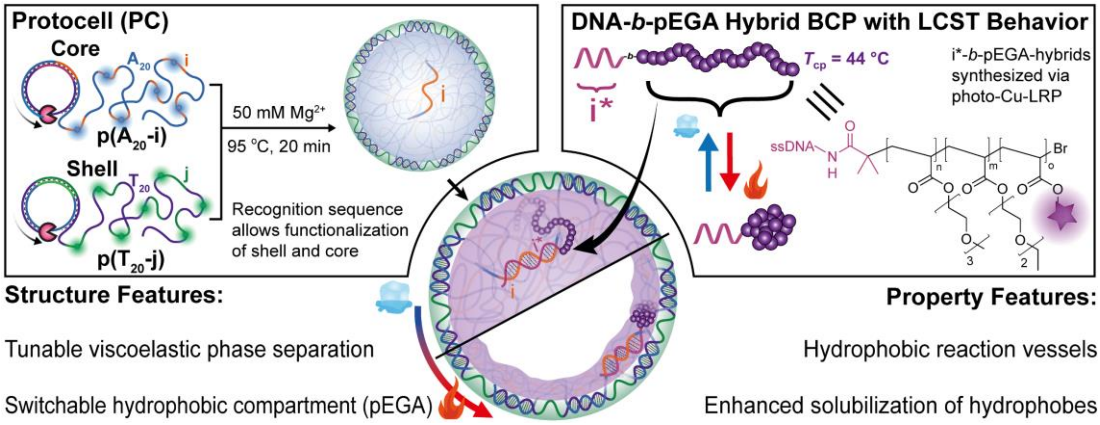

Figure 3.1. All-DNA PCs with switchable hydrophobic compartments: PC preparation, DNA-*b*-pEGA structure, and temperature switchable behavior. Core/shell PCs are prepared from a homogeneous mixture of two ssDNA polymers (p(A_{20}-i) and p(T_{20}-j)) using a heating ramp in the presence of 50 mM Mg^{2+}. Dye-labeled i*-*b*-pEGA hybrids are synthesized by Cu-LRP. pEGA exhibits LCST behavior. Uptake of i*-*b*-pEGA and subsequent heat shock leads to intra-PC phase segregation, structural evolution, and hydrophobic reaction compartments.

3.2 Results and Discussion

3.2.1 Reversible and Controllable Compartment Formation Within PCs

To enable the formation of switchable hydrophobic compartments, we synthesized a dye-labeled DNA-*b*-pEGA BCP using photo-mediated Cu-controlled living radical polymerization (Cu-LRP).[25] The ssDNA part (i*) is complementary to the i barcodes in

the PC core and was functionalized with the Cu-LRP initiator (Figure S3.1). We used a comonomer mixture of triethylene glycol methyl ether acrylate (mTEGA) and diethylene ethyl ether acrylate (eDEGA) to tune the cloud point temperature (T_{cp}; Figure 3.2a). Trace amounts of rhodamine (Rhd) acrylate serve as fluorescent markers. We targeted a molar ratio of mTEGA/eDEGA of 55/45 to achieve a T_{cp} of 43 °C in dilute solution.[26] Gel Permeation Chromatography (GPC) exhibits a linear evolution of molecular weights with conversion and narrow dispersities ($Đ$ = 1.16, Figure 3.2b; Figure S3.2). This indicates a controlled polymerization. In the following we focus on an i*-*b*-pEGA BCP with ca. 780 repeating units in the pEGA moiety to allow for a substantial volume fraction of phase-separated segments. Temperature-dependent turbidity measurements reveal a T_{cp} of 44 °C at 15 mM Mg^{2+} of a 0.3 g/L solution (Figure 3.2c). This value is appropriate as it is below the melting temperature, T_m, of the i/i* (65 °C) providing immobilization in the core and A_{20}/T_{20} (58 °C) stabilizing the PC at the core/shell interface.

Core/shell PCs were assembled by kinetically trapping p(A_{20}-i) coacervates, formed during heating, with p(T_{20}-j) during cooling in a temperature ramp up to 95 °C at 50 mM Mg^{2+}.[11] This leads to PCs with a liquid interior of p(A_{20}-i) stabilized by a hydrogel shell of A_{20}/T_{20}-duplexes formed by p(A_{20}-i)/p(T_{20}-j). A_{20} and T_{20} refer to homosequences containing 20 adenine and thymine bases, while i and j represent barcode sequences for functionalization. Immobilization of Rhd-labeled i*-*b*-pEGA (magenta) into DNA PCs is achieved by diffusion in 100 mM NaCl TE buffer at 25 °C (Figure 3.2d; Figure S3.3a, b). A uniform magenta color indicates a homogeneous uptake. The salinity can be adjusted, or agents for cross-linking can be added. In general, we adjusted the concentration of Mg^{2+} to 15 mM to stabilize the PCs during the heat shock experiments (the scheme for the loading process is in Figure S3.4).

To understand whether the heat-induced phase separation of pEGA still occurs within the crowded DNA PC core, we subjected the hybrid PC/i*-*b*-pEGA to a heating ramp up to 48 °C (T_{cp} of i*-*b*-pEGA = 44 °C) and monitored the behavior in situ in a heating cell under a confocal laser scanning microscope (CLSM). Figure 3.2d shows the phase separation of pEGA by formation of a bicontinuous structure, its coarsening, and finally the formation of a concentric ring. During this heat shock, the average diameter of the PCs decreases from ca. 7.3 to 3.9 µm (Figure S3.3e). Upon cooling, uniform magenta fluorescence reappears, confirming full reversibility (Figure 3.2d; Figure S3.3). The

network-like structure arises from classical spinodal or viscoelastic phase separation (overview images in Figure S3.3a−d).[23] A deeper mechanistic analysis is prevented due to limited PC size and spatiotemporal resolution.[27] The shrinkage arises from hydrophobic collapse and the formation of an inner interface that seeks to minimize itself.

The process is mechanistically robust. It can be triggered multiple times, and increasing the temperature or incubation time at a constant temperature above T_{cp} results in the same PC structures (Figure S3.5). We found slight variations in the exact transition temperature for the onset of phase segregation, which we associate with minimally different loading amounts of i*-*b*-pEGA. To effectively implement the compartmentalization process, we chose the temperature ramp to typically reach 55 °C in the following.

Next, we address the question of why phase separation transitions into a concentric layer during heat shock. Intuitively, the coarsening is caused by surface energy minimization and concentric layer formation by interfacial adhesion to the shell. In principle, the interfacial adhesion is because a part of p(A_{20}-i) in the core is bound to p(T_{20}-j) in the shell. However, this interfacial adhesion can remain effective only if the heat-induced phase separation of pEGA does not lead to dissociation of the i/i* barcode bonds that tether the i*-*b*-pEGA to the p(A_{20}-i) core. This culminates in the question whether the pEGA cosequesters p(A_{20}-i) or whether it is torn off during phase segregation at the i/i* duplex. Therefore, we covalently labeled p(A_{20}-i) with Atto$_{647}$. Indeed, during heating the Rhd-labeled i*-*b*-pEGA and p(A_{20}-i)-Atto$_{647}$ colocalize (magenta and blue in Figure 3.2e−g). This confirms the co-condensation of p(A_{20}-i) and i*-b-pEGA due to prevailing hybridization of i/i*. This synergy also helps to understand why spinodal or viscoelastic decomposition occur. Classical binodal phase separation would occur at a low concentration in a test tube, while the high concentration in PCs allows us to attain the highly concentrated region required for triggering spinodal or viscoelastic decomposition.[15, 28]

To understand how the viscoelastic properties of PCs affect structure formation, we employed a different divalent cation (Ca^{2+}) and a DNA palindrome-cross-linker (i*-P_8) to prepare PCs with nondynamic and cross-linked interior (Figure 3.2h−j). Previously, we showed that Ca^{2+} leads to a more arrested PC interior.[29] Indeed, when 25 mM Ca^{2+} is added to a PC/i*-*b*-pEGA dispersion at 15 mM Mg^{2+}, phase separation is arrested

because of a lack of molecular mobility (Figure 3.2i). Moreover, when PC/i*-*b*-pEGA is co-crosslinked with a self-hybridizing i*-P_8 palindrome domain,[30] the phase separation is restricted to nanoscopic domains (recall the resolution limits of CLSM, details in Figure S3.6a). A slight shrinkage of 17% occurs (Figures 3.2j, S3.6b,c). In summary, different PC compartment structures can be achieved by adjusting the dynamics.

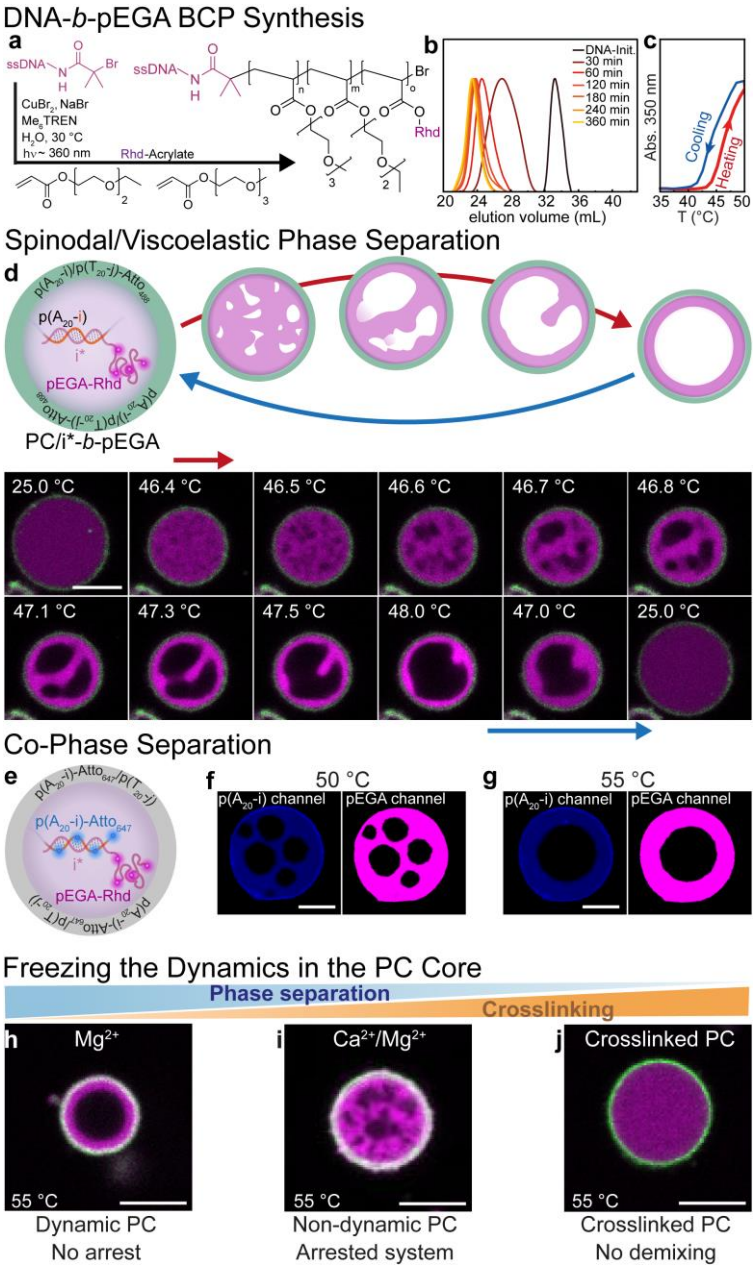

Figure 3.2. i*-*b*-pEGA BCP synthesis, and reversible and controllable compartment formation within PCs. (a–c) Synthesis and properties of Rhd-labeled i*-*b*-pEGA BCP: **(a)** Synthetic scheme. **(b)** GPC data shows a clear shift of molecular weight traces with conversion and narrow dispersities. **(c)** Turbidity measurements reveal a T_{cp} of 44 °C of a 0.3 g/L solution. **(d)** Thermoreversible phase separation of pEGA segments (magenta) within PCs follows spinodal/viscoelastic decomposition. **(e–g)** Co-phase separation behavior of p(A_{20}-i)-Atto$_{647}$ (blue) and i*-*b*-pEGA (magenta) occurs during heat shock. **(h–j)** Viscoelastic properties of the PCs control compartment size at high temperature: **(h)** Dynamic PCs. **(i)** Arrested phase separation in the presence of additional 25 mM Ca^{2+}. **(j)** Slight shrinkage but no visible phase separation occurs in PC/i*-*b*-pEGA co-crosslinked with a self-cross-linking palindrome domain (i*-P_8) at a ratio of i*-P_8/i*-*b*-pEGA of 1:9 (see Figure S3.6a–c). Scale bar: 5 µm. All experiments carried out at 15 mM Mg^{2+}.

3.2.2 Hydrophobic Subcompartments Sequester Hydrophobic Molecules and Promote Reactions

To investigate the potential of co-phase-segregated p(A_{20}-i)/i*-*b*-pEGA as a hydrophobic reaction crucible, we investigated the sequestration of a dye known to sense hydrophobic environments with a fluorescence increase (BODIPY 493/503, blue in Figure 3.3c).[31] To avoid crosstalk in the emission channels, we used an unlabeled i*-*b*-pEGA to form the PC/i*-*b*-pEGA hybrids. BODIPY fluorescence within the PC core is absent at room temperature but appears within the concentric layer of the phase-separated structure at 55 °C (Figure 3.3a−c). Fluorescence measurements show a 3-fold increase in BODIPY fluorescence upon heating (Figure 3.3d). This confirms the increased solubility for hydrophobic molecules in the subcompartment.

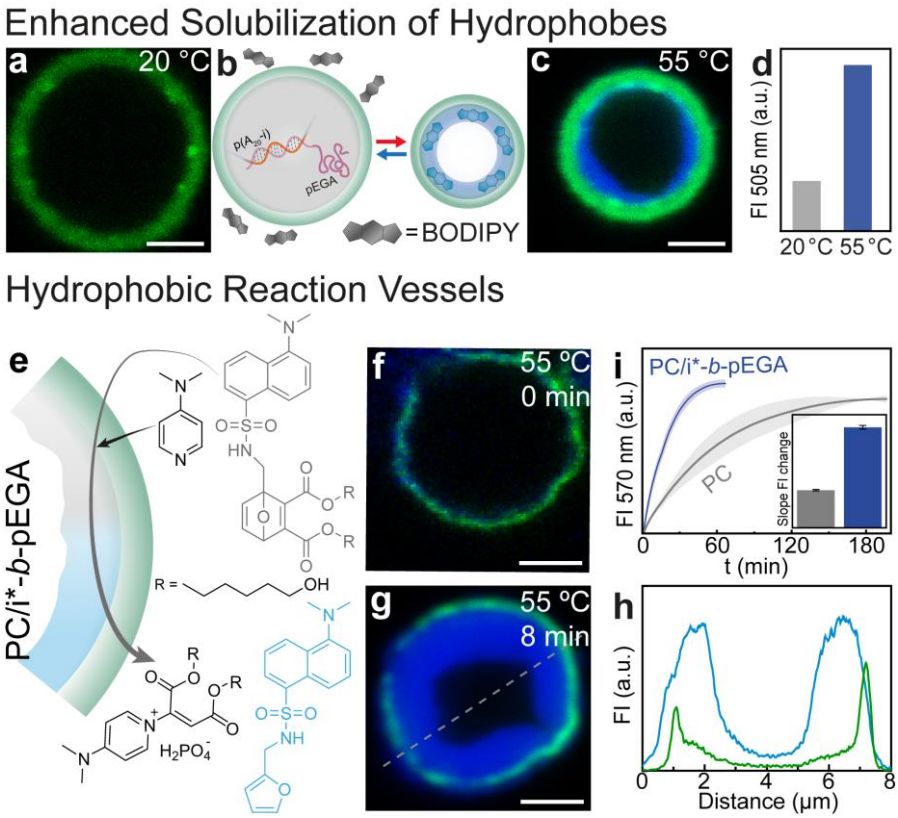

Figure 3.3. Hydrophobic subcompartments sequester hydrophobic molecules and promote reactions. (a−d) Solubilization of BODIPY 493/503 (blue) in PC/i*-*b*-pEGA hybrids: **(a−c)** No fluorescence within PC core at room temperature, but strong blue fluorescence within the phase-separated structure at 55 °C. **(d)** Fluorescence increase of hybrid PC/i*-*b*-pEGA at 55 °C compared with 20 °C. **(e−h)** PC/i*-*b*-pEGA hybrids accelerate the self-reporting bimolecular reaction which provides a fluorophore readout (blue): (e) Scheme. **(f−g)** CLSM images show the reaction progress at 55 °C. **(h)** Line segment analysis of (g). **(i)** Time-dependent fluorescence of the reaction within PC/i*-*b*-pEGA hybrids vs normal PCs without i*-*b*-pEGA. Inset: Slope of the fluorescence increase by linear fitting during the first 5 min. Scale bar: 2 µm.

Finally, we question if such hydrophobic compartments can accelerate reactions, as is known from intracellular organelles. We use a self-reporting bimolecular reaction

based on a protected dansylfuran that undergoes a retro-Diels−Alder reaction when exposed to nucleophiles such as 4-dimethylaminopyridine (DMAP; Figure 3.3e).[32] The reaction provides a facile readout as the released dansylfuran is a fluorophore (blue in Figure 3.3g, products confirmed by mass spectrometry in Figure S3.7). The reaction was expected to prefer a hydrophobic environment since the pro-fluorophore and the products are hydrophobic. Tracking the fluorescence change inside the PC allows analysis of the reaction. Blue fluorescence increases with time at 55 °C (Figure 3.3f, g), and the fluorescence accumulates only in the hydrophobic subcompartments (Figure 3.3h). For comparison, we also compared the fluorescence increase for a pristine PC without i*-*b*-pEGA at 55 °C (Figure 3.3i; Figure S3.8). Although the reaction also occurs, the product formation is much slower and cannot be localized to a PC. The hybrid PC/i*-*b*-PEGA accelerates the reaction 3-fold. As a control, there is no significant difference in reaction between a PC and a hybrid PC/i*-*b*-pEGA in the non-phase-segregated state at 25 °C (Figure S3.9). Hence, it becomes evident that the hydrophobicity imparted by the synthetic BCP compartments can confer a functional reactivity enhancement to the artificial cell structure.

3.3 Conclusion

In conclusion, we have shown how to leverage synergies between the DNA world and synthetic BCPs to create switchable hydrophobic domains in hybrid PCs. We found that phase separation inside of the PCs proceeds via spinodal/viscoelastic decomposition, which contrasts with binodal decomposition in dilute solution. The transition from a network to a concentric layer can be explained by cocondensation of the ssDNA interior and the synthetic BCP segment. The extent of phase separation can be tuned by changing the viscoelastic properties of the DNA PC core with salt and/or specific DNA-based cross-linking, which should allow further fine control over secondary structuration inside PCs in the future. Observation of spinodal/viscoelastic decomposition and interface wetting layer formation offers new insight into phase separation under viscoelastic confinement, and we propose that such programmable DNA PCs are an ideal vehicle to study such processes. The ability to control compartment morphologies opens new ways to design tunable compartments for catalytic reactions, information transfer, and partitioned storage. The enrichment of hydrophobic molecules in the resulting hydrophobic compartments allows complex chemical reactions with poorly soluble reactants to proceed faster, thus expanding the

prospects of such structured artificial cell models for applications as selective microreactors.

3.4 Supplementary Information

3.4.1 Reagents and Solvents

Ac-dA SynbaseTM CPG 1000/110 and Ac-dT SynbaseTM CPG 1000/110 were purchased from Link Technology. DMT-dA(bz) phosphoramidite, DMT-dG(dmf) phosphoramidite, DMT-dC(bz) phosphoramidite, and DMT-dT phosphoramidite (99 %) were purchased from Sigma Aldrich and dissolved in anhydrous acetonitrile prior to use. CAP A (THF/pyridine/acetic anhydride, 8:1:1), CAP B (10 % methylimidazole in THF), trichloroacetic acid deblock (TCA Deblock, 3 % in DCM), 5-(Ethylthio)-1H-tetrazole (ETT Activator, 3 % in ACN), Oxidizer (pyridine/water/iodine, 9:1:12.7), 2-bromoisobutanoic acid N-hydroxysuccinimide ester (≥ 98 %), NaBr (≥ 99 %), Calcium acetate ($CaAc_2$), Magnesium chloride ($MgCl_2$), Sodium chloride (NaCl, 99%), Sodium Phosphate Dibasic (Na_2HP_4), Potassium Phosphate Monobasic (KH_2PO_4), Potassium Chloride (KCl), Acetic acid, Tris(hydroxymethyl)-aminomethane hydrochloride (Tris, pH=8), Ethylenediaminetetraacetic acid disodium salt dihydrate (EDTA), 4-dimethylaminopyridine (DMAP), and Trizma base were purchased from Sigma-Aldrich and used as received. MMT-protected 5'-amino-modifier C6 (99 %) was purchased from Glen Research and dissolved in anhydrous ACN prior to use. Triethylene glycol methyl ether acrylate (mTEGA) (> 98 %) and diethylene ethyl ether acrylate (eDEGA) (> 98 %) were purchased from TCI Germany. Monomers were passed through a short column of basic alumina prior to use to remove the radical inhibitor. Tris[2-(dimethylamino)ethyl]amine (Me_6TREN) (99 %) was purchased from ABCR GmbH. $CuBr_2$ (99 %), Triethylamine (99 %), and basic alumina were purchased from Merck. All DNA oligonucleotides (except the ssDNA-macroinitiator) and nuclease-free water were ordered from Integrated DNA Technologies (IDT). NxGen T4 DNA ligase (2 U/µL and 20 U/µL), Exonuclease I (20 U/µL), Exonuclease III (200 U/µL), and Φ29 DNA polymerase (10 U/µL) were supplied by Lucigen. Inorganic pyrophosphatase (0.1 U/µL) was supplied from New England Biolabs (NEB). dNTP Bundle (dATP, dCTP, dGTP, dTTP; 4 × 100mM), Aminoallyl-dUTP-ATTO647N, and Aminoallyl-dUTP-XX-ATTO-488 were purchased from Jena Bioscience GmbH. BODIPY 493/503 was purchased from Thermo Fisher Scientific.

3.4.2 Methods of Analysis

3.4.2.1 Nuclear Magnetic Resonance (NMR)

NMR analysis was conducted with a Brucker Avance III HD 300 at 300 MHz using deuterated Dimethyl sulfoxide (DMSO) as solvent.

3.4.2.2 High-Performance Liquid Chromatography (HPLC)

A Thermo Fischer Scientific Dionex Ultimate 3000 HPLC system was used and chromatograms were processed using the Chromeleon data system.

DNA samples were dissolved in water and separated by using a gradient from 100 % A to 75 % A with solvent A being 0.1 M triethyl ammonium acetate (TEAA) buffer in 95/5 water/acetonitrile, and solvent B being acetonitrile. A Thermo Scientific DNAPac 4 µm, 3.0 × 100 mm reversed phase column was used.

Small molecule samples were dissolved in water and separated by using a gradient from 100 % water to 100 % acetonitrile. A Kromasil 100-5-C18, 4.6 × 250 mm reversed phase column was used.

All the experiments were performed at 40 °C.

3.4.2.3 Gel Permeation Chromatography (GPC)

GPC analysis was conducted using an Agilent 1260 Infinity II using dimethylacetamide (DMAc) with 0.5 % LiBr as eluent. For separation, a GRAM high speed linear column system (molar mass range: 500–1000 kDa) was used. The measurement was carried out at 50 °C. The traces were calibrated with PMMA of low dispersity.

3.4.2.4 Matrix-Assisted Laser-Desorption-Ionization Time of Flight Mass Spectrometry (MALDI-ToF MS)

Matrix-assisted laser-desorption-ionization time of flight mass spectrometry (MALDI-ToF MS) measurements were performed using matrix consisting of 3-hydroxy picolinic acid and diammonium citrate. The measurements are conducted on an autoflex maX MALDI-TOF-MS from Bruker.

3.4.2.5 UV-VIS Spectroscopy

Lower critical solution temperature (LCST) measurements were conducted on an Analytic Jena Scandrop connecting with JUMO DTRON 308 temperature controller. The DNA concentrations were measured with a DeNovix DS-11 spectrophotometer.

3.4.2.6 Confocal Laser Scanning Microscopy (CLSM)

CLSM was performed on Leica Stellaris 5 equipped with a microheating stage and temperature controller from VAHEAT.

3.4.2.7 Fluorescence Spectroscopy

Fluorescence experiments were done using an Ocean QE Spectrometer with a setup consisting of an Ocean CUV-QPOD temperature-controlled cuvette holder and a 365 nm and 490 nm LED source coupled via optic fiber (Mightex).

3.4.2.8 Electrospray Ionization Mass Spectrometry (ESI-MS)

High resolution ESI-MS was carried out using an Agilent 6545 QTOF-HRAM-MS.

3.4.3 Oligonucleotide Sequences

Table S3.1. Oligonucleotide sequences used, with their names, the sequence codes, the purification methods, and the modifications.

	Name	Oligonucleotide sequence (5'-3')	Purification	Modification
Polymer	$p(A_{20}\text{-}i)_x$	[AAAAAAAAAAAAAAAAAAAA-TTAGGATAGATATACGGGTTC]$_x$		
	$p(T_{20}\text{-}j)_y$	[TTTTTTTTTTTTTTTTTTTT-GATTTTAGAGGATCGTGTGGTTTTAC]$_y$		
$p(A_{20}\text{-}i)_x$	Template ($T_p(A_{20}\text{-}i)_x$)	/5Phos/ATCTATCCTAATTTTTTTTTTTTTTTTTTTGAACCCGTAT	HPLC	5'-Phosphorylation
	Primer (i')	TTAGGATAGATATACGGGT*T*C	Desalting	Phosphorothioated Twice
	Ligation (i)	TTAGGATAGATATACGGGTTC	HPLC	None
$p(T_{20}\text{-}j)_y$	Template ($T_p(T_{20}\text{-}j)_y$)	/5Phos/ATCCTCTAAAATCAAAAAAAAAAAAAAAAAAAAGTAAAACCACACG	HPLC	5'-Phosphorylation
	Primer (j')	TTTTAGAGGATCGTGTGGTT*T*T	Desalting	Phosphorothioated Twice
	Ligation (j)	TTTTAGAGGATCGTGTGGTTTT	HPLC	None
	Crosslinker ($i^*\text{-}P_8$)	TGAACCCGTATATCTATCCTAAATCAA-GTAGCTAC	Desalting	None

3.4.4 Experimental Protocols

3.4.4.1 DNA-*b*-pEGA Hybrid Synthesis

(1) ssDNA macroinitiator synthesis

General procedure for automated DNA synthesis: Oligonucleotide sequences ($i^*\text{-}NH_2$) were synthesized on a H8-custom DNA/RNA synthesis apparatus from K&A Laborgeraete at 10 µmol scale using standard solid-phase-β-cyanoethylphosphoramidite chemistry. Synthesis was performed from the 3'- to the 5'-

end of oligonucleotide strands on packed Ac dA SynbaseTM CPG 1000/110 solid-phase columns. 50 mM solutions of standard DNA phosphoramidites such as DMT-dT, DMT-dA(bz), DMT-dG(dmf), and DMT-dC(ac) in dry acetonitrile were used for synthesis. The MMT-protected 5'-amino modifier C6 was used as the final phosphoramidite. At the end of the synthesis, the MMT group was cleaved by a prolonged TCA wash. The oligonucleotide supports were then washed with I and dried with N_2.

Cleavage of DNA oligonucleotides from solid support: The cleavage of the oligonucleotides from the solid support and the deprotection of the nucleobases were carried out in one step to achieve optimal yields. The phosphate group is protected by cyanoethyl groups and bases A, C and G are protected by different groups such as benzoyl (in the case of A and C) or isobutyl groups (for G). The T nucleotide has no protecting group. Cleavage of oligonucleotides from the solid support with a 1:1 mixture of ethylenediamine (EDA) and toluene for two hours at room temperature was chosen as the method of choice in this work. The solid support in the plastic carrier was wetted with the mixture (2 mL) using a syringe and allowed to stand for two hours. The EDA/toluene mixture was then washed out with pure toluene (5 mL). The cleaved, deprotected, and precipitated DNA was dried with a stream of N_2. The oligonucleotides were then washed out by rinsing the 75chlenk three times with water (3 mL). The remaining DNA residues were rinsed with another 2 mL of water. The combined solutions were freeze dried. The resulting crude DNA was purified by preparative HPLC to remove EDA residues.

Oligonucleotide modification: Purified i*-NH_2 (20 µmol, 1.0 eq.) was dissolved in 4.0 mL of a Na_2CO_3/$NaHCO_3$ buffer (pH = 9.0, 1.0 M). Then 2-bromoisobutanoic acid-N-hydroxysuccinimide ester (26.4 mg, 20 µmol, 10 eq.) was added. The mixture was stirred at room temperature for 1 h. The crude reaction mixture was then purified by preparative HPLC to remove excess reagents.

(2) photo-Cu-LRP (targeted DP_n = 800)

A schlenk tube was charged with DMF (5.0 µL) as the ^{1}H-NMR standard. Afterwards the following aqueous stock solutions were added in this order: DNA initiator (5.0 mM, 160 µL, 0.80 µmol, 1.0 eq.), $CuBr_2$ (100 mM, 64.0 µL, 6.40 µmol, 8.0 eq.), Me_6TREN (100 mM, 384 µL, 38.4 µmol, 48.0 eq.), NaBr (1000 mM, 8.0 µL, 8.0 µmol, 10.0 eq.)

and Rhd-acrylate (20 mM, 31.9 µL, 0.8 µmol, 0.8 eq.). Then, the pure monomers mTEGA (72.3 µL, 351.0 µmol, 440 eq.) and eDEGA (53.2 µL, 54.0 µmol, 360 eq.) were added. The reaction mixture was then filled up to 1130 µL with water. The mixture was stirred at room temperature for 2 min. The reaction mixture was then degassed four times via freeze-pump-thaw. Then, the solution was transferred to a sealed and N_2-flushed light scattering tube (100 x 5 mm) using an N_2-flushed syringe. The tube was laid under a NailStar® NS-01 UV nail lamp (λ_{max} ~ 365 nm) equipped with a hot plate at 30 °C. After 15 min had passed and the temperature of the solution had equilibrated, the UV light was turned on. Kinetic samples were taken at regular intervals (30, 60, 90, 120, and 180 min) under positive N_2 pressure. Samples were exposed to air and diluted in DMSO-D_6 (for NMR) and DMAc (for GPC measurements) and stored in the dark. The conversion was calculated by comparing the acrylate protons with the signal of DMF. Purification of the obtained polymer was performed by dialysis against demineralized water using a regenerated cellulose membrane with a cutoff molecular weight of 6-8 kD. The used BPC has a number average degree of polymerization of EGA of 780 units.

3.4.4.2 Low Critical Solution Temperature (LCST) Measurement of i*-*b*-pEGA

0.3 g/L i*-*b*-pEGA BCP with a number average degree of polymerization of EGA of 780 units in 15 mM Mg^{2+} TE buffer (pH = 8; 40 mM Tris, 20 mM acetic acid and 1 mM EDTA) was heated to 80 °C at a rate of 1 °C/min. Absorbance at 350 nm was recorded every minute.

3.4.4.3 All-DNA Protocell (PC) Formation

(1) Synthesis of ssDNA polymer (p(A_{20}-i) and p(T_{20}-j)) by rolling circle amplification (RCA)

Circular templates preparation: 1 µM linear ssDNA template, 1 µM ligation strand, and 100 mM NaCl were mixed in TE buffer to the final volume of 100 µL. The solution was rapidly heated to 85 °C (for 5 min) at a rate of 3 °C/s and then slowly cooled to 20 °C at a rate of 0.01 °C/s. The annealed solution, 1x T4 DNA ligase buffer, as well as 0.1 U/µL T4 DNA ligase, were added to nuclease-free water to the final volume of 200 µL. This mixture was gently shaken for 3 h at room temperature and then rapidly heated to 70 °C for 20 min at a rate of 3 °C/s to inactivate the T4 DNA ligase. Afterwards, 1 U/µL Exonuclease I and 5 U/µL Exonuclease III were added to the solution and

incubated overnight at 37 °C to remove unhybridized ligation strands and non-circularized templates. The mixture was then heated to 80 °C (for 40 min) to inactivate the two exonucleases. The resulting circular templates were purified using 10 kDa Amicon Ultra Centrifugal Filters and washed three times with TE buffer.

Polymerization reaction: 0.05 µM circular template, 0.1 µM primer, 1x Φ29 polymerase buffer, 0.2 U/µL Φ29 polymerase, 0.01 U/µL inorganic pyrophosphatase, 5 mM adjusted dNTP mixture, and nuclease-free water were mixed to the final volume of 200 µL. The mixture was gently shaken at 30 °C (for 60 h). The resulting ssDNA polymers were heated to 95 °C (for 15 min), and then purified using 30 kDa Amicon Ultra Centrifugal Filters and washed three times with TE buffer.

When needed, Aminoallyl-dUTP-ATTO647N or Aminoallyl-dUTP-XX-ATTO-488 (at a ratio of 2% of dTTP) was introduced in the dNTP mixture, composed of dATP, dTTP, dCTP, and dGTP in a ratio of the corresponding expected ssDNA polymer, to synthesize covalently labeled ssDNA polymers.

(2) Preparation of PCs

0.5 g/L (32.5 µM) p(A_{20}-i) and 0.0625 g/L p(T_{20}-j) were mixed in TE buffer and heated to 95 °C for 15 min with heating and cooling ramp of 3 °C/s for homogenization. Then 50 mM $MgCl_2$ was added to the solution for phase separation. The PCs were formed by heating the sample to 95 °C for 20 min at a rate of 3 °C/s. The solution was diluted ten times using TE buffer containing 50 mM Mg^{2+}.

When needed, covalent-labeled ssDNA polymers (e.g. p(A_{20}-i)-Att_{647}, p(T_{20}-j)-Att_{488}, and p(T_{20}-j)-Att_{647}) and non-labeled ssDNA polymers (e.g. p(A_{20}-i) and p(T_{20}-j)) were used to form PCs.

3.4.4.4 Phase Separation of i*-*b*-pEGA within PC (PC/i*-*b*-pEGA)

Encapsulation of i-b-pEGA and phase separation measurements:* To avoid crosstalk in the emission channels, we prepared shell-labeled PCs with p(A_{20}-i) core and p(A_{20}-i)/p(T_{20}-j)-$Atto_{488}$ shell. The PCs were washed with 100 mM Na^+ TE buffer to open the pores of the shell for better encapsulation of i*-*b*-pEGA *(EGA units = 780)*. Excess Rhd-labeled i*-*b*-pEGA (at a ratio of 1.1 eq. of I on p(A_{20}-i)) was added to the PCs solution and incubated overnight at room temperature for encapsulation. The solution was washed again with 100 mM Na^+ TE buffer to remove the free BCP in the solution

and the concentration of Mg^{2+} was adjusted to 15 mM. The sample was rapidly heated to 40 °C (lower than T_{cp} of polymer hybrid of 46 °C) at a rate of 3 °C/s, then slowly heated to 48 °C at a rate of 0.1 °C/s, rapidly cooled to room temperature at 3 °C/s. Images were recorded during this process using CLSM.

Temperature ramp selection: To effectively implement the phase separation process, we selected a standard temperature ramp to typically reach 55 °C.

Co-phase separation measurements: Core-labeled PCs with p(A_{20}-i)-$Atto_{647}$ core and p(A_{20}-i)-$Atto_{647}$/p(T_{20}-j) shell were prepared to investigate the behavior of p(A_{20}-i). The phase separation of i*-*b*-pEGA hybrid within PC was performed as described above and high temperature of 55 °C was used for the temperature ramp. Images were recorded during this process using CLSM.

3.4.4.5 Controllable Compartment Structures by Adjusting the Viscoelastic Properties of the PCs

PC/i*-*b*-pEGA were prepared as described in section 3.4.4.4. Then the samples were subjected to a temperature ramp with high temperature of 55 °C (the samples were rapidly heated to 40 °C at a rate of 3 °C/s, then slowly heated to 55 °C for 2 min at a rate of 0.1 °C/s, rapidly cooled to room temperature at 3 °C/s).

Dynamic PCs system (15 mM Mg^{2+}): 15 mM Mg^{2+} was added to the sample before the temperature ramp.

Non-dynamic PCs system (15 mM Mg^{2+}/25 mM Ca^{2+}): 15 mM Mg^{2+} and 25 mM Ca^{2+} were added to the sample before the temperature ramp.

Crosslinked PCs system (15 mM Mg^{2+}): A small amount of self-crosslinking palindrome domain i*-P_8 (i*-P_8 : i*-*b*-pEGA = 1 : 9) was introduced during encapsulation of the i*-*b*-pEGA to achieve tight crosslinking. Otherwise the sample was handled as above.

3.4.4.6 Enhanced Solubilization of Hydrophobes

PC/i*-*b*-pEGA hybrids were prepared as described in section 3.4.4.4. Then 20 µM BODIPY 493/505 (0.6 µL, 1 mM in acetonitrile) was added to the solution of 30 µL before subjecting with a temperature ramp. Images were recorded during this process using CLSM.

Fluorescence spectra were acquired for which the samples were heated to 55 °C for 10 min with a heating and cooling rate of 10 °C/min.

3.4.4.7 Reaction Crucible

PC/i*-*b*-pEGA hybrids were prepared as described in section 3.4.4.4 except that DPBS buffer (137.9 mM NaCl, 1.47 mM KH_2PO_4, 2.67 mM KCl, 8.09 mM Na_2HP_4) was used for washing process instead of 100 mM Na^+ TE buffer to avoid the reaction between protected dansylfuran and Tris.

CLSM Measurements: The protected dansylfuran (3.0 µL, 500 µM in DMSO; 1.5 nmol) was added to the PC/i*-*b*-pEGA solution of 24 µL on a microheating stage. The solution was rapidly heated to 55 °C at a rate of 5 °C/s. Then DMAP (3.0 µL, 1000 µM in water; 3.0 nmol) was added at 55 °C. The reaction with a final volume of 30 µL was recorded using CLSM.

Temperature-dependent fluorescence measurements: The protected dansylfuran (5.0 µL, 500 µM in DMSO; 2.5 nmol) was added to the PC/i*-*b*-pEGA solution of 40 µL in a cuvette. The solution was rapidly heated to 55 °C at a rate of 5 °C/s. Then DMAP (5.0 µL, 1000 µM in water; 5.0 nmol) was added at 55 °C. The development of fluorescence (λ_{ex} = 365 nm) at 55 °C was measured every minute. After full conversion (determined by negligible changes in fluorescence), the products were purified via HPLC chromatography and analyzed using ESI-MS.

The development of fluorescence (λ_{ex} = 365 nm) at 25 °C was also measured every minute while the same amount of DMAP was added at 25 °C.

As a comparison, pristine PCs without i*-*b*-pEGA were also prepared and used this reaction. Experiments were performed as described above, except that pristine PCs without i*-*b*-pEGA were used instead of PC/i*-*b*-pEGA.

3.4.5 Supplementary Figures

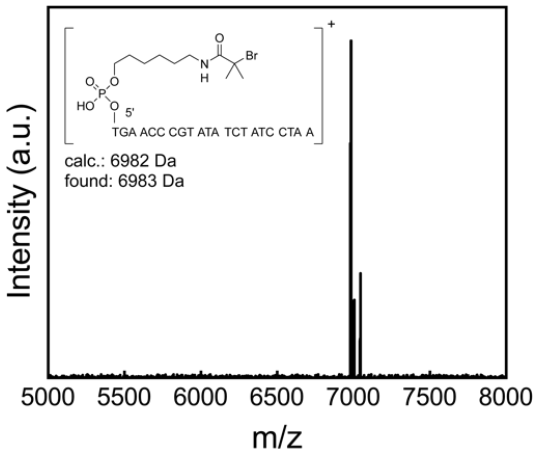

Figure S3.1. ssDNA macroinitiator synthesis. MALDI-TOF of ssDNA macroinitiator.

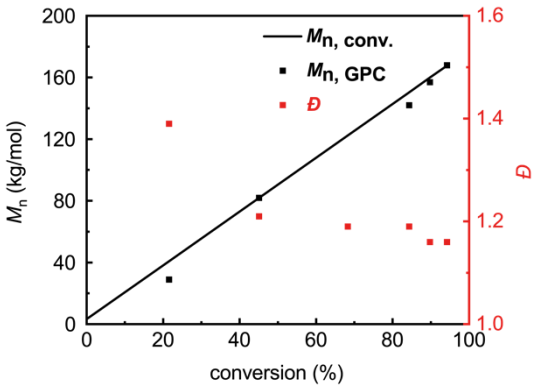

Figure S3.2. Synthesis of i*-*b*-pEGA block copolymer. Linear evolution of molecular weights with conversion and narrow dispersities (*Đ* = 1.16) obtained via GPC confirm a controlled polymerization. The calculated molecular weight from NMR conversion data is shown for comparison.

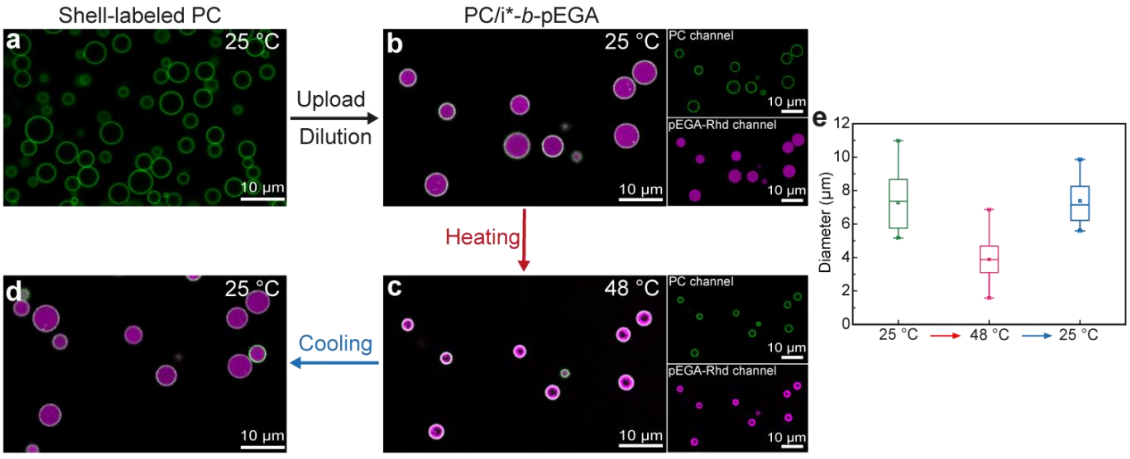

Figure S3.3. Reversible compartment formation within PCs. (a–d) Loading of i*-*b*-pEGA hybrid into PCs, and reversibility of phase separation of i*-*b*-pEGA within PCs during temperature ramp. **(e)** Diameter decrease of PC/i*-*b*-pEGA at 48 °C compared with 25 °C. The square and line inside the box correspond to the mean and median line of the PC population. The box represents a five-number summary of the PC data set, extending from the first quartile to the third quartile. Error bars are the standard deviation of ca. 15 PC/i*-*b*-pEGA counts.

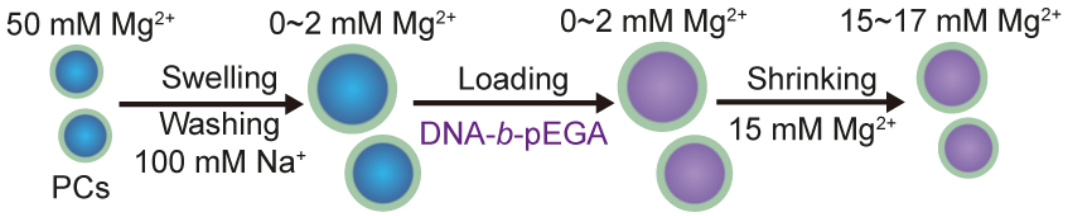

Figure S3.4. Schematic Loading Process. The PCs were washed with 100 mM Na^+ TE buffer to open the pores of the shell for better encapsulation of i*-*b*-pEGA. Subsequently, the concentration of Mg^{2+} was adjusted to 15 mM to stabilize the PCs.

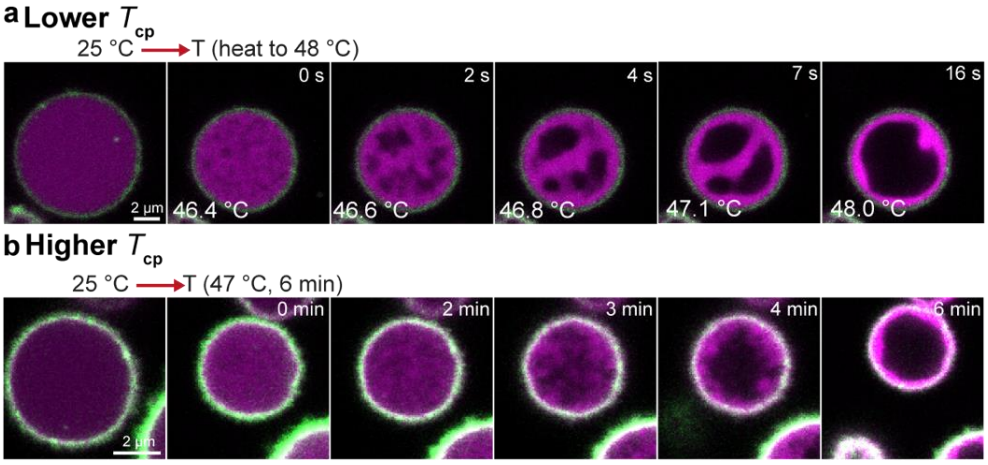

Figure S3.5. Robustness of the phase separation: Slight fluctuations in the exact transition temperature occur. We show two examples: **(a)** Temperature ramp to 48 °C for 1 min for a sample with a slightly lower transition temperature. **(b)** Temperature ramp to 47 °C, and staying at 47 °C for 6 min for a sample with a slightly higher transition temperature. Increasing the heating temperature or extending the incubation time at a lower temperature lead to the same structure formation and to the same final structure.

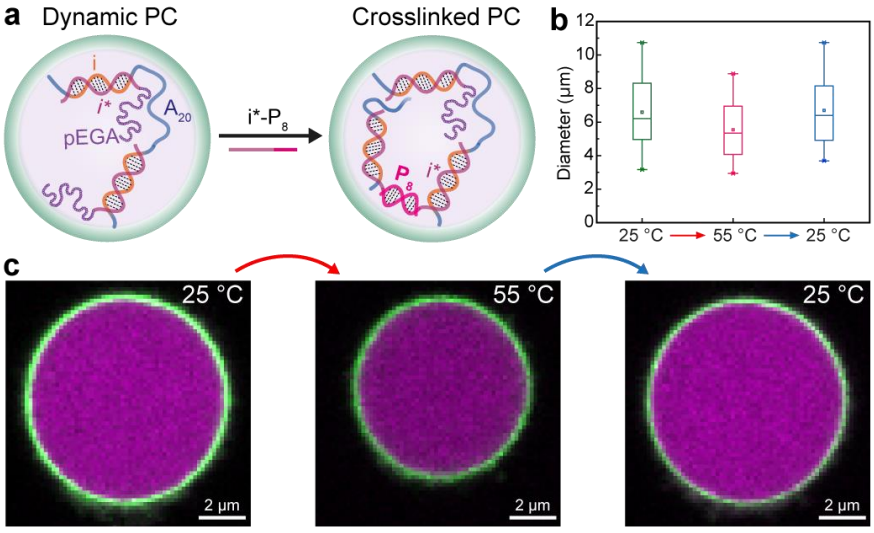

Figure S3.6. Crosslinking PCs by the introduction of palindrome crosslinker i*-P_8 at a ratio of i*-P_8/i*-*b*-pEGA of 1:9**. (a)** Scheme. **(b)** Slight diameter decrease of crosslinked-PC/i*-*b*-pEGA at 55 °C compared with 25 °C. The square and line inside the box correspond to the mean and median line of the crosslinked-PC population. The box represents a five-number summary of the crosslinked-PC data set, extending from the first quartile to the third quartile. Error bars are the standard deviation of ca. 15 crosslinked-PC counts. **(c)** Reversible heat triggered shrinkage (15 mM Mg^{2+}).

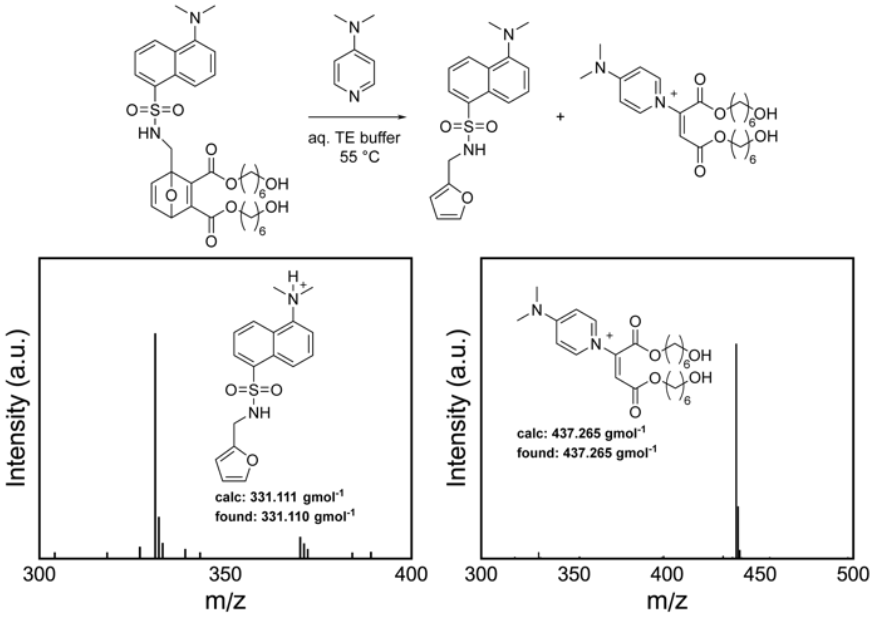

Figure S3.7. Uncaging reaction within PC/i*-*b*-pEGA and ESI-MS data of obtained products.

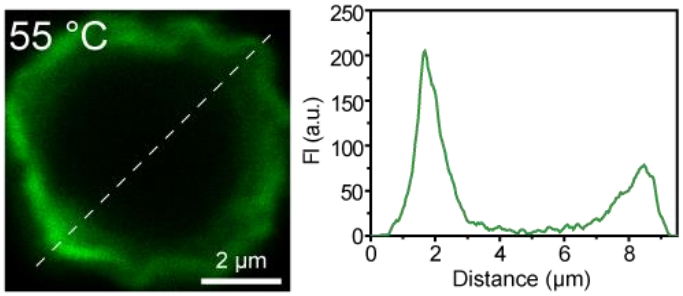

Figure S3.8. Uncaging reaction within pristine PCs. The uncaging reaction of Figure 3.3e does not take place inside pristine PCs without i*-*b*-pEGA. No blue fluorescence appears.

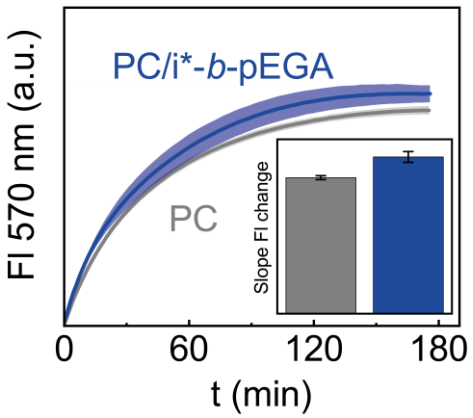

Figure S3.9. Time-dependent fluorescence of the reaction within PC/i*-*b*-pEGA hybrids vs. pristine PCs at 25 °C. Inset: Slope of the fluorescence increase by linear fitting during the first five minutes.

3.5 References

1. Buddingh, B. C.; van Hest, J. C. M. Artificial Cells: Synthetic Compartments with Life-like Functionality and Adaptivity. *Acc. Chem. Res.* **50**, 769-777 (2017).
2. Zhang, Y.; Chen, Y.; Yang, X.; He, X.; Li, M.; Liu, S.; Wang, K.; Liu, J.; Mann, S. Giant Coacervate Vesicles As an Integrated Approach to Cytomimetic Modeling. *J. Am. Chem. Soc.* **143**, 2866-2874 (2021).
3. Martin, N.; Tian, L.; Spencer, D.; Coutable-Pennarun, A.; Anderson, J. L. R.; Mann, S. Photoswitchable Phase Separation and Oligonucleotide Trafficking in DNA Coacervate Microdroplets. *Angew. Chem. Int. Ed.* **58**, 14594-14598 (2019).
4. Chen, X.; Wang, Y.; Dai, X.; Ding, L.; Chen, J.; Yao, G.; Liu, X.; Luo, S.; Shi, J.; Wang, L.; Nechushtai, R.; Pikarsky, E.; Willner, I.; Fan, C.; Li, J. Single-Stranded DNA-Encoded Gold Nanoparticle Clusters as Programmable Enzyme Equivalents. *J. Am. Chem. Soc.* **144**, 6311-6320 (2022).
5. Lu, T.; Spruijt, E. Multiphase Complex Coacervate Droplets. *J. Am. Chem. Soc.* **142**, 2905-2914 (2020).
6. Abbas, M.; Lipinski, W. P.; Wang, J.; Spruijt, E. Peptide-based coacervates as biomimetic protocells. *Chem. Soc. Rev.* **50**, 3690-3705 (2021).
7. Gao, N.; Mann, S. Membranized Coacervate Microdroplets: from Versatile Protocell Models to Cytomimetic Materials. *Acc. Chem. Res.* **56**, 297-307 (2023).
8. Leathers, A.; Walczak, M.; Brady, R. A.; Al Samad, A.; Kotar, J.; Booth, M. J.; Cicuta, P.; Di Michele, L. Reaction-Diffusion Patterning of DNA-Based Artificial Cells. *J. Am. Chem. Soc.* **144**, 17468-17476 (2022).
9. Sato, Y.; Takinoue, M. Capsule-like DNA Hydrogels with Patterns Formed by Lateral Phase Separation of DNA Nanostructures. *JACS Au* **2**, 159-168 (2022).
10. Zhao, Q. H.; Cao, F. H.; Luo, Z. H.; Huck, W. T. S.; Deng, N. N. Photoswitchable Molecular Communication between Programmable DNA-Based Artificial Membraneless Organelles. *Angew. Chem. Int. Ed.* **61**, e202117500 (2022).
11. Merindol, R.; Loescher, S.; Samanta, A.; Walther, A. Pathway-controlled formation of mesostructured all-DNA colloids and superstructures. *Nat. Nanotechnol.* **13**, 730-738 (2018).
12. Samanta, A.; Horner, M.; Liu, W.; Weber, W.; Walther, A. Signal-processing and adaptive prototissue formation in metabolic DNA protocells. *Nat. Commun.* **13**, 3968 (2022).
13. Ludwanowski, S.; Samanta, A.; Loescher, S.; Barner-Kowollik, C.; Walther, A. A Modular Fluorescent Probe for Viscosity and Polarity Sensing in DNA Hybrid Mesostructures. *Adv. Sci.* **8**, 2003740 (2021).
14. Samanta, A.; Sabatino, V.; Ward, T. R.; Walther, A. Functional and morphological adaptation in DNA protocells via signal processing prompted by artificial metalloenzymes. *Nat. Nanotechnol.* **15**, 914-921 (2020).
15. Alberti, S.; Gladfelter, A.; Mittag, T. Considerations and Challenges in Studying Liquid-Liquid Phase Separation and Biomolecular Condensates. *Cell* **176**, 419-434 (2019).
16. Capasso Palmiero, U.; Paganini, C.; Kopp, M. R. G.; Linsenmeier, M.; Kuffner, A. M.; Arosio, P. Programmable Zwitterionic Droplets as Biomolecular Sorters and Model of Membraneless Organelles. *Adv. Mater.* **34**, e2104837 (2022).
17. Deng, J.; Walther, A. Programmable and Chemically Fueled DNA Coacervates by Transient Liquid-Liquid Phase Separation. *Chem* **6**, 3329-3343 (2020).
18. Brangwynne, Clifford P.; Tompa, P.; Pappu, Rohit V. Polymer physics of intracellular phase transitions. *Nat. Phys.* **11**, 899-904 (2015).
19. Wang, B.; Maxwell, B. A.; Joo, J. H.; Gwon, Y.; Messing, J.; Mishra, A.; Shaw, T. I.; Ward, A. L.; Quan, H.; Sakurada, S. M.; Pruett-Miller, S. M.; Bertorini, T.; Vogel, P.; Kim, H. J.; Peng, J.; Taylor, J. P.; Kundu, M. ULK1 and ULK2 Regulate Stress Granule Disassembly Through Phosphorylation and Activation of VCP/p97. *Mol. Cell* **74**, 742-757 (2019).
20. Gwon, Y.; Maxwell, B. A.; Kolaitis, R. M.; Zhang, P.; Kim, H. J.; Taylor, J. P. Ubiquitination of G3BP1 mediates stress granule disassembly in a context-specific manner. *Science* **372**, eabf6548 (2021).
21. An, H.; de Meritens, C. R.; Shelkovnikova, T. A. Connecting the "dots": RNP granule network in health and disease. *Biochim. Biophys. Acta. Mol. Cell. Res.* **1868**, 119058 (2021).
22. Banani, S. F.; Lee, H. O.; Hyman, A. A.; Rosen, M. K. Biomolecular condensates: organizers of cellular biochemistry. *Nat. Rev. Mol. Cell. Biol.* **18**, 285-298 (2017).
23. Tanaka, H. Viscoelastic phase separation in biological cells. *Commun. Phys.* **5**, 167 (2022).

24. Liu, X.; Xiong, Y.; Zhang, C.; Lai, R.; Liu, H.; Peng, R.; Fu, T.; Liu, Q.; Fang, X.; Mann, S.; Tan, W. G-Quadruplex-Induced Liquid-Liquid Phase Separation in Biomimetic Protocells. *J. Am. Chem. Soc.* **143**, 11036-11043 (2021).
25. Jones, G. R.; Whitfield, R.; Anastasaki, A.; Haddleton, D. M. Aqueous Copper(II) Photoinduced Polymerization of Acrylates: Low Copper Concentration and the Importance of Sodium Halide Salts. *J. Am. Chem. Soc.* **138**, 7346-7352 (2016).
26. Vancoillie, G.; Van Guyse, J. F. R.; Voorhaar, L.; Maji, S.; Frank, D.; Holder, E.; Hoogenboom, R. Understanding the effect of monomer structure of oligoethylene glycol acrylate copolymers on their thermoresponsive behavior for the development of polymeric sensors. *Polym. Chem.* **10**, 5778-5789 (2019).
27. Heckel, J.; Batti, F.; Mathers, R. T.; Walther, A. Spinodal decomposition of chemically fueled polymer solutions. *Soft Matter* **17**, 5401-5409 (2021).
28. Andre, A. A. M.; Spruijt, E. Liquid-Liquid Phase Separation in Crowded Environments. *Int. J. Mol. Sci.* **21**, 5908 (2020).
29. Liu, W.; Samanta, A.; Deng, J.; Akintayo, C. O.; Walther, A. Mechanistic Insights into the Phase Separation Behavior and Pathway-Directed Information Exchange in all-DNA Droplets. *Angew. Chem. Int. Ed.* **61**, e202208951 (2022).
30. Glickman, B. W.; Ripley, L. S. Structural intermediates of deletion mutagenesis: A role for palindromic DNA. *Proc. Nati. Acad. Sci.* **81**, 512-516 (1984).
31. Dorh, N.; Zhu, S.; Dhungana, K. B.; Pati, R.; Luo, F. T.; Liu, H.; Tiwari, A. BODIPY-Based Fluorescent Probes for Sensing Protein Surface-Hydrophobicity. *Sci. Rep.* **5**, 18337 (2015).
32. Fell, J. S.; Lopez, S. A.; Higginson, C. J.; Finn, M. G.; Houk, K. N. Theoretical Analysis of the Retro-Diels-Alder Reactivity of Oxanorbornadiene Thiol and Amine Adducts. *Org. Lett.* **19**, 4504-4507 (2017).

4 A Facile DNA Coacervate Platform for Engineering Wetting, Engulfment, Fusion and Transient Behavior

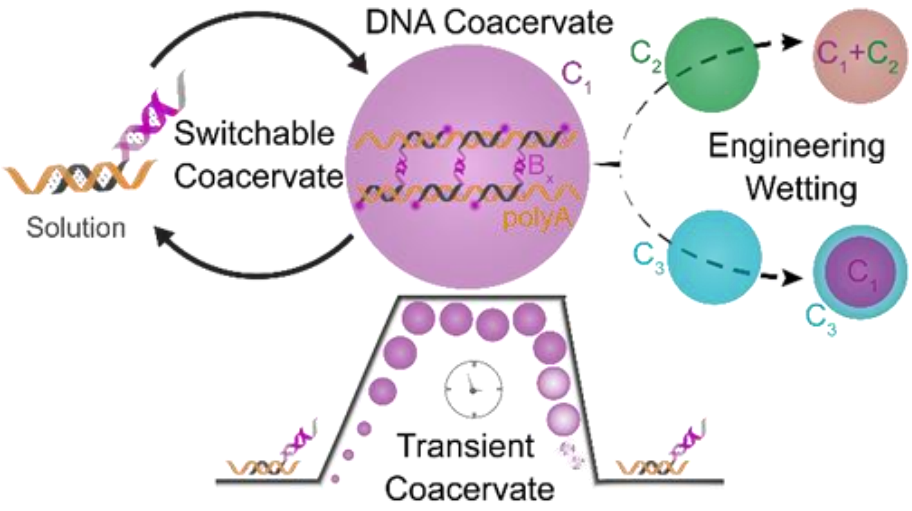

Preliminary note: *This chapter is based on the article published in Commun. Chem. 7, 100 (2024). Minor changes have been made concerning formatting style.*

Abstract: Biomolecular coacervates are emerging models to understand biological systems and important building blocks for designer applications. DNA can be used to build up programmable coacervates, but often the processes and building blocks to make those are only available to specialists. Here, we report a simple approach for the formation of dynamic, multivalency-driven coacervates using long single-stranded DNA homopolymer in combination with a series of palindromic binders to serve as a synthetic coacervate droplet. We reveal details on how the length and sequence of the multivalent binders influence coacervate formation, how to introduce switching and autonomous behavior in reaction circuits, as well as how to engineer wetting, engulfment, and fusion in multi-coacervate system. Our simple-to-use model DNA coacervates enhance the understanding of coacervate dynamics, fusion, phase transition mechanisms, and wetting behavior between coacervates, forming a solid foundation for the development of innovative synthetic and programmable coacervates for fundamental studies and applications.

4.1 Introduction

Membraneless organelles (MLOs), also known as biomolecular condensates, form through liquid-liquid phase separation (LLPS) within cells and have been shown to play a crucial role in regulating biological functions.[1-3] Unlike traditional membrane-bound organelles, MLOs such as nucleoli, stress granules, and P-bodies function in the absence of a surrounding lipid bilayer. They are often formed by proteins or complexes of proteins and nucleic acids.[4-6] The unique properties of MLOs are predominantly driven by an array of weak interactions, including protein–protein, protein–RNA, electrostatic, and hydrophobic interactions, culminating in dynamic liquid properties.[7-9] These liquid characteristics influence the spatial organization, phase transition, and molecular interactions within cells, thereby regulating diverse cellular activities including gene expression, cell adhesion, and cargo recruitment.[10-12]

Inspired by natural LLPS-driven organelles, the fabrication of bioinspired LLPS systems, consisting of DNA, RNA, and proteins, has gained much ground in order to better understand biological systems using defined model systems, as well as for generating functional materials relevant to the molecular systems engineering world.[13-17] Despite the progress, many open questions remain, for instance, regarding the interactions between coacervates of different natures and of coacervates with soft interfaces. Interesting progress has also been made with respect to the uptake of

coacervates into liposomes or cells or, very recently, regarding LLPS in fibrillar environments.[18-20]

DNA is an appealing building block to build up coacervates due to the programmable nature of interactions.[21] Various strategies have been employed to construct DNA coacervates and droplets, including the use of hybridization-mediated assembly of DNA nanostars or temperature-induced phase segregation and trapping of DNA.[16, 22-25] These all-DNA artificial cell models can exhibit liquid-like behavior, beneficial to study adhesion, fission, fusion, and wetting.[26-32] For instance, Takinoue and co-workers investigated the impact of DNA sequences on the fusion dynamics of liquid-like droplets at elevated temperatures (above 43 °C).[28] However, many of the approaches require specialist knowledge for DNA assembly techniques and well-designed annealing protocols, whereas simple mix-and-use protocols at one temperature would be very desirable.

In this study, we report an easy-to-use platform for all-DNA coacervates utilizing single-stranded DNA (ssDNA) components and multivalency-driven LLPS at physiological temperature (Figure 4.1). We show that a series of palindromic domains can be flexibly hybridized to long ssDNA homopolymers composed solely of adenine nucleotides (polyA) to trigger coacervate formation, and to study dynamics as a function of the type of palindromic binder. Through the integration of DNA or RNA strands, we establish switchable systems for the controlled assembly and disassembly of coacervates. This advancement enables the realization of a transient, autonomous coacervate system.[33] Furthermore, the selective exploitation of the distinctive dynamic properties conferred by various palindromic domains allows to engineer multiphase structures through tailored wetting mechanisms. We anticipate that the facile formation mechanism and the flexible design of different dynamic behaviors of these DNA coacervates will pave the way for the engineering of functional DNA-based coacervates, with a great potential to be followed up by non-experts.

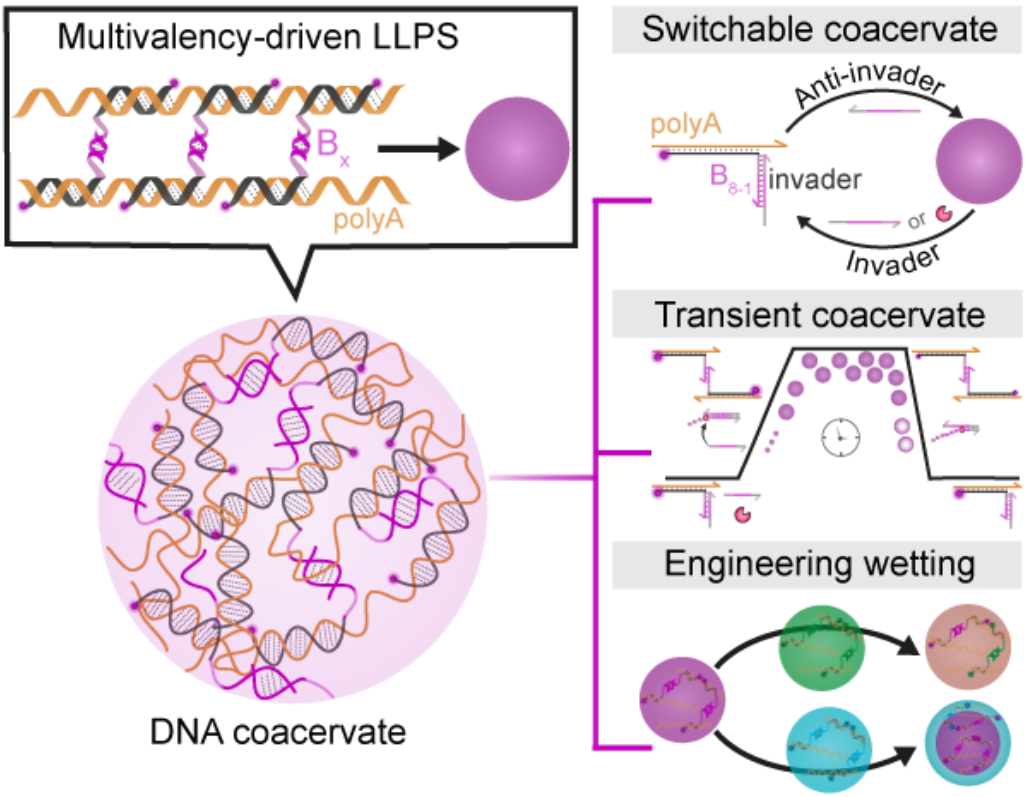

Figure 4.1. Multivalency-driven all-DNA coacervates: coacervate preparation, switching, autonomous behavior and engineered wetting for multi-phase structures. DNA coacervates are prepared via multivalency-driven liquid-liquid phase separation (LLPS) between a ssDNA polymer (polyA) and shorter self-complimentary binders (B_x). The introduction of DNA or RNA invader triggers the formation of switchable and transient coacervates. Using two distinct coacervates with different palindromic domains allows controlling multiphase structures through engineering wetting.

4.2 Results and Discussion

4.2.1 Formation of Multivalency-Driven Coacervates

Our strategy for the fabrication of all-DNA coacervates employs a straightforward multivalency-driven LLPS approach based on the combination of a ssDNA homopolymer (polyA; A = adenine) and shorter binders (B_x) containing palindromic domains and a T_{30} (T = thymine) domain for hybridization to the polyA backbone (Figure 4.2a). The DNA homopolymer A_{1500} was synthesized using terminal deoxynucleotidyl transferase (TdT)-catalyzed polymerization to feature 1500 repeating units.[34, 35] Similar polyA are however also available commercially. The binders, B_x, typically feature four components: (1) the complementary segment T_{30} ensuring hybridization to the polymer A_{1500} (melting temperature, T_m (A_{30}/T_{30}) = 62.8 °C at 10 mM Mg^{2+}, 50 mM Na^+, by IDT), (2) an intermediate spacer providing both flexibility and a toehold (S_7), (3) the palindromic domain, P_x, facilitating multivalent interactions, and (4) a dye label. These structures are hence composed of T_{30}-S_7-P_x

(or shorter B_x), whereby x signifies the length of the palindrome and thus the strength of the interaction. The strength of the palindrome also depends on the GC content. The table listing the T_m in Figure 4.2b gives a rough correlation of the binder strength.

We designed eight distinct binder strands (T_{30}-S_7-P_x = B_x), each characterized by a unique sequence and varying length of the palindromic domain (Figure 4.2b). Through this approach, we aimed to understand the influence of these two factors (GC content and palindromic length) on the formation and dynamics of spherical coacervates. Coacervate systems were typically assembled by mixing B_x with A_{1500} in a molar ratio of 25:1 at 1.5 µM T_{30}-S_7-P_x and 0.06 µM A_{1500} at 37 °C in a buffer containing 10 mM Mg^{2+} and 50 mM K^+ (pH = 7.9). Note that 0.06 µM A_{1500} is equivalent to 3 µM A_{30} and hence the B_x segments can occupy 50% of all A repeat units in A_{1500}. Confocal laser scanning microscopy (CLSM) shows nicely spherical coacervates for five of the eight systems (Figure 4.2c, d). The system featuring the shortest P_x, comprised of merely 4 nucleotides (nt) and a low GC content ($P_{4\text{-}1}$), presents no distinguishable structural formation. Systems with the longest P_x, containing 10 or 12 nt (P_{10}, P_{12}), display excessive aggregation into non-spherical structures. This behavior roughly correlates with the T_m of the individual palindromes, but the multivalent strengthening needs to be considered as well.

The absence of coacervate formation in the A_{1500}/$P_{4\text{-}1}$ system ($T_{m,P4\text{-}1}$ = 0 °C) arises from the feeble multivalent binding due to the low GC content. Even though the other shorter P_x systems (x = 4-2, 6, 8-1, 8-2, 8-3) have also calculated T_m < 28 °C, hence still significantly lower than the system temperature of 37 °C, they still lead to the formation of well-defined spherical coacervates due to efficient multivalency effects. This indicates a dynamic nature and binding/unbinding dynamics. In contrast, the aggregation in systems incorporating the longest P_x strands (x = 10, 12) with T_m = 38.7 °C and 41.9 °C can be attributed to the excessively rigid multivalent interactions without significant internal dynamics for rearrangement into spherical structures. Hence, for the fabrication of spherical all-DNA coacervate via multivalency-driven LLPS, the optimum length of P_x containing four GC bases lies in the approximate range of 4 to 8 nt in total (Figure 4.2c). This balances phase separation and sufficient rebinding dynamics on a multivalency level, yielding the desired spherical structural output.

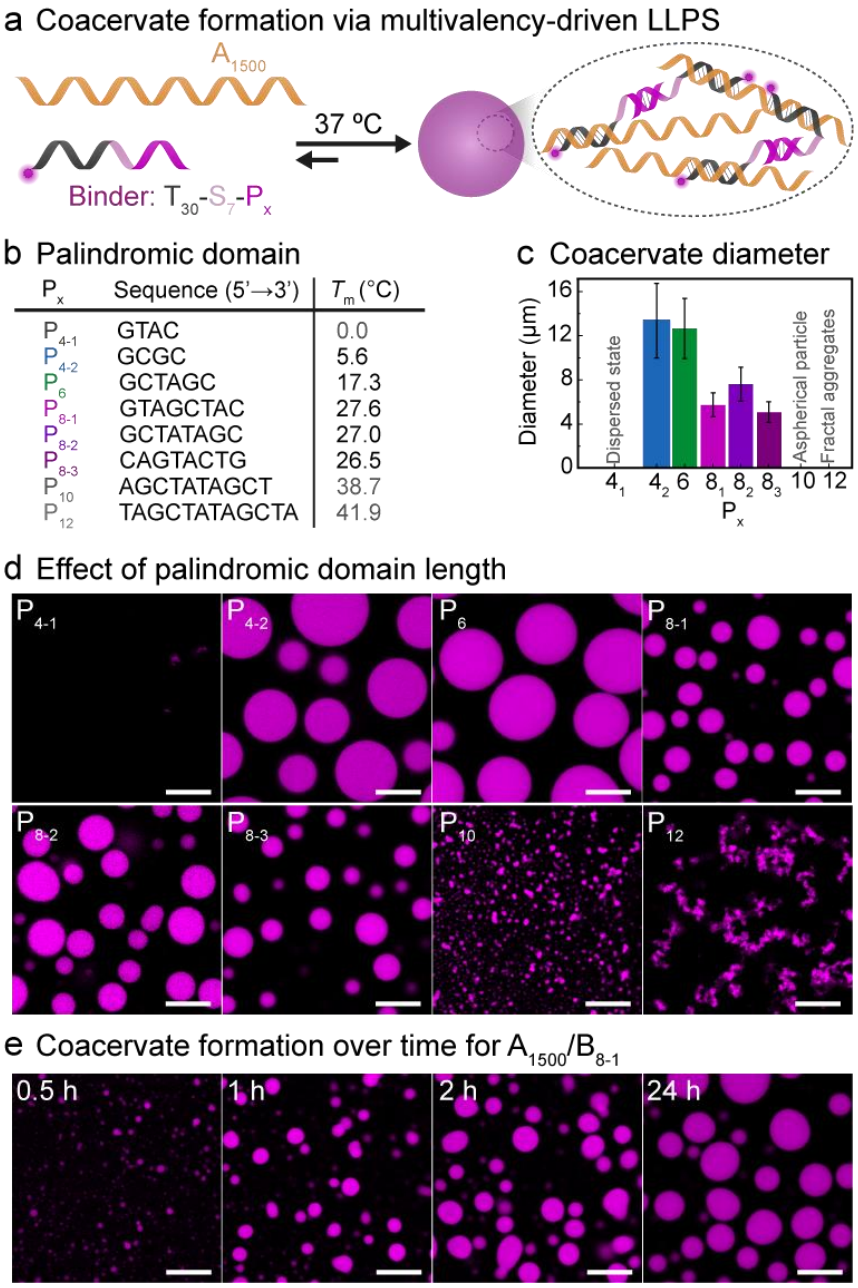

Figure 4.2. Mechanism of the formation of multivalency-driven coacervates and the palindromic domain effect on the formation. (a) Multivalency-driven coacervates by a long ssDNA (A_{1500}) mixed with short binder ssDNA consisting of a complementary strand T_{30}, a spacer S_7 and a palindromic multivalency domain P_x. **(b)** Sequences and melting temperatures (T_m) of the palindromic domains at 10 mM Mg^{2+}. **(c)** Size distribution of coacervates in systems containing 0.06 μM A_{1500} and 1.5 μM binder at 37 °C after a 4 h reaction period with various palindromic domains. Error bars correspond to standard deviations of ca. 150 coacervates. **(d)** CLSM images of systems containing 0.06 μM A_{1500} and 1.5 μM binder at 37 °C after a 4 h reaction period with different palindromic domains. **(e)** Time-dependent CLSM images of A_{1500}/B_{8-1}. The fluorescent labels are on the B_x. The experiments were conducted at 37 °C with gentle rotation at 80 rpm. Scale bars: 10 μm.

We monitored a mixture of A_{1500} and B_{8-1} at 37 °C for visual tracking of the coacervate formation. After 0.5 h, a population of small coacervates with an average diameter of 0.7 μm appears. These small coacervates rapidly coalesce, gradually increase in size, and transform into larger entities with an average diameter of ca. 2.8 μm within 1 h. In the following 30 h, these structures continue to progressively coalesce and evolve into

well-defined coacervates with ca. 8.8 µm diameter (Figure 4.2e and Figure S4.1). This coalescence and growth further highlight the dynamic behavior within the phase-separated coacervate state. Fluorescence recovery after photobleaching (FRAP) measurements reveal a partial, limited recovery within 1.5 h post bleaching for the three coacervates with 8 nt in the palindrome. At the same time, partial fusion events can be clearly observed (Figure S4.2; arrows therein highlight fusion events; Figure S4.3 shows the minor effect of palindromic domains with different lengths = 4, 6, 8 nt). Hence, these coacervates are sufficiently dynamic to allow for fusion. Most interestingly, the coacervates formed by $B_{8\text{-}2}$ show the quickest recovery at the coacervate surface. Hence, despite the strong similarities in the different binders of the $B_{8\text{-}y}$ series, subtle differences in behavior can occur.

4.2.2 DNA- and RNA-Triggered Coacervate Dynamics: Switchable and Transient Systems

In the above investigation, we discussed the mechanism and conditions guiding the formation of our multivalency-driven coacervates. To achieve switchable and transient coacervate systems, we employed tools from DNA and RNA nanoscience to coacervates formed with the binder $B_{8\text{-}1}$. For the establishment of switchable coacervates, we introduced a DNA invader consisting of a domain complementary to the S_7-$P_{8\text{-}1}$ segment of the binder, along with an additional dangling overhang acting as a toehold for subsequent reactions (Figure 4.3a). The addition of this invader to already formed coacervates disengages the multivalent interactions via strand displacement of the P_x/P_x palindrome. CLSM images demonstrate the disappearance of the coacervates upon the addition of the DNA invader in less than 10 minutes (Figure 4.3b). Furthermore, the introduction of an additional DNA anti-invader, which can hybridize with the DNA invader at its dangling overhang, triggers displacement of the invader and the reengagement of the palindromic hybridization site followed by reassembly of the coacervate. This process enables simple isothermal switching of the DNA coacervates.

This concept can be extended to an RNA invader capable of complementary interaction with the S_7-$P_{8\text{-}1}$ segment of the binder (Figure 4.3c,d; Figure S4.4). When RNA invaders are introduced, the coacervates disassemble rapidly in less than 10 minutes. Coacervate reassembly occurs upon addition of RNase H, which specifically degrades RNA hybridized with DNA. A toehold is no longer needed as for the DNA

invader. The use of an enzyme allows, in principle, to fine-tune the kinetics of the re-engagement by simply changing its concentration. Furthermore, the switching process can be inverted by introducing an RNA anti-invader that removes a blocker strand from the B_x domain to trigger assembly. Subsequent addition of RNase H thereafter affords disassembly of the coacervate systems by degradation of the RNA anti-invader and subsequent reblocking of the B_x with the newly liberated original ssDNA block strand (Figure 4.3e,f).

Building upon the RNA-triggered switchable coacervate systems, we asked whether autonomous and transient coacervate dissolution as well as coacervate formation would be possible by addition of RNA trigger strands into RNase H-loaded systems.[36-38] Figure 4.3g−k displays transient coacervate disassembly. Coacervates formed by A_{1500} and $B_{8\text{-}1}$ were first generated, and then combined with an excess of RNA invader (10 eq. of binder) at a low concentration of RNase H (0.1 U μL^{-1}). Before introducing the RNA invader, CLSM images show the initially formed coacervates (Figure 4.3k). The subsequent simultaneous addition of RNA invader and RNase H set off an autonomous and dynamic transformation between coacervate and solution states. Within 10 min, the coacervates disassemble into a fully homogeneous solution due to rapid hybridization of $B_{8\text{-}1}$ and RNA invader, which blocks multivalent interactions. After 0.5 h, some minor coacervates are observed because of the gradual degradation of the RNA invader by the already present RNase H. As RNA degradation continues, the reformation of well-defined coacervates occurs (Figure 4.3h,k). Importantly, the reassembly time (defined as the point where coacervates reappear in CLSM) of these transient coacervates can be adjusted within a range of 0.3 to 2.9 h by either augmenting the quantity of RNA invader or reducing the concentration of RNase H (Figure 4.3i,j; Figure S4.5 and S4.6).

The opposite pathway, i.e., transient coacervates, can be accomplished by integrating the A_{1500}/$B_{8\text{-}1}$/DNA-invader complex with excess of RNA anti-invader and a low concentration of RNase H (Figure 4.3l). The RNA anti-invader quickly removes the DNA strand blocking the multivalent interaction, and thereby activated coacervation. By balancing the competition between anti-invader/invader hybridization and anti-invader degradation by RNase H, and allowing the necessary time for coacervate formation, well-defined coacervate structures are observed after 1.5 h (Figure 4.3m and Figure S4.7). After 3 h, these coacervates gradually disappear.

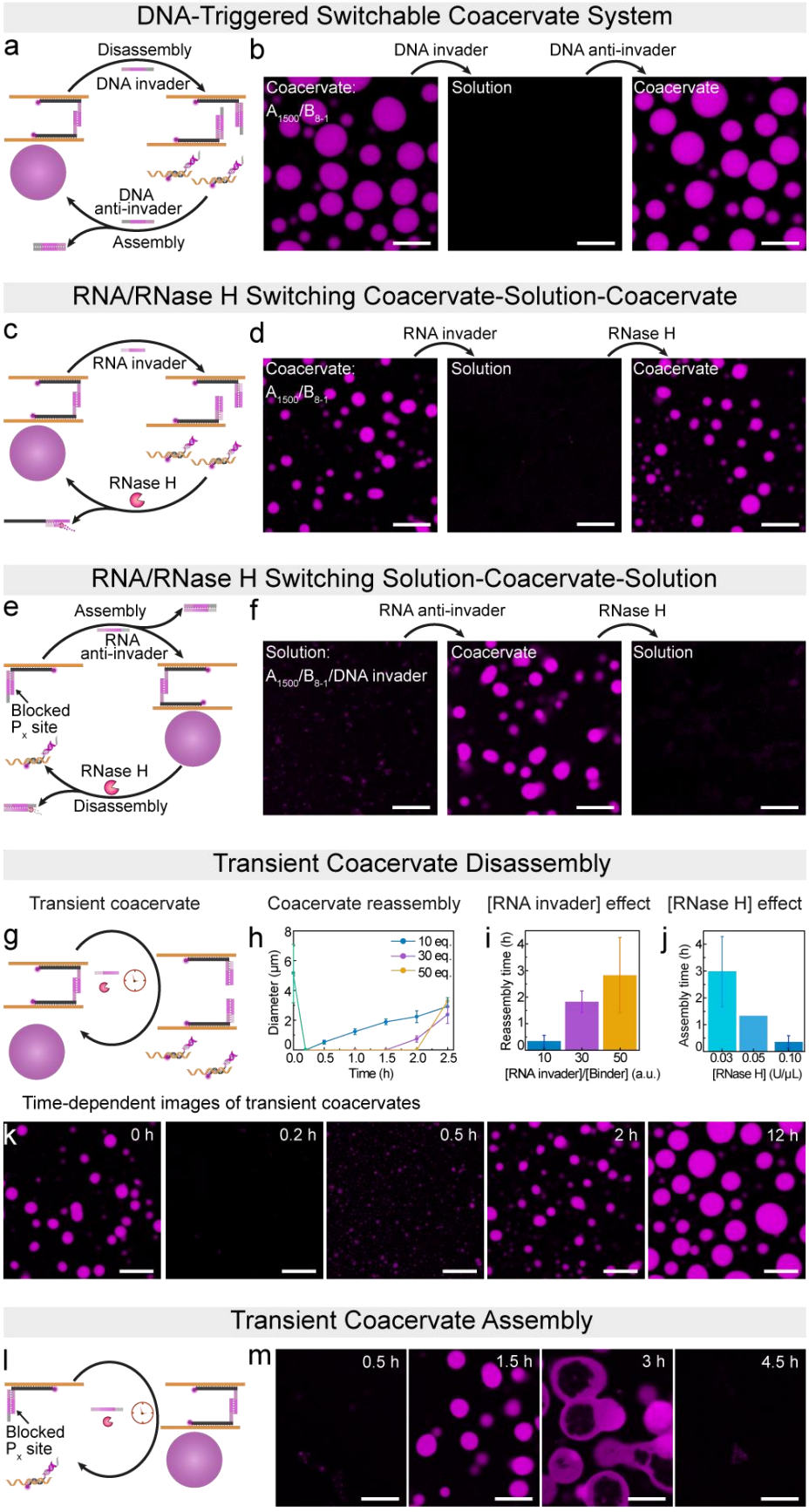

Figure 4.3. DNA- and RNA-triggered switchable coacervates and RNA-regulated transient coacervates. (a–b) Illustration and CLSM images of DNA-triggered switchable coacervate systems. 2.25 μM (1.5 eq.) of DNA invader was introduced to the coacervates formed from 0.06 μM A_{1500} and 1.5 μM (1.0 eq.) of $B_{8\text{-}1}$, resulting in the

disassembly of the coacervates. Subsequently, the addition of 3 μM (2.0 eq.) of DNA anti-invader caused the reformation of coacervates. **(c–d)** Illustration and CLSM images of RNA-triggered switching between coacervate and solution states. 4.5 μM (3 eq.) of RNA invader was introduced to the coacervates formed from 0.06 μM A_{1500} and 1.5 μM (1.0 eq.) of $B_{8\text{-}1}$, resulting in the disassembly of the coacervates. Subsequently, the addition of 0.1 U μL^{-1} of RNase H triggered the assembly of coacervates. **(e–f)** Illustration and CLSM images of RNA-triggered switchable coacervate of solution-to-coacervate-to-solution. 15 μM (10 eq.) of RNA anti-invader was introduced into the complex comprising 0.06 μM A_{1500}, 1.5 μM $B_{8\text{-}1}$, and 2.25 μM DNA invader, leading to the assembly of the coacervates. Subsequently, the addition of 0.1 U μL^{-1} of RNase H caused the coacervates to disassemble into a homogeneous solution. A few tiny objects in the initial state may be due to incomplete dissolution of the dye-bearing strand adsorbed at the microscopy chamber. **(g–k)** RNA-regulated transient coacervate disassembly with the introduction of RNA invader and RNase H: **(g)** Schematic illustration. **(h)** Time-dependent plot of the transient coacervates with tunable reassembly times by varying the concentration of RNA invaders. The green line indicates start from a similar population of coacervates. Error bars are the standard deviation of ca. 20 droplet counts. **(i)** Controlled reassembly times via the concentration ratios of RNA invader/binder. Error bars correspond to standard deviations from duplicates. **(j)** Controlled reassembly times via the RNase H concentrations. Error bars correspond to standard deviations from duplicates. **(k)** Time-dependent CLSM images of transient coacervates with 15 μM (10 eq.) RNA invader and 0.1 U μL^{-1} RNase H. **(l–m)** RNA-regulated transient coacervate assembly with the introduction of RNA anti-invader and RNase H: **(l)** Schematic illustration. **(m)** Time-dependent CLSM images of transient coacervates with 45 μM (30 eq.) RNA anti-invader and 0.1 U μL^{-1} RNase H. The experiments were conducted at 37 °C with gentle rotation at 80 rpm. Scale bars: 10 μm.

Strikingly, hollow capsules appear, which indicates entrapment of the RNase H due to affinity to RNA (and potentially DNA) inside the coacervates and degradation from the inside. The relatively high stability of the vacuoles without diffusion to the surface likely originates from the viscoelastic character of the coacervates with limited dynamics (FRAP in Figure S4.2). Such vacuole formation has been observed earlier for enzymatic degradation of DNA nanostar condensates when adding a restriction enzyme from the outside and was associated with the dynamics of the condensate and enzyme migration dynamics.[39] Our mechanism is however different as the restriction enzyme is present from the start and entrapped, and does not need to diffuse into the condensate. Both approaches highlight the development of RNA-mediated autonomous transient coacervate systems that function by simultaneously utilizing RNA strands and the endoribonuclease. These systems will be used below for slow activation of binary coacervate systems.

4.2.3 Engineering Wetting Between Coacervates

After understanding how the combination of A_{1500} and B_x can lead to the formation of dynamic and switchable coacervates, we hypothesized that these simple-to-prepare coacervates can be used to engineer coacervate mixtures and interactions using various binders. To this end, we prepared three distinct coacervates: C_1 in magenta, C_2 in green, and C_3 in cyan, using different binders $B_{8\text{-}1}$, $B_{8\text{-}2}$, and $B_{8\text{-}3}$, respectively, wherein each binder is associated with a specific and selectively binding palindrome sequence ($P_{8\text{-}1}$, $P_{8\text{-}2}$, and $P_{8\text{-}3}$, as shown in Figure 4.2b,c and Figure 4.4a). After initial formation of the individual coacervates (time = 1 h; 37 °C), we combined two of them

to understand whether they remain segregated or potentially fuse despite being built by different palindromic binders.

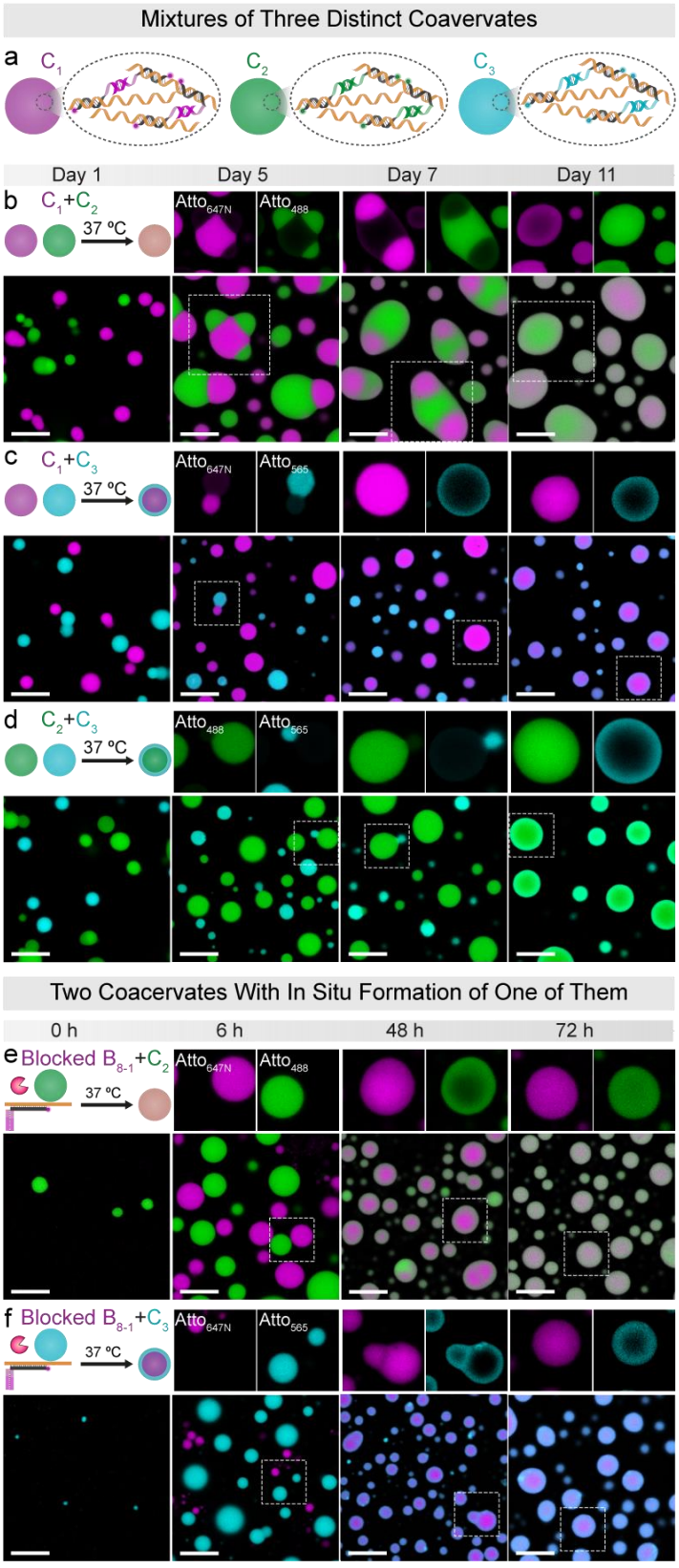

Figure 4.4. Engineering wetting between coacervates formed with diverse palindromic sequences at 37 °C. The coacervates were prepared using a mixture containing a final concentration of 0.06 µM of A_{1500} and 1.5 µM of

the respective B_x. **(a)** Illustration of three distinct coacervate structures (C_1 in magenta, C_2 in green, and C_3 in cyan) synthesized from different binders ($Atto_{647N}$-$B_{8\text{-}1}$, $Atto_{488}$-$B_{8\text{-}2}$, and $Atto_{565}$-$B_{8\text{-}3}$) with various palindromic sequences ($P_{8\text{-}1}$, $P_{8\text{-}2}$, and $P_{8\text{-}3}$, as showed in Figure 4.2b,c). The experiments were performed at 37 °C with gentle rotation at 80 rpm, unless otherwise specified. **(b)** Wetting behavior between distinct C_1 and C_2, leading to the formation of mixed coacervates. **(c)** Wetting behavior between C_1 and C_3, resulting in the formation of core-shell structures. **(d)** Wetting behavior between C_2 and C_3, contributing to the formation of core-shell structures. The experiments were carried out at 37 °C without rotation to minimize collisions. **(e)** Behavior during RNase H-initiated, slow coacervation of C_1 in a dispersion of preformed C_2. 0.1 U μL^{-1} RNase H and preformed C_2 were introduced into the complex comprising 0.06 µM A_{1500}, 1.5 µM of $B_{8\text{-}1}$, and 2.25 µM RNA invader. **(f)** Behavior during RNase H-initiated, slow coacervation of C_1 to preformed C_3. 0.1 U μL^{-1} RNase H and preformed C_3 were introduced into the complex comprising 0.06 µM A_{1500}, 1.5 µM of $B_{8\text{-}1}$, and 2.25 µM RNA invader**.** The experiments were conducted at 37 °C with gentle rotation at 80 rpm. Scale bars: 10 µm.

Following an 11-day incubation period at 37 °C, a rich diversity of morphologies emerges. In general, the process follows initial contact at early times, subsequent engulfment, formation of a preferred wetting layer, and ultimately complete mixing (Figure 4.4). The harmonization process occurs on different time scales for the different coacervate mixtures and is not complete for mixtures of C_1 (magenta)/C_3 (cyan) and of C_2 (green)/C_3 (cyan), for which distinct core-shell morphologies persist with slow homogenization even after 11 days. (Figure 4.4c,d), These observations are in line with the diminished dynamics of C_3 relative to C_1 and C_2 (Figure S4.2). The tendency to form the wetting layer on the surface follows $C_1 < C_2 < C_3$. It leaves to speculate that the small differences in palindrome binder – despite being very similar in structure and thermodynamics – leads to slightly different surface tensions. It is interesting to note that the most hydrophilic dye ($Atto_{488}$) located on C_2 (green) does not form the most effective surface wetting layer (Figure 4.4d). Concerning the gradual homogenization, control experiments by gel electrophoresis point to a gradual strand displacement within simplified model system of A_{37}/$B_{8\text{-}1}$ and $B_{8\text{-}2}$ (Figure S4.8), wherein the initially bound $B_{8\text{-}1}$ strand is undergoing slow exchange with $B_{8\text{-}2}$. This process may aid in compatibilization. Note that NUPACK simulations do not indicate cross-talk/off-target binding between the different $B_{8\text{-}x}$ binders down to a temperature of 5 °C.

To further investigate the emergence of wetting phenomena, we employed the autonomous formation of one coacervate system in presence of an already formed different coacervate. This connects to Figure 4.3c, where RNase H-mediated digestion of RNA was used to trigger coacervation. When using slow RNase H-mediated formation of C_1 in presence of already preformed C_2 (Figure 4.4e), the data shows homogeneous nucleation of distinct magenta C_1 structures in presence of preformed C_2. Heterogeneous nucleation is absent. Over time, these discrete coacervates form a unified coacervate. When slowly activating C_1 to preformed C_3 (Figure 4.4f), again

homogeneous nucleation takes place followed by formation of core-shell structures. Hence the morphological development is independent of the nucleation pathway and the temporal orchestration. No matter whether preformed coacervates are mixed, or whether one is grown slowly, similar fully mixed or core/shell structures appear. This points to a robustness of the process. Overall, this approach shows how to control diverse morphologies in the presence of two distinct coacervate systems, thereby not only achieving wetting control but also mimicking the formation processes and wetting behaviors of the biological organelles within cells.[29, 40-42]

Obviously, the wetting process between two preformed coacervates takes more than one week because of the slow mobility of the coacervates, as well as the very slow possible exchange of binder segments. To gain a better understanding of the wetting behavior and accelerate this process, we employed a so-called C_{31} system together with the C_1 coacervates (Figure 4.5). The C_{31} coacervate was engineered to contain mixtures of its original $B_{8\text{-}3}$ binder and either 25 or 50 mol% of the $B_{8\text{-}1}$ binder (Figure 4.5a). The latter serves to strengthen and accelerate interactions between the C_{31} and the C_1.

Upon mixing C_1 and C_{31} (Figure 4.5c,d), core-shell structures visually identical to the C_1/C_3 system are formed (Figure 4.4c and Figure 4.5b), but with different formation times, based on the ratio of $B_{8\text{-}3}$ to $B_{8\text{-}1}$. C_{31} with a $B_{8\text{-}3}$:$B_{8\text{-}1}$ ratio of 75%:25% leads to the observation of Janus-like structures within 1 day. Following this, multicompartment structures occur after 3 days, and the final core-shell structures emerge within 7 days (Figure 4.5c). Furthermore, changing the $B_{8\text{-}3}$:$B_{8\text{-}1}$ ratio to 50%:50% significantly enhances the wetting behavior, resulting in the emergence of the final core-shell structures within 3 days, instead of 7 days (Figure 4.5d). This phenomenon indicates that the wetting speed can be effectively modulated by tuning the multivalent interactions of the binders between two coacervates.

The wetting behavior of C_1 and C_{31} helps to understand the interaction in a mixture of pure, distinct C_1 and C_3. In the mixture of C_1 and C_3, as mentioned above, the unbound free A repeat units on A_{1500} within coacervates present opportunities for strand exchange between $B_{8\text{-}1}$ in the C_1 coacervate and $B_{8\text{-}3}$ in the C_3 coacervate (Figure 4.5e; Figure S4.8). This strand displacement process leads to an increased

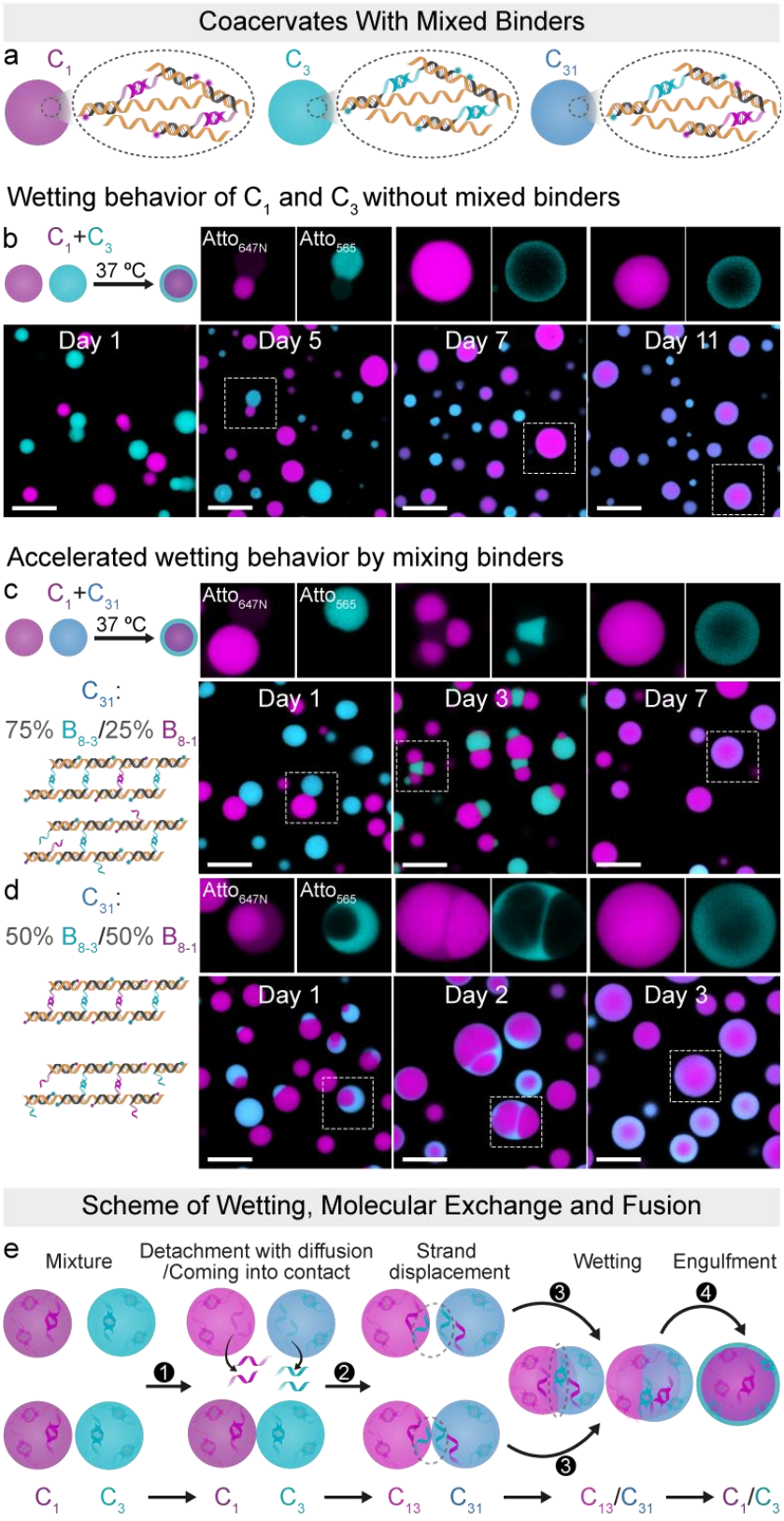

Figure 4.5. Engineering accelerated wetting between two coacervates and its mechanisms. Coacervates C_1 (or C_3) were formed using a mixture containing a final concentration of 0.06 μM of A_{1500} and 1.5 μM of either $B_{8\text{-}1}$ or $B_{8\text{-}3}$. Coacervates C_{31} were generated from 0.06 μM A_{1500} and a mixture totaling 1.5 μM of $B_{8\text{-}1}$ and $B_{8\text{-}3}$. **(a)** Illustration of three distinct coacervate structures (C_1 in magenta, C_3 in cyan, and C_{31} in dark cyan) synthesized using different binders ($B_{8\text{-}1}$, $B_{8\text{-}3}$, and a mixture of $B_{8\text{-}3}$ and $B_{8\text{-}1}$). The experiments were performed at 37 °C with gentle rotation at 80 rpm, unless otherwise specified. **(b)** Wetting behavior upon the combination of C_1 and C_3. **(c)** Accelerated wetting behavior upon the combination of C_1 and C_{31} by the introduction of $B_{8\text{-}1}$ in the C_{31} system at a

ratio of 75%:25% $B_{8\text{-}3}$:$B_{8\text{-}1}$ (1.125 µM of $B_{8\text{-}3}$ and 0.375 µM of $B_{8\text{-}1}$). **(d)** Accelerated wetting behavior upon the combination of C_1 and C_{31} by introducing $B_{8\text{-}1}$ in the C_{31} system at a ratio of 50%:50% $B_{8\text{-}3}$:$B_{8\text{-}1}$ (0.75 µM of $B_{8\text{-}3}$ and 0.75 µM of $B_{8\text{-}1}$). The experiments were conducted at 37 °C without rotation to minimize collisions. **(e)** Suggested mechanisms of coacervate fusion for C_1 and C_3. The molecular exchange between different-type coacervates occurs through either detachment of the binders and their diffusion or strand displacement. Scale bars: 10 µm.

presence of $B_{8\text{-}3}$ in C_1 as well as of $B_{8\text{-}1}$ in C_3 that enables multivalent interactions between the original C_1 and C_3 via wetting and engulfment. This strand displacement behavior can occur when the coacervates come into contact. Subsequently, the strand exchange enhances the emergence of complex structures through wetting, fusion, and engulfment. The process is sketched in Figure 4.5e. We hypothesize that strand exchange may also occur very slowly even when the coacervates are at a distance from each other through complete detachment of the binders and their diffusion (equilibrium dynamics of dsDNA). It is reasonable to assume that an elongation of the T_x segment in the binders would further limit the molecular exchange, and thus slow down or even prevent fusion.

4.3 Conclusions

In summary, we introduced a simple and versatile platform for programmable DNA coacervates. In contrast to many other DNA coacervate systems, this model system does not require much knowledge on the design of DNA nanostars, complicated synthesis or well-designed annealing protocols, but operates on a simple mix and use principle. Furthermore, due to the presence of a polymeric component (polyA), a different viscoelastic regime can be generated within the coacervates as compared to nanostar-based droplets, because polymer entanglements can be present for long polyA, as well as higher multivalency effect. FRAP measurements indicate a slow and partial recovery in the coacervates, contrasting with the rapid and almost complete recovery reported in nanostar-based droplets by previous studies.[22, 43-45] Even though we synthesized the polyA building block in house, it is commercially available, and preliminary experiments show that the commercial polyA also undergoes coacervation (Figure S4.9).

Using established strand displacement switching principles of DNA nanoscience, we demonstrated simple switching of our coacervates. The assembly/disassembly switching can also be achieved using RNA/RNase H switches that allow a fine tuning of the kinetics and the design of autonomous systems, where recruitment of the enzymes into the coacervate droplet was observed. The liquid-like properties and

small differences in palindrome binder of these coacervates paved the way towards engineering wetting, clustering, engulfment and merging of distinct coacervate droplet. The interaction of these coacervates can be simply engineered by co-hybridization with other linkers, which should allow for sequential mixing processes in future.

The facile tunability and the facile options for functionalization should enable both fundamental studies into coacervate dynamics and structures, as well as opens doors for applications including delivery, synthetic biology, and for material science.

4.4 Supplementary Information

4.4.1 Materials

All DNA and RNA oligonucleotides were purchased from Integrated DNA Technologies (IDT) and Biomers.net GmbH. Commercial polyA (250-500 bases) was supplied by Sigma-Aldrich. RNase H, rCutSmart™ Buffer (10x), and Nuclease-free water were supplied by New England Biolabs (NEB). dATP solution was supplied by Jena Bioscience GmbH. Ethylenediaminetetraacetic acid disodium salt dihydrate (EDTA) was purchased from Sigma-Aldrich. Terminal Deoxynucleotidyl Transferase (TdT) was supplied by Promega. Agarose low EEO (Agarose Standard) was ordered from AppliChem. SYBR™ Gold Nucleic Acid Gel Stain, DNA gel loading dye (6x), GeneRuler 50 bp DNA Ladder, and GeneRuler 1 kb DNA Ladder were purchased from Thermo Fisher Scientific. Milli-Q water was used throughout this study.

1x rCutSmart™ Buffer (pH=7.9): 50 mM Potassium Acetate, 20 mM Tris-acetate, 10 mM Magnesium Acetate, 100 µg/ml Recombinant Albumin.

5x TdT Buffer (pH=6.8): 500 mM cacodylate buffer, 5 mM $CoCl_2$, 0.5 mM DTT.

TE Buffer (pH=8): 10 mM Tris-HCl and 1 mM EDTA.

4.4.2 Characterization Methods and Instrument

UV-Vis measurements were measured with a DeNovix DS-11 spectrophotometer.

Agarose gel electrophoresis was conducted on the sample with a concentration of 1 µM using agarose gels with 4 wt% agarose in TAE buffer, applying a voltage of 75 V for 3 h.

Confocal laser scanning microscopy (CLSM) was performed using a Leica Stellaris 5 microscope connected to a STX stage top incubator system.

4.4.3 Oligonucleotide Sequences

Table S4.1. Oligonucleotide sequences used, with their names, the sequence codes, the purification methods, and the modifications.

	Name	Oligonucleotide sequence (5'-3')	Purification	Modification
A_{1500}	Primer	C*A*G*CGAGCAAAAA	HPLC	Phosphorothioation
Binder	T_{30}-S_7-**P_{4-1}**	/5ATTO488N/TTTTTTTTTTTTTTTTTTTTTTTTTTTTTTTTTTTTAAACAAA**GTAC**	HPLC	Atto 488 (NHS ester)
	T_{30}-S_7-**P_{4-2}**	/5ATTO488N/TTTTTTTTTTTTTTTTTTTTTTTTTTTTTTTTTTTTAAACAAA**GCGC**	HPLC	Atto 488 (NHS ester)
	T_{30}-S_7-**P_6**	/5ATTO488N/TTTTTTTTTTTTTTTTTTTTTTTTTTTTTTTTTTTTAAACAAA**GCTAGC**	HPLC	Atto 488 (NHS ester)
	T_{30}-S_7-**P_{8-1}** (B_{8-1})	/5ATTO647NN/TTTTTTTTTTTTTTTTTTTTTTTTTTTTTTTTTTTTATTCAA**GTAGCTAC**	HPLC	Atto 647N (NHS ester)
	T_{30}-S_7-**P_{8-2}** (B_{8-2})	/5ATTO488N/TTTTTTTTTTTTTTTTTTTTTTTTTTTTTTTTTTTTAAACAAA**GCTATAGC**	HPLC	Atto 488 (NHS ester)
	T_{30}-S_7-**P_{8-3}** (B_{8-3})	/5ATTO565N/TTTTTTTTTTTTTTTTTTTTTTTTTTTTTTTTTTTTAATTCTT**CAGTACTG**	HPLC	Atto 565 (NHS ester)
	T_{30}-S_7-**P_{10}**	/5ATTO488N/TTTTTTTTTTTTTTTTTTTTTTTTTTTTTTTTTTTTAAACAAA**AGCTATAGCT**	HPLC	Atto 488 (NHS ester)
	T_{30}-S_7-**P_{12}**	/5ATTO488N/TTTTTTTTTTTTTTTTTTTTTTTTTTTTTTTTTTTTAAACAAA**TAGCTATAGCTA**	HPLC	Atto 488 (NHS ester)
C_1 System	T_{30}-S_7-**P_{8-1}** (B_{8-1})	/5ATTO647NN/TTTTTTTTTTTTTTTTTTTTTTTTTTTTTTTTTTTTATTCAA**GTAGCTAC**	HPLC	Atto 647N (NHS ester)
	DNA invader	TTCCTAAT**GTAGCTAC**TTGAATA	Desalting	None
	DNA anti-invader	TATTCAA**GTAGCTAC**ATTAGGAA	Desalting	None
	RNA invader	**GUAGCUAC**UUGAAUA	HPLC	None
	RNA anti-invader	UAUUCAA**GUAGCUAC**AUUAGGAA	HPLC	None

4.4.4 Experimental Protocols

4.4.4.1 Synthesis of ssDNA Polymer A_{1500} by TdT Polymerization

TdT polymerization is a widely employed method for synthesizing ssDNA products through controlled nucleotide polymerization. To synthesize A_{1500}, a mixture of 0.2 µM primer, 300 µM dATP, 1x TdT buffer, and 1 U μL^{-1} TdT enzyme was prepared in nuclease-free water, resulting in a final volume of 150 µL. The reaction was conducted at 37 °C for 2 h and then quenched by adding 20 µL of 200 mM EDTA solution. The obtained polymer was purified using 10 kDa Amicon Ultra Centrifugal Filters and washed three times with TE buffer. The concentration of the polymer was determined using UV-Vis spectroscopy.

4.4.4.2 Palindromic Effect on Coacervate Formation

To evaluate the impact of the palindromic length and GC content on the multivalency-driven coacervation, eight different binder strands with varying palindromic lengths and sequences were introduced. The samples were prepared by dissolving 0.03 g L^{-1} (~0.06 µM) A_{1500} and 1.5 µM binder in rCutSmart buffer containing 10 mM Mg^{2+} and 50 mM K^+ (pH = 7.9), resulting in a final volume of 20 µL. The solutions were incubated for 4 h at 37 °C with gentle rotation at 80 rpm. The resulting structures were visualized and recorded using CLSM. The experiments were conducted using a 384-well microtiter plate with a 0.2 mm glass bottom.

4.4.4.3 Time-Dependent Coacervate Formation

A 20 µL solution was prepared containing 0.06 µM of A_{1500} and 1.5 µM of $B_{8\text{-}1}$ in rCutSmart buffer. This solution was incubated for 30 h at 37 °C with a rotation of 80 rpm. The coacervate formation process was recorded using CLSM.

4.4.4.4 DNA-Triggered Switchable Coacervate

To realize a transformation sequence from coacervate to solution and back to coacervate (coacervate-to-solution-to-coacervate), coacervates containing $B_{8\text{-}1}$ were prepared with a final concentration of 0.06 µM A_{1500} and 1.5 µM (1.0 eq.) of $B_{8\text{-}1}$ in rCutSmart buffer. This mixture was incubated for 12 h at 37 °C with gentle rotation at 80 rpm. Subsequently, 2.25 µM (1.5 eq.) of DNA invader was introduced and allowed to incubate for 0.5 h, resulting in the disassembly of the coacervates. Following this, 3 µM (2.0 eq.) of DNA anti-invader was added and incubated for an additional 16 h, leading to the reformation of coacervates. Images were recorded during this process using CLSM.

4.4.4.5 RNA-Triggered Switchable Coacervate

In the switchable system between coacervate and solution states, coacervates containing $B_{8\text{-}1}$ were prepared with a final concentration of 0.06 µM A_{1500} and 1.5 µM (1.0 eq.) of $B_{8\text{-}1}$ in rCutSmart buffer. This mixture was incubated for 1 h at 37 °C with gentle rotation at 80 rpm. Subsequently, RNA invader (4.5 µM, 3 eq.) was introduced and allowed to incubate for 10 min until the coacervates disappeared. Following this, 0.1 U μL^{-1} RNase H was added and incubated overnight.

For the transformation sequence of solution-to-coacervate-to-solution, a mixture containing 0.06 µM A_{1500}, 1.5 µM (1.0 eq.) $B_{8\text{-}1}$, and 2.25 µM (1.5 eq.) DNA invader was prepared in rCutSmart buffer (complex of $A_{1500}/B_{8\text{-}1}$/DNA invader). The solution was rapidly heated to 80 °C at a rate of 3 °C s^{-1} and then gradually cooled to 20 °C at a rate of 0.01 °C s^{-1}. Subsequently, RNA anti-invader (15 µM, 10.0 eq.) was added to the annealed solution and incubated for 1 h to form coacervates. Following this, 0.1 U μL^{-1} RNase H was introduced and incubated for 2 h, resulting in the coacervates disassembling into a homogeneous solution.

4.4.4.6 RNA-Regulated Transient Coacervate

For the RNA-regulated transient coacervate disassembly system, the coacervates were first prepared with final concentrations of 0.06 µM of A_{1500} and 1.5 µM (1.0 eq.) of $B_{8\text{-}1}$ in rCutSmart buffer. The mixture was incubated for 2 h at 37 °C with gentle rotation at 80 rpm. Following this, varying amounts of RNA invader (15 µM, 45 µM, 75 µM) and 0.1 U μL^{-1} RNase H were added into the solution. The mixture was then incubated at 37 °C with gentle rotation at 80 rpm. Images were recorded during this process using CLSM, and the tunable reassembly time was monitored. Additionally, to further explore the effect of RNase H concentration on the reassembly time, RNA invader (15 µM, 10.0 eq.) and different RNase H concentrations (0.03, 0.05, 0.1 U μL^{-1}) were introduced. The duration of reassembly is measured from the moment the preformed coacervates disassemble to the commencement of coacervate reformation.

To achieve opposite pathway (transient coacervate assembly), RNA anti-invader and RNase H were introduced. The complex of A_{1500}/$B_{8\text{-}1}$/DNA invader was prepared with a final concentration of 0.06 µM A_{1500}, 1.5 µM (1.0 eq.) $B_{8\text{-}1}$, and 2.25 µM (1.5 eq.) DNA invader in rCutSmart buffer. The solution was rapidly heated to 80 °C at a rate of 3 °C s^{-1} and then gradually cooled to 20 °C at a rate of 0.01 °C s^{-1}. Then different concentrations of RNA anti-invader (15 µM, 45 µM) and RNase H (0.1 U μL^{-1}) were added to the solution. The mixture was incubated at 37 °C with gentle rotation at 80 rpm, and images were recorded during this process using CLSM.

4.4.4.7 Engineering Wetting Between Coacervates

Three distinct coacervate structures, denoted as C_1, C_2, and C_3, were prepared using different binders ($B_{8\text{-}1}$, $B_{8\text{-}2}$, and $B_{8\text{-}3}$). A mixture with a final concentration of 0.06 µM A_{1500} and 1.5 µM of the respective B_x was dissolved in rCutSmart buffer and incubated for 1 h at 37 °C with gentle rotation at 80 rpm. Subsequently, two of these resulting coacervates were mixed and incubated for 11 days at 37 °C without shaking (shaking was avoided in this case to limit collisions). The morphological changes during this period were captured and recorded using CLSM.

4.4.4.8 Engineering Wetting Under Nucleation Process by Activating C_1 to Preformed C_2 (or C_3)

To investigate the structures that can emerge through the wetting behavior during nucleation process, we introduced a system where $B_{8\text{-}1}$ is blocked by an RNA invader.

Coacervates of C_2 and C_3 were prepared as described previously. A mixture consisting of A_{1500} (0.06 μM), $B_{8\text{-}1}$ (1.5 μM, 1.0 eq.), and RNA invader (2.25 μM, 1.5 eq.) was prepared in rCutSmart buffer, forming the complex of A_{1500}/$B_{8\text{-}1}$/RNA invader. The solution was rapidly heated to 80 °C at a rate of 3 °C s^{-1} and then gradually cooled to 20 °C at a rate of 0.01 °C s^{-1}. Subsequently, 0.1 U μL^{-1} RNase H and preformed C_2 (or C_3) were introduced into the solution and incubated for 72 h at 37 °C with gentle rotation at 80 rpm. The morphological changes occurring during this period were monitored and recorded using CLSM.

4.4.4.9 Accelerated Wetting Between Two Coacervates

To facilitate the wetting process, coacervate C_{31}, incorporating different ratios of $B_{8\text{-}1}$ and $B_{8\text{-}3}$ ($B_{8\text{-}3}$:$B_{8\text{-}1}$=75%:25%, 50%:50%), was employed. In the system with 75%:25% $B_{8\text{-}3}$:$B_{8\text{-}1}$, a mixture comprising 1.125 μM of $B_{8\text{-}3}$ and 0.375 μM of $B_{8\text{-}1}$ was combined with 0.06 μM A_{1500} in rCutSmart buffer. This solution was then incubated for 1 h at 37 °C with gentle rotation at 80 rpm to form C_{31}. C_1 was prepared as described previously. Subsequently, C_{31} solution was mixed with the C_1 solution and incubated for 7 days at 37 °C without shaking. Morphological changes during this period were observed and recorded using CLSM.

4.4.4.10 Strand Exchange Reaction Between A_{37}/$B_{8\text{-}1}$ and $B_{8\text{-}2}$

A mixture was prepared by mixing 2 μM A_{37} and 10 μM $B_{8\text{-}1}$ in rCutSmart buffer, resulting in a final volume of 20 μL. This solution was rapidly heated to 80 °C at a rate of 3 °C s^{-1} and then slowly cooled to 20 °C at a rate of 0.01 °C s^{-1}. Then 10 μM $B_{8\text{-}2}$ was added to the solution, and the mixture was incubated for 24 h at 37 °C. The samples were analyzed through agarose gel electrophoresis using a 4 wt% agarose gel.

4.4.4.11 Coacervate Formation Using Commercial polyA

A 20 μL solution was prepared containing 0.06 μM of polyA and 2.5 μM of $B_{8\text{-}1}$ in rCutSmart buffer. This solution was incubated at 37 °C with a rotation of 80 rpm, and images were recorded during this process using CLSM.

4.4.5 Supplementary Figures

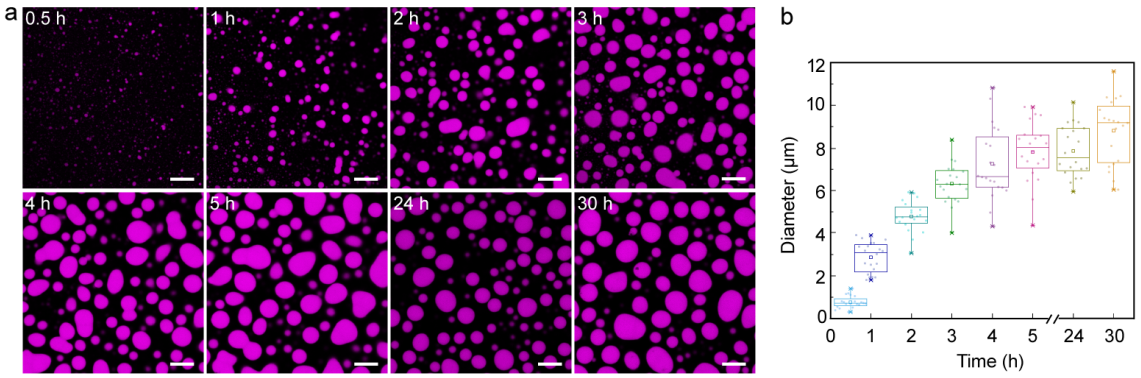

Figure S4.1. Coacervate formation for $A_{1500}/B_{8\text{-}1}$. (a) Time-dependent CLSM images. **(b)** Coacervate diameter from (a). The square and line inside the box represent the mean and median values of the coacervate population, respectively. The box represents a five-number summary of the coacervate dataset, extending from the first quartile to the third quartile. Error bars are the standard deviation of ca. 20 coacervate counts. Scale bars: 10 µm.

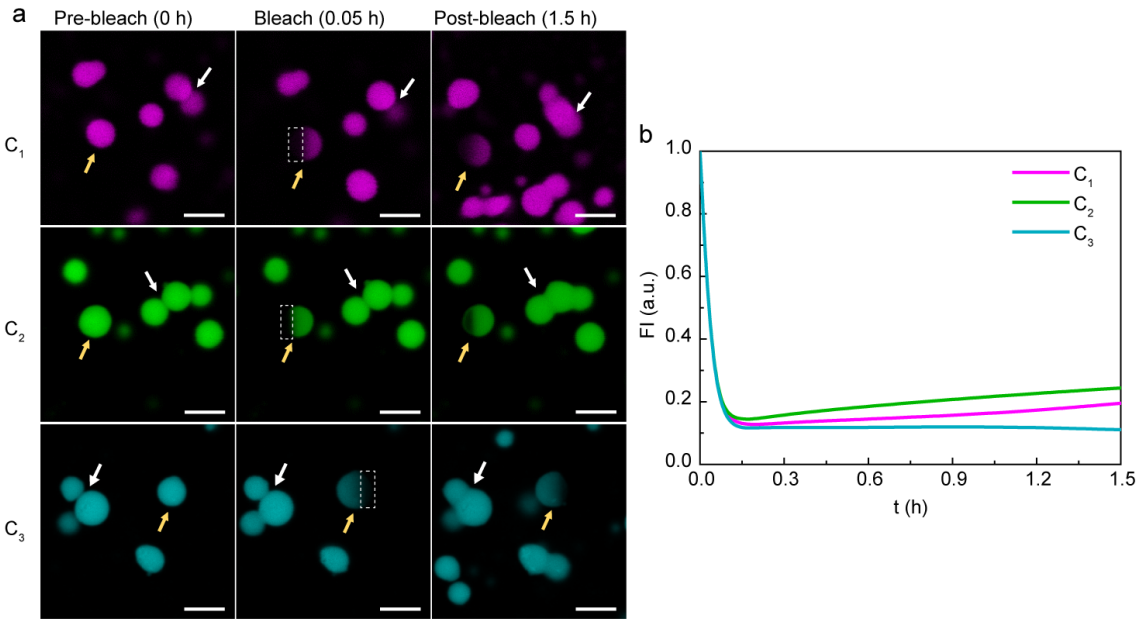

Figure S4.2. Fluorescence recovery after photobleaching (FRAP) and fusion behavior of C_1, C_2, and C_3 using different binders ($B_{8\text{-}1}$, $B_{8\text{-}2}$, and $B_{8\text{-}3}$). (a) CLSM images of the coacervates during a FRAP experiment at different time points: pre-bleach (0 s), bleach (0.05 h), and after-bleaching (1.5 h). **(b)** The corresponding fluorescence intensity from (a) confirm that the coacervates exhibit limited mobility in their interior regions. Scale bars: 5 µm.

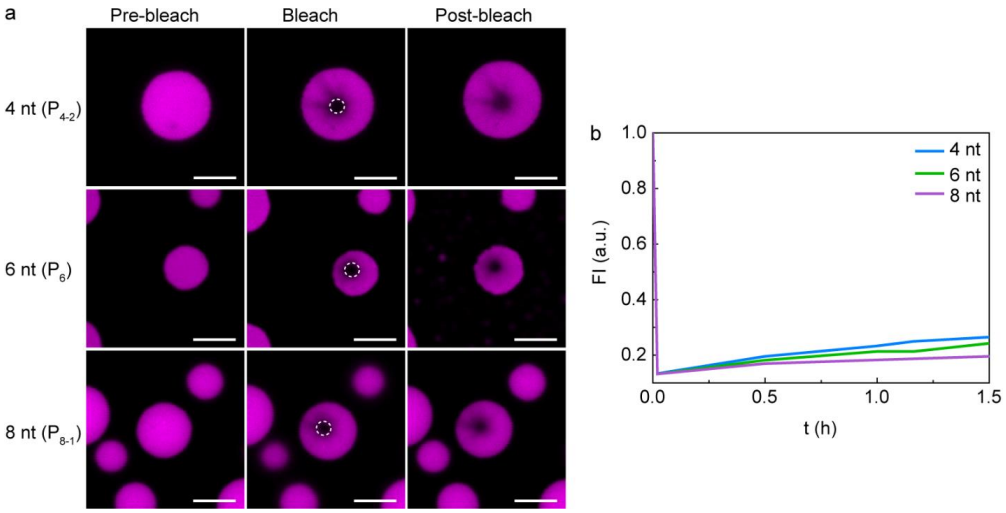

Figure S4.3. Fuorescence recovery after photobleaching (FRAP) of coacervates employing different binders with varying lengths of palindromic domains, including 4, 6, and 8 nucleotides. (a) CLSM images of the coacervates during a FRAP experiment at different time points: pre-bleach (0 s), bleach (0.02 h), and after-bleaching (1.5 h). **(b)** The corresponding fluorescence intensity from (a) indicate that the coacervates exhibit limited mobility within their interior regions, with mobility decreasing as the length of palindromic domains increases. Scale bars: 5 µm.

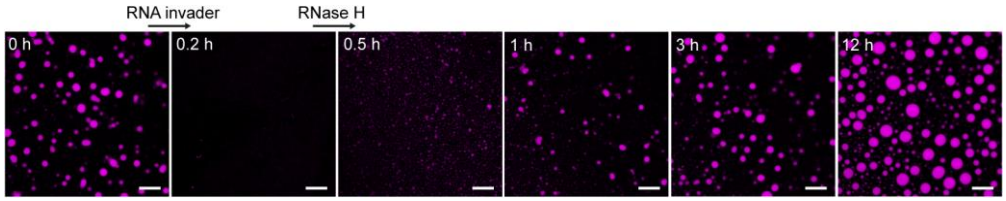

Figure S4.4. RNA-triggered switchable system. CLSM images of RNA-triggered switchable system between coacervate and solution states. Scale bars: 10 µm.

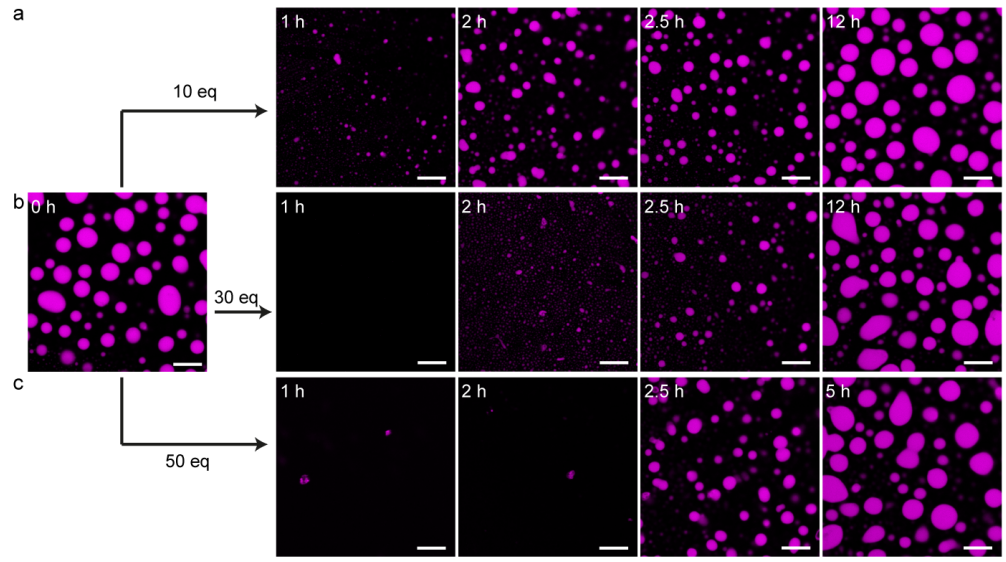

Figure S4.5. RNA-regulated transient coacervate disassembly system by introducing varying concentrations of RNA invader. Time-dependent CLSM images of transient coacervate disassembly system with reassembly times, achieved by introducing varying amounts of RNA invader (10 eq., 30 eq., 50 eq.) in the presence of 0.1 U µL^{-1} RNase H. Scale bars: 10 µm.

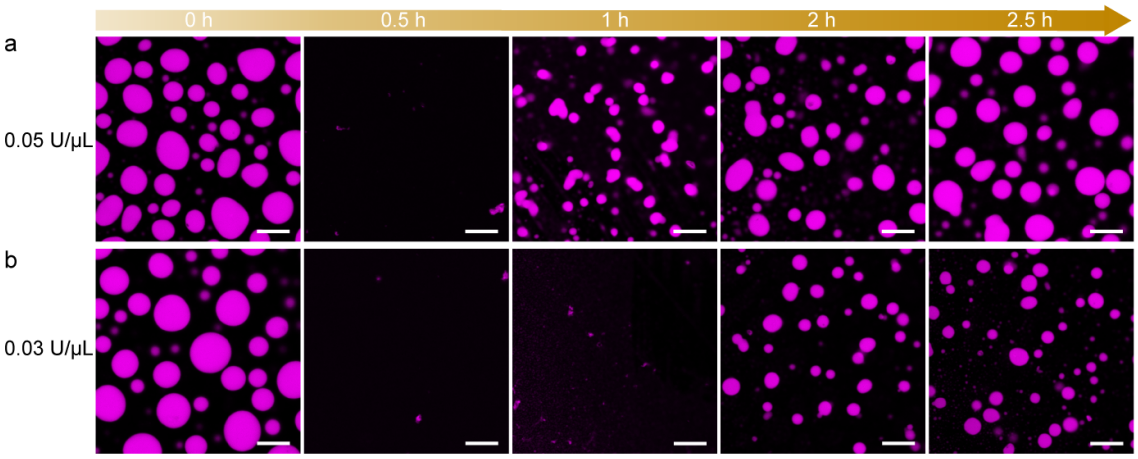

Figure S4.6. RNA-regulated transient coacervate disassembly system by introducing varying concentrations of RNase H. Time-dependent CLSM images of transient coacervate disassembly system with reassembly times, achieved by introducing varying concentrations of RNase H (0.03 U μL^{-1}, 0.05 U μL^{-1}) in the presence of 15 μM (10 eq.) RNA invader. Scale bars: 10 μm.

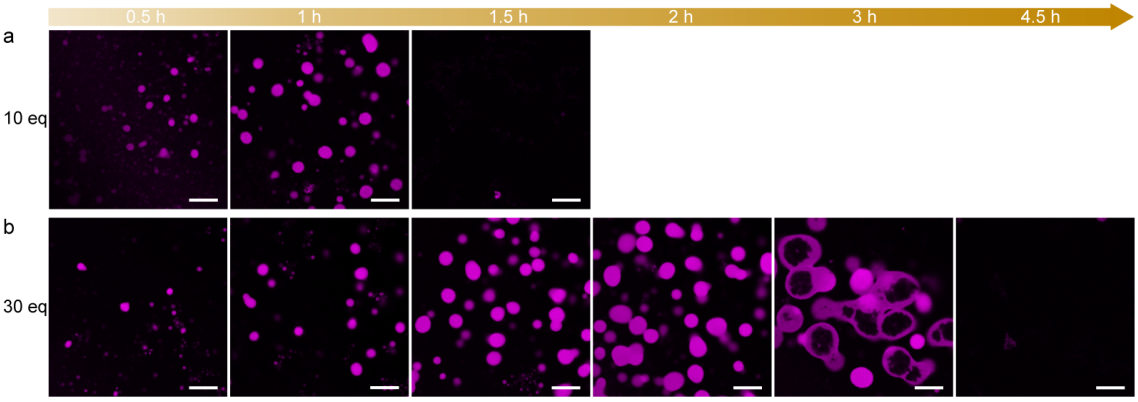

Figure S4.7. RNA-regulated transient coacervate assembly system by using different concentrations of RNA anti-invader. Time-dependent CLSM images of transient coacervate assembly, conducted by using different concentrations of RNA anti-invader (10 eq., 30 eq.) in the presence of 0.1 U μL^{-1} RNase H. Scale bars: 10 μm.

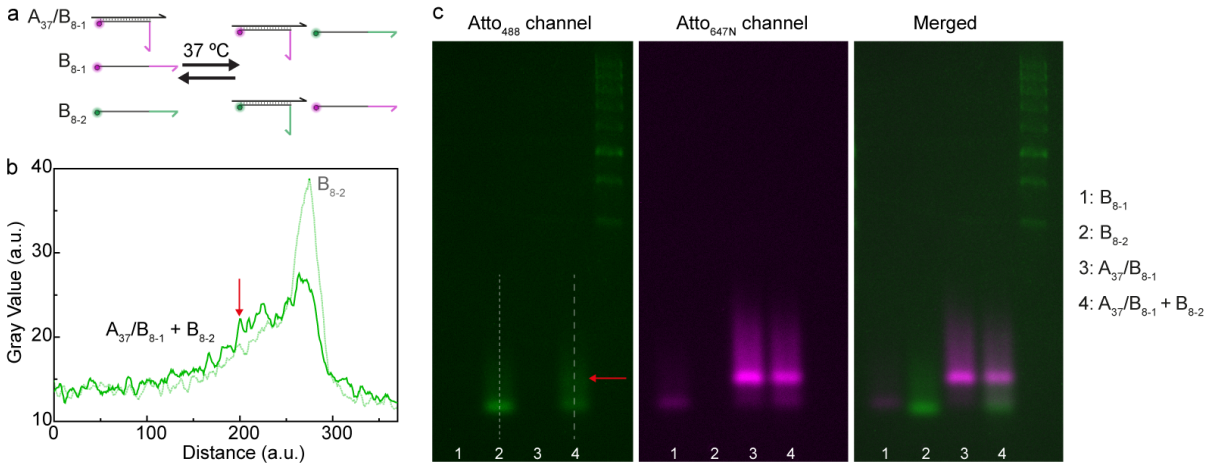

Figure S4.8. Strand exchange reaction between $A_{37}/B_{8\text{-}1}$ and $B_{8\text{-}2}$. (a) Schematic illustration of reaction design. **(b)** Fluorescence intensity plot for the $Atto_{488}$ channel demonstrates that minor dynamic strand exchange occurred within 1 day during the reaction. **(c)** Agarose gel electrophoresis for the system with different channels.

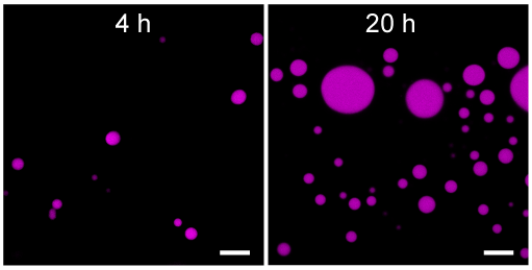

Figure S4.9. Coacervate formation using commercial polyA. CLSM images of coacervates formed from commercial polyA and $B_{8\text{-}1}$ following incubation at 37 °C for 4 hours and 20 hours. Scale bars: 10 µm.

4.5 References

1. Banani, S.F., Lee, H.O., Hyman, A.A. & Rosen, M.K. Biomolecular condensates: organizers of cellular biochemistry. *Nat. Rev. Mol. Cell Biol.* **18**, 285-298 (2017).
2. Garabedian, M.V. et al. Designer membraneless organelles sequester native factors for control of cell behavior. *Nat. Chem. Biol.* **17**, 998-1007 (2021).
3. Gomes, E. & Shorter, J. The molecular language of membraneless organelles. *J. Biol. Chem.* **294**, 7115-7127 (2019).
4. Hernandez-Verdun, D. Assembly and disassembly of the nucleolus during the cell cycle. *Nucleus* **2**, 189-194 (2011).
5. Mao, Y.S., Zhang, B. & Spector, D.L. Biogenesis and function of nuclear bodies. *Trends Genet.* **27**, 295-306 (2011).
6. Decker, C.J. & Parker, R. P-Bodies and Stress Granules: Possible Roles in the Control of Translation and mRNA Degradation. *Cold Spring Harb. perspect. biol.* **4**, a012286 (2012).
7. Kaur, T. et al. Sequence-encoded and composition-dependent protein-RNA interactions control multiphasic condensate morphologies. *Nat. Commun.* **12**, 872 (2021).
8. Liu, W., Samanta, A., Deng, J., Akintayo, C.O. & Walther, A. Mechanistic Insights into the Phase Separation Behavior and Pathway-Directed Information Exchange in all-DNA Droplets. *Angew. Chem. Int. Ed.* **61**, e202208951 (2022).
9. Milovanovic, D., Wu, Y., Bian, X. & Camilli, P.D. A liquid phase of synapsin and lipid vesicles. *Science* **361**, 604-607 (2018).
10. Hirose, T., Ninomiya, K., Nakagawa, S. & Yamazaki, T. A guide to membraneless organelles and their various roles in gene regulation. *Nat. Rev. Mol. Cell Biol.* **24**, 288-304 (2023).
11. Beutel, O., Maraspini, R., Pombo-García, K., Martin-Lemaitre, C. & Honigmann, A. Phase Separation of Zonula Occludens Proteins Drives Formation of Tight Junctions. *Cell* **179**, 923-936 (2019).
12. Schuster, B.S. et al. Controllable protein phase separation and modular recruitment to form responsive membraneless organelles. *Nat. Commun.* **9**, 2985 (2018).
13. Yewdall, N.A., André, A.A.M., Lu, T. & Spruijt, E. Coacervates as models of membraneless organelles. *Curr. Opin. Colloid Interface Sci.* **52**, 101416 (2021).
14. Hyman, A.A., Weber, C.A. & Jülicher, F. Liquid-Liquid Phase Separation in Biology. *Annu. Rev. Cell Dev. Biol.* **30**, 39-58 (2014).
15. Liu, W., Lupfer, C., Samanta, A., Sarkar, A. & Walther, A. Switchable Hydrophobic Pockets in DNA Protocells Enhance Chemical Conversion. *J. Am. Chem. Soc.* **145**, 7090-7094 (2023).
16. Leathers, A. et al. Reaction-Diffusion Patterning of DNA-Based Artificial Cells. *J. Am. Chem. Soc.* **144**, 17468-17476 (2022).
17. Cook, A. B., Novosedlik, S. & van Hest, J. C. M. Complex Coacervate Materials as Artificial Cells. *Acc. Mater. Res.* **4**, 287-298 (2023).
18. Lu, T. et al. Endocytosis of Coacervates into Liposomes. *J. Am. Chem. Soc.* **144**, 13451-13455 (2022).
19. te Brinke, E. et al. Dissipative adaptation in driven self-assembly leading to self-dividing fibrils. *Nat. Nanotechnol.* **13**, 849-855 (2018).
20. Spruijt, E. Open questions on liquid-liquid phase separation. *Commun. Chem.* **6**, 23 (2023).
21. Wang, J., Li, Z. & Willner, I. Dynamic Reconfigurable DNA Nanostructures, Networks and Materials. *Angew. Chem. Int. Ed.* **62**, e202215332 (2023).

22. Sato, Y., Sakamoto, T. & Takinoue, M. Sequence-based engineering of dynamic functions of micrometer-sized DNA droplets. *Sci. Adv.* **6**, eaba3471 (2020).
23. Merindol, R., Loescher, S., Samanta, A. & Walther, A. Pathway-controlled formation of mesostructured all-DNA colloids and superstructures. *Nat. Nanotechnol.* **13**, 730-738 (2018).
24. Samanta, A., Hörner, M., Liu, W., Weber, W. & Walther, A. Signal-processing and adaptive prototissue formation in metabolic DNA protocells. *Nat. Commun.* **13**, 3968 (2022).
25. Samanta, A., Sabatino, V., Ward, T.R. & Walther, A. Functional and morphological adaptation in DNA protocells via signal processing prompted by artificial metalloenzymes. *Nat. Nanotechnol.* **15**, 914-921 (2020).
26. Jeon, B.-j., Nguyen, D. T. & Saleh, O. A. Sequence-Controlled Adhesion and Microemulsification in a Two-Phase System of DNA Liquid Droplets. *J. Phys. Chem. B* **124**, 8888-8895 (2020).
27. Deng, J. & Walther, A. Programmable and Chemically Fueled DNA Coacervates by Transient Liquid-Liquid Phase Separation. *Chem* **6**, 3329-3343 (2020).
28. Sato, Y. & Takinoue, M. Sequence-dependent fusion dynamics and physical properties of DNA droplets. *Nanoscale Adv.* **5**, 1919-1925 (2023).
29. Mangiarotti, A., Chen, N., Zhao, Z., Lipowsky, R. & Dimova, R. Wetting and complex remodeling of membranes by biomolecular condensates. *Nat. Commun.* **14**, 2809 (2023).
30. Deng, J. & Walther, A. ATP-powered molecular recognition to engineer transient multivalency and self-sorting 4D hierarchical systems. *Nat. Commun.* **11**, 3658 (2020).
31. Rubio-Sánchez, R., Mognetti, B. M., Cicuta, P. & Di Michele, L. DNA-Origami Line-Actants Control Domain Organization and Fission in Synthetic Membranes. *J. Am. Chem. Soc.* **145**, 11265-11275 (2023).
32. Li, Z. et al. Dynamic Fusion of Nucleic Acid Functionalized Nano-/Micro-Cell-Like Containments: From Basic Concepts to Applications. *ACS Nano* **17**, 15308-15327 (2023).
33. Heinen, L. & Walther, A. Celebrating Soft Matter's 10th Anniversary: Approaches to program the time domain of self-assemblies. *Soft Matter* **11**, 7857-7866 (2015).
34. Tang, L., Navarro, L.A., Chilkoti, A. & Zauscher, S. High-Molecular-Weight Polynucleotides by Transferase-Catalyzed Living Chain-Growth Polycondensation. *Angew. Chem. Int. Ed.* **56**, 6778-6782 (2017).
35. Fowler, J.D. & Suo, Z. Biochemical, Structural, and Physiological Characterization of Terminal Deoxynucleotidyl Transferase. *Chem. Rev.* **106**, 2092-2110 (2006).
36. Green, L.N. et al. Autonomous dynamic control of DNA nanostructure self-assembly. *Nat. Chem.* **11**, 510-520 (2019).
37. Sun, M., Deng, J. & Walther, A. Communication and Cross-Regulation between Chemically Fueled Sender and Receiver Reaction Networks. *Angew. Chem. Int. Ed.* **62**, e202214499 (2023).
38. Farag, N., Dordevic, M., Del Grosso, E. & Ricci, F. Dynamic and Reversible Decoration of DNA-Based Scaffolds. *Adv. Mater.* **35**, e2211274 (2023).
39. Saleh, O.A., Jeon, B.J. & Liedl, T. Enzymatic degradation of liquid droplets of DNA is modulated near the phase boundary. *PNAS* **117**, 16160-16166 (2020).
40. Yoo, B.Y. & Chrispeels, M.J. The origin of protein bodies in developing soybean cotyledons: a proposal. *Protoplasma* **103**, 201-204 (1980).
41. Ambroggio, E.E., Costa Navarro, G.S., Perez Socas, L.B., Bagatolli, L.A. & Gamarnik, A.V. Dengue and Zika virus capsid proteins bind to membranes and self-assemble into liquid droplets with nucleic acids. *J. Biol. Chem.* **297**, 101059 (2021).
42. Snead, W.T. et al. Membrane surfaces regulate assembly of ribonucleoprotein condensates. *Nat. Cell Biol.* **24**, 461-470 (2022).
43. Agarwal, S., Osmanovic, D., Dizani, M., Klocke, M.A. & Franco, E. Dynamic control of DNA condensation. *Nat. Commun.* **15**, 1915 (2024).
44. Maruyama, T., Gong, J. & Takinoue, M. Temporally controlled multistep division of DNA droplets for dynamic artificial cells. *ChemRxiv*, doi:10.26434/chemrxiv-2024-z67br (2024).
45. Skipper, K. & Wickham, S. Core-shell coacervates formed from DNA nanostars. *ChemRxiv*, doi:10.26434/chemrxiv-2024-07pvd (2024).

5 Synopsis

This chapter concludes this thesis by summarizing the findings from the investigations into hierarchical DNA-based structures for synthetic cells. A comprehensive overview of the results is presented, highlighting the key contributions to the field. Furthermore, this chapter outlines future research directions, offering insights into potential areas of exploration and development within this domain.

5.1 Conclusion

This thesis showcases different hierarchical DNA-based structures created by manipulating weak interactions, including electrostatic interactions, hydrophilic/hydrophobic interactions and hydrogen bonding, which induce liquid-liquid phase separation (LLPS) in DNA-based systems. Thermo-responsive phase separation of polyadenine-rich ssDNA polymers allows the formation of kinetically trapped all-DNA coacervates in the presence of Mg^{2+} or Ca^{2+}. The novel Ca^{2+}-pathway opens a new design space to trigger information exchange between coacervates and protocells stemming from distinct ion-specific pathways. A hybrid artificial cell system was created via integrating an all-DNA-based synthetic cell model (Mg^{2+}-induced protocell) with synthetic temperature-switchable block copolymers (ssDNA-*b*-pEGA). Tunable and reversible organelle formation of hydrophobic pockets occurred within the protocells core during heat shock, and these hydrophobic compartments could accelerate chemical conversion of self-reporting bimolecular reactions based on a protected dansylfuran. In addition to thermo-responsive phase separation, an isothermal method has also been developed to form all-DNA-based synthetic cell model (coacervate) using a simple and versatile platform by integrating a long ssDNA homopolymer with a series of palindromic binders at physiological temperature. The synthetic coacervates were developed to establish switching and autonomous systems, and were used to engineer multiphase structures through wetting, engulfment, and fusion.

The research is discussed in more detail in **Chapter 2**, where we have systematically investigated the coacervation of ssDNA polymers based on thermo-responsive phase separation that is important for the formation of DNA droplets and DNA-based protocells as entities to study life-like behavior in complex systems. We mainly focused on differences between the previously established Mg^{2+}-type phase separation and

Ca^{2+}-dependent pathway discovered here, particularly with respect to the reversibility and sequence-specificity of the phase separation processes. The most critical and consistent observation was the reversibility of the phase separation in the case of Mg^{2+}, whereas the phase separation was irreversible for Ca^{2+}-pathway. Based on irreversible phase separation of ssDNA in the presence of Ca^{2+}, a straightforward pathway was used to form all-DNA droplets in a few minutes via a simple temperature ramp. The phase separation of ssDNA passed through two different transition temperatures during heating process, confirming a nucleation and growth-like mechanism, which was termed as “two-stage process”. Additionally, an appropriate length was required to obtain sufficient phase separation, while excessively long strands hindered re-obtaining a spherical shape after droplet coalescence at high temperatures, deriving important aspects regarding the sphericity and size of the coacervates. This salt-dependent phase separation behavior allows the creation of new coacervate structures by mixing multiple coacervate systems. Ca^{2+}-derived polyadenine (polyA)-rich droplets (that would be unstable in a Mg^{2+} setting) could merge their information content with Mg^{2+}-derived core/shell DNA protocells formed by polyA/polythymine (that would equally not form in a Ca^{2+}-setting) by proper salinity adjustment and using a secondary temperature ramp. These phase behaviors of sequence-specific nucleic acid polymers may provide an essential understanding of relevant scenarios in living cells, such as heat shock-mediated droplet formation inside the living cell cytoplasm or the relevance of a polyA-tag present in each mRNA produced in the nucleus.

Building on the foundations laid in Chapter 2, **Chapter 3** demonstrated how to leverage synergies between the DNA world (Mg^{2+}-derived core/shell DNA protocells) and synthetic temperature-responsive block copolymers (ssDNA-*b*-polyethylene glycol acrylate block copolymer) to create switchable hydrophobic compartments in hybrid protocells. In situ microscopy measurements revealed a spinodal/viscoelastic decomposition within protocells, in contrast to binodal decomposition in dilute solutions. The transition from a network to a concentric layer was explained by co-condensation of the ssDNA interior of the protocells and the encapsulated synthetic copolymer segment. The extent of phase separation could be modulated by crosslinking the interior of the protocells with Ca^{2+} and/or specific DNA-based crosslinker, which should allow further fine control over secondary structuration inside protocells in the future.

These hydrophobic compartments accelerated chemical conversion of bimolecular reactions. These findings shed light on phase segregation processes under viscoelastic confinement (leading to spinodal/viscoelastic and not binodal structures) and provide avenues for chemical microreactors that enhance chemical response by sensing the elevated temperature of its surroundings.

In addition to thermo-responsive phase separation, an isothermal method for phase separation was also developed to investigate the coacervation of ssDNA, forming dynamic, multivalency-driven DNA coacervates at physiological temperature using a long ssDNA homopolymer in combination with a series of palindromic binders (**Chapter 4)**. The synthetic coacervate was developed to establish switching and autonomous systems, leveraging tools from DNA and RNA nanoscience. Autonomous transient coacervate system was realized by using RNA/RNase H switches, where recruitment of the enzymes into the coacervate droplet was observed. The liquid-like properties and small differences in palindrome binder of these coacervates paved the way for wetting, engulfment, and merging of distinct coacervate droplets. This study not only paves the way for designing and controlling innovative synthetic DNA coacervates but also enhances the understanding of coacervate dynamics, phase transition mechanisms, and the wetting behavior between coacervates.

In summary, these investigations of LLPS-driven tunable hierarchical DNA-based systems offer a better understanding of coacervation and properties of organelles, and also expand the prospects of such structured artificial DNA-based cell models for applications in delivery systems, microreactors, synthetic biology, and material science.

5.2 Outlook

Biomolecular coacervates are promising model systems to understand biological systems such as membraneless organelles, and important building blocks for designer applications in controlled delivery, synthetic biology, or as chemical nanoreactors.[1-3] Since DNA has emerged as a powerful building block for developing hierarchical nano/microstructures because of its programmability and sequence-specificity, engineering all-DNA coacervates in a bottom-up approach would provide a platform to study biological activities in a DNA-based crowded environment.[4-6] Different hierarchical DNA-based structures as cell-mimicking systems are presented in the

thesis, these findings may trigger further research on the understanding of living cells and the origin of life.

The thesis provided mechanistic insights into the metal-dependent phase separation of ssDNA and leveraged this understanding for a straightforward formation of all-DNA droplets (Chapter 2). The finding that ssDNA length influences droplet formation may trigger the development of ssDNA column for the purification or selection of ssDNA length. It may also lead to further investigation on the construction of mRNA polyA-based coacervation and the effect of polyA-tail length on transcript function.[7-9] The differential binding affinity of Ca^{2+} and Mg^{2+} with DNA can lead to the research applications on the enzyme activity and DNA interactions, thereby regulating the cellular processes including DNA replication, transcription, and repair.

Spatiotemporal compartmentalization in living cells provides segregated microenvironments in the form of membraneless organelles.[10] Inspired by these phenomena, we introduced a bottom-up process to investigate subcompartmentalization in artificial cells by combining all-DNA core/shell protocells with a ssDNA-*b*-polyethylene glycol acrylate block copolymer (Chapter 3). It sheds light on phase segregation processes under viscoelastic confinement and provides avenues for chemical microreactors that enhance chemical response by sensing the elevated temperature of their surroundings. However, the data can only show that the subcompartmentalization arises from classical spinodal or viscoelastic phase separation due to limited protocell size and spatiotemporal resolution. An in-depth analysis of the mechanism would provide further insight into the phase separation under crowded conditions. Various approaches can be used to tune the protocell size, such as controlling ssDNA length and concentration, protocell dynamics interior, or ratio of the two employed ssDNA polymers.[11] Moreover, a rich diversity of compartmental morphologies such as droplet coacervates and gentle incubation temperature are expected, which may be achieved by the introduction of encapsulation materials with lower cloud point temperature.

Furthermore, an easy-to-use platform was developed for constructing all-DNA coacervates utilizing ssDNA components and multivalency-driven LLPS at physiological temperature (Chapter 4). Our research detailed the influences of the length and sequence of multivalent, self-complimentary binders on coacervate formation. Exploiting the varying phase separation rates induced by different binders

will enable autonomous control over system dynamics and kinetics, as well as over nucleation and growth processes.[12] This concept will be conducive to the formation of core/shell droplets with tunable size and permeability by leveraging the differences in phase-separation speeds between two binder systems. In this model, the faster-separation phase can form the core, while the interaction of other binder systems with the core promotes the nucleation of a shell.[13] Such advancements have the potential to enhance structural and system complexity, aiding in the fabrication of precise cellular models and deepening our understanding of system dynamics. Additionally, the engineering of interactions between coacervates has given rise to a rich diversity of morphologies, initiating a groundbreaking method for enzymatic cascade reactions upon their contact.[14, 15] This strategy is set to enable controllable chemical reactivity and significantly improve the efficiency of desired reactions, promising benefits in biochemical and synthetic applications.

5.3 References

1. Dogterom, M., Kamat, N.P., Jewett, M.C. & Adamala, K.P. Progress in Engineering Synthetic Cells and Cell-Free Systems. *ACS Synth. Biol.* **13**, 695-696 (2024).
2. Lu, T. & Spruijt, E. Multiphase Complex Coacervate Droplets. *J. Am. Chem. Soc.* **142**, 2905-2914 (2020).
3. Buddingh, B.C. & van Hest, J.C.M. Artificial Cells: Synthetic Compartments with Life-like Functionality and Adaptivity. *Acc. Chem. Res.* **50**, 769-777 (2017).
4. Leathers, A. et al. Reaction-Diffusion Patterning of DNA-Based Artificial Cells. *J. Am. Chem. Soc.* **144**, 17468-17476 (2022).
5. Martin, N. et al. Photoswitchable Phase Separation and Oligonucleotide Trafficking in DNA Coacervate Microdroplets. *Angew. Chem. Int. Ed.* **58**, 14594-14598 (2019).
6. Sato, Y., Sakamoto, T. & Takinoue, M. Sequence-based engineering of dynamic functions of micrometer-sized DNA droplets. *Sci. Adv.* **6**, eaba3471 (2020).
7. Xiang, K. & Bartel, D.P. The molecular basis of coupling between poly(A)-tail length and translational efficiency. *eLife* **10**, e66493 (2021).
8. Jalkanen, A.L., Coleman, S.J. & Wilusz, J. Determinants and implications of mRNA poly(A) tail size--does this protein make my tail look big? *Semin. Cell Dev. Biol.* **34**, 24-32 (2014).
9. Ma, Y. et al. Nucleobase Clustering Contributes to the Formation and Hollowing of Repeat-Expansion RNA Condensate. *J. Am. Chem. Soc.* **144**, 4716-4720 (2022).
10. Capasso Palmiero, U. et al. Programmable Zwitterionic Droplets as Biomolecular Sorters and Model of Membraneless Organelles. *Adv. Mater.* **34**, e2104837 (2022).
11. Merindol, R., Loescher, S., Samanta, A. & Walther, A. Pathway-controlled formation of mesostructured all-DNA colloids and superstructures. *Nat. Nanotechnol.* **13**, 730-738 (2018).
12. Thanh, N.T., Maclean, N. & Mahiddine, S. Mechanisms of nucleation and growth of nanoparticles in solution. *Chem. Rev.* **114**, 7610-7630 (2014).
13. Skipper, K. & Wickham, S. Core-shell coacervates formed from DNA nanostars. *ChemRxiv*, doi:10.26434/chemrxiv-2024-07pvd (2024).
14. Deng, J. & Walther, A. Programmable and Chemically Fueled DNA Coacervates by Transient Liquid-Liquid Phase Separation. *Chem* **6**, 3329-3343 (2020).
15. Kojima, T. & Takayama, S. Membraneless Compartmentalization Facilitates Enzymatic Cascade Reactions and Reduces Substrate Inhibition. *ACS Appl. Mater. Interfaces* **10**, 32782-32791 (2018).

Acknowledgements

Reflecting on my doctoral journey, I would like to acknowledge all the members of our group and the people who offered their assistance and contributed to this thesis.